International joint supervision of thesis

UNIVERSIDADE ESTADUAL PAULISTA "JÚLIO DE MESQUITA FILHO"

Programa de Pós-graduação em Ciência e Tecnologia de Materiais

and

UNIVERSITÉ DE PAU ET DES PAYS DE L'ADOUR

Ecole Doctorale Sciences Exactes et leurs Applications

Bruna Andressa Bregadiolli

STUDY AND DEVELOPMENT OF MATERIALS FOR APPLICATIONS IN HYBRID SOLAR CELLS

Brazilian supervisor: Prof. Dr. Carlos Frederico de Oliveira Graeff
French supervisor: Dr. Roger. Hiorns

2016

UNIVERSIDADE ESTADUAL PAULISTA “JÚLIO DE MESQUITA FILHO”
Programa de Pós-graduação em Ciência e Tecnologia de Materiais

Bruna Andressa Bregadiolli

ESTUDO E DESENVOLVIMENTO DE MATERIAIS PARA APLICAÇÕES EM CÉLULAS SOLARES HÍBRIDAS

BAURU
2016

Bruna Andressa Bregadiolli

Estudo e desenvolvimento de materiais para aplicações em células solares híbridas

Tese apresentada como requisito à obtenção do título de Doutora à Universidade Estadual Paulista "Júlio de Mesquita Filho" - Programa de Pós-graduação em Ciência e Tecnologia de Materiais, sob a orientação do Prof. Dr. Carlos Frederico de Oliveira Graeff.

BAURU
2016

UNIVERSIDADE ESTADUAL PAULISTA

Câmpus de Bauru

Faculdade de Ciências

ATA DA DEFESA PÚBLICA DA TESE DE DOUTORADO DE BRUNA ANDRESSA BREGADIOLLI, DISCENTE DO PROGRAMA DE PÓS-GRADUAÇÃO EM CIÊNCIA E TECNOLOGIA DE MATERIAIS, DA FACULDADE DE CIÊNCIAS.

Aos 20 dias do mês de setembro do ano de 2016, às 14:00 horas, no(a) Sala de Videoconferência da FC/Bauru, reuniu-se a Comissão Examinadora da Defesa Pública, composta pelos seguintes membros: Prof. Dr. CARLOS FREDERICO DE OLIVEIRA GRAEFF - Orientador(a) do(a) Departamento de Física / Faculdade de Ciências - UNESP - Bauru, Profª. Drª. ALEJANDRA HORTENCIA MIRANDA GONZÁLES do(a) Campus Pirituba / Universidade Anhanguera de São Paulo - UNIAN, Prof. Dr. FRANCISCO EDUARDO GONTIJO GUIMARÃES do(a) Departamento de Física e Ciência dos Materiais / Instituto de Física de São Carlos / Universidade de São Paulo, Prof. Dr. ALEXANDRE FONTES DA FONSECA do(a) Departamento de Física Aplicada / Universidade Estadual de Campinas/ UNICAMP, Prof. Dr. ANDRÉ SARTO POLO do(a) Centro de Ciências Naturais e Humanas / UNIVERSIDADE FEDERAL DO ABC, sob a presidência do primeiro, a fim de proceder a arguição pública da TESE DE DOUTORADO de BRUNA ANDRESSA BREGADIOLLI, intitulada **Estudo e desenvolvimento de materiais para aplicações em células solares híbridas**. Após a exposição, a discente foi arguida oralmente pelos membros da Comissão Examinadora, tendo recebido o conceito final: APROVADA. Nada mais havendo, foi lavrada a presente ata, que após lida e aprovada, foi assinada pelos membros da Comissão Examinadora.

Prof. Dr. CARLOS FREDERICO DE OLIVEIRA GRAEFF

Profª. Drª. ALEJANDRA HORTENCIA MIRANDA GONZÁLES

Prof. Dr. FRANCISCO EDUARDO GONTIJO GUIMARÃES

Prof. Dr. ALEXANDRE FONTES DA FONSECA

Prof. Dr. ANDRÉ SARTO POLO

Bregadiolli, Bruna Andressa.

Estudo e desenvolvimento de materiais para aplicações em células solares híbridas / Bruna Andressa Bregadiolli, 2016

167 f. : il.

Orientador: Carlos Frederico de Oliveira Graeff

Tese (Doutorado)–Universidade Estadual Paulista. Faculdade de Ciências, Bauru, 2016

1. titanium dioxide. 2. fullerenes. 3. hybrid materials. I. Universidade Estadual Paulista. Faculdade de Ciências. II. Título.

THESIS

UNIVERSITE DE PAU ET DES PAYS DE L'ADOUR – UNIVERSIDADE ESTADUAL PAULISTA - BAURU

Defended on September 20th, 2016 by

Bruna Andressa BREGADIOLLI

Submitted in fulfilment of the requirements for the degree of

Doctor of Philosophy

in Chemistry at

UNIVERSITÉ DE PAU ET DES PAYS DE L'ADOUR

and

UNIVERSDADE ESTADUAL PAULISTA "JULIO DE MESQUITA FILHO"

"Study and development of materials for applications in hybrid solar cells"

Etude et développement de matériaux pour des applications en cellules solaires hybrides

Advisors: Dr. Roger C. HIORNS, and Prof. Carlos Frederico de Oliveira GRAEFF

JURY

Prof Alejandra Hortencia Miranda GONZÁLEZ	**Rapporteur**
Prof Alexandre Fontes FONSECA	**Rapporteur**
Prof André Sarto POLO	**Examinateur**
Prof Francisco Eduardo Gontijo GUIMARÃES	**Examinateur**

Fullerene Derivatives

Abstract

Main-chain fullerene polymers were prepared using a newly discovered dipolar azido cycloaddition polymerisation (DACAP). This first demonstration employs sterically cumbersome bis(azido-alkyl) comonomers to yield oligo- and poly(aziridinofullerene)s. The products were extensively characterized and devices were made in order to evaluate its behavior in organic photovoltaic devices. This new methodology opens a route to numerous main-chain fullerene polymers.

Publications

Ramanitra, H.H, Santos Silva, H., Bregadiolli B. A., Khoukh. A., Combe C.M.S., Dowland, S.A., Bégué, D., Carlos F. O. Graeff, C.F.O., Dagron-Lartigau, C, Distler, A., Morse, G., Hiorns, R.C. Synthesis of Main-Chain Poly(fullerene)s from a Sterically Controlled Azomethine Ylide Cycloaddition Polymerization Macromolecules, 2016, 49 (5), pp 1681–1691 DOI: 10.1021/acs.macromol.5b02793

Ramanitra, H.H., Dowland, S.A., Bregadiolli, B.A., Salvador, M. Santos Silva,H., Bégué, D., Graeff, C.F.O., Peisert, H., Chassé, T. Rajoelson, S., Osvet, A., Brabec, C.J., Egelhaaf, H.J. Morse, G., Distler, A., Hiorns, R.C. Increased Thermal Stabilization of Polymer Photovoltaic Cells with Oligomeric PCBM. Journal of Materials Chemistry C, Accepted Manuscript DOI: 10.1039/C6TC03290G

Part of the results will be published in:

Bregadiolli, B. A., Corcoles, L., Kang, L., Ramanitra, H.H., Combe, C.M.S., Ferreira, R.M., Santos Silva, H., Bégué, D., Lavada, F.C., Dagron-Lartigau, C., Luscombe, C.K., Olivati, C., Graeff, C.F.O., Hiorns, R.C. Syntheses of Main-chain Poly(aziridinofullerene)s and their use in Organic Photovoltaic Devices.

Santos-Silva, H., Ramanitra, H.H.; Bregadiolli, B.A.; Bégué, D.; Graeff, C.F.O; Dagron-Lartigau, C.; Peisert, H.; Chasse, T.; Hiorns, R.C. Regioregular Oligo- and Poly(fullerene)s for Photovoltaic Applications: Modelled Electronic Behaviours and Synthesis

The research leading to fullerene results has received funding from the European Union Seventh Framework Program (FP7/2011) under grant agreement no. 290022, the Region Aquitaine under grant FULLINC 2012. LC acknowledges financial support from the Ministry of Economy and Competitiveness of Spain (FPI grant MAT2012-37776). LNNano (CNPEM - Brazil) is thanked for providing gold IDE. LK and CKL acknowledge support from the National Science Foundation (DMR 1407815 and CHE 1506209) as well as the State of Washington through the University of Washington Clean Energy Institute Exploratory Fellowship Program. Dr. M. Pédeutour is warmly thanked for administrative support.

Inorganic Oxide

Abstract

TiO_2 derivatives with distinct morphologies have been successfully obtained by microwave assisted hydrothermal synthesis in acidic and alkaline medium using mild conditions. Titanium tetraisopropoxide (TTIP) was used as precursor in different environmental conditions with low temperatures and short synthesis time. XRD, SEM, EDX, TEM and BET were used to characterize the microstructural properties of the oxides. In the acidic synthesis the reaction time and temperature are not accompanied by significant changes in the structure of the material. However, in the basic conditions, the concentration of Na^+ ions strongly influences the particle morphology and growth. The morphology of the nanoparticles shows irregular spheres in acidic conditions, while in alkaline medium, needle-like structures are formed as well as aggregated nanotube-like structures synthesized in only 30 min. Besides the difference in the morphology and structure, in both systems, high surface area was obtained.

Publications

González, A.H.M., Machado Junior, C., Bregadiolli, B.A., de Farias, N.C., D'Alpino, P.H.P; Graeff, C.F.O. New Materials for Energy and Biomedical Applications. Ceramic Engineering and Science Proceedings. 1ed.: John Wiley & Sons, Inc., 2013, v. , p. 1-13.

Da Silva, B.H.S.T., Bregadiolli, B.A., Graeff, C.F.O., Silva-Filho, L.C. $NbCl_5$-Promoted synthesis of novel fluorescein dye derivatives: Spectroscopic and Spectrometric characterization and its application in dye-sensitized solar cells. Accepted Manuscript DOI: 10.1002/cplu.201600530

Part of the results will be published in:

Bregadiolli, B. A., Fernandes, S.L., Graeff, C. F. O., Easy and fast preparation of TiO_2 nanotubes and nanoparticles using different environmental conditions by microwave assisted hydrothermal technique.

Hybrid Nanoparticles

Abstract

This work consists in the synthesis and characterization of TiO_2 and Nb_2O_5 nanoparticles grafted P3HT. Hybrid nanoparticles, core@shell of metallic oxides and P3HT were synthesized. The optical and structural properties of hybrid nanoparticles (TiO_2@P3HT and Nb_2O_5@P3HT) were investigated. The physical and morphological properties have been characterized using TEM, where a homogeneous P3HT shell is observed onto the particles. Photoluminescence measurements reveal a blue shift and quenching of intensity in the emission spectrum of the grafted particles. Those phenomena would be explained by the annihilation of the excitons by polarons at the polymer/oxide interface.

Part of the results will be published in:

Bregadiolli, B. A., Awada, H, Nunes Neto, O., Dagron-Lartigau, C., Bilon, L., Bousquet, A., Hiorns R.C., Batagin-Neto, A., Guimarães, F. E. G., Graeff, C. F .O, Exciton-polaron annihilation in hybrid systems studied by FLIM-confocal microscopy. – in preparation

CBMM is thanked for provide $NbCl_5$.

.

This work is dedicated to my parents Amadeu and Maria Helena

Acknowledgments

I would like to give my sincere acknowledgment to:

My supervisors: Prof. Dr. Carlos F. O. Graeff for all the support, fruitful discussions and opportunities during all this work and Dr. Roger C. Hiorns for the support and patience for the thousand Skype meetings and discussions to improve this thesis.

My friends from the LNMD and from EPCP group (IPREM – UPPA) - the ones who are there and the ones who already left - for the contributions in this work. In special Sílvia Fernandes, João Vitor Paulin, Oswaldo Nunes Neto, Erika Bronze-Uhle, Augusto Batagin Neto, Marina Piacenti and Gustavo Albano.

Dr Alejandra Hortencia Miranda Gonzalez and Dr Luiz Carlos da Silva Filho for all the help since the beginning of the project and the contributions in the Exame Geral de Qualificação. Prof Francisco Carlos Lavarda and Ms Rodrigo Marques Ferreira for the simulation results and Dr Christine Luscombe's group for the solar cells preparation and measurements. Dr Antoine Bousquet and Dr Hussein Awada (IPREM – EPCP) for the contributions to synthesize the hybrid nanoparticles. Professor Francisco Eduardo Gontijo Guimarães – IFSC/USP for the FLIM measurements, Dr Luiz Alberto Colnago - EMBRAPA - São Carlos for the relaxometry measurements and Professor Clarissa Olivatti (DFQB - Unesp – Presidente Prudente) for the conductivity measurements. My first advisor Professor Marcelo Nalin who presented me the research world and had guided my first steps.

My family, in special my nephew Davi for the happiness moments and my partner Glauco for the patient and love.

FAPESP (2011/02205-5) and CAPES (BEX 11216-12-3) for the scholarship.

BREGADIOLLI, B. A., **Study and development of materials for applications in hybrid solar cells**. 2016. 167f. Thesis (PhD in Science and Technology of Materials) - UNESP and (PhD in Polymer Chemistry) - UPPA, Bauru, 2016.

ABSTRACT

This work aims to study and develop materials for applications in third generation solar cells. The synthesized materials are fullerene derivatives, titanium oxide, and hybrid (polymer@oxide) nanoparticles. The fullerene derivatives, n-type polymers, were designed to contain C_{60} in the main chain. Different products were obtained, varying the comonomer alkyl length using a new polymerization route discovery in this work. The photovoltaic devices were prepared using the bulk heterojunction configuration and the highest efficiency reached was 1.84 %, representing a very promising performance for a novel material. The titanium dioxide nanoparticles were synthesized using microwave assisted hydrothermal technique in different reaction condition, such as pH, temperature and time, in order to obtain well defined nano-sized morphologies, high yields and high surface areas. Also, it was investigated the influence of the Na^+ ions on the crystalline growth and morphologies of the oxides, where nanoparticles, needles and nanotube-like structures were obtained. The hybrid nanoparticles were synthesized using the prepared oxides and a P3HT functionalized in order to bond covalently with the oxides. The nanoparticles were optically characterized and concluded to be possible to use for studies of charge transfer in hybrid systems.

Keywords: TiO_2, microwave assisted hydrothermal, fullerene derivatives, Poly(azafulleroid)s, grafted nanoparticles.

BREGADIOLLI, B. A., **Estudo e desenvolvimento de materiais para aplicações em células solares híbridas**. 2016. 167f. Tese (Doutorado em Ciência e Tecnologia de Materiais) – UNESP e (Doutora em Química de Polímeros) – UPPA, Bauru, 2016.

RESUMO

Este trabalho tem como objetivo estudar e desenvolver materiais para aplicações em células solares de terceira geração. Os materiais sintetizados são derivados de fulereno, óxido de titânio e nanopartículas híbrido (óxido@polímero). Os polímeros derivados de fulereno, de tipo *n*, foram planejados para conter C_{60} na cadeia principal. Três produtos diferentes foram obtidos, variando o comprimento da cadeia alquílica do co-monômero utilizando uma nova rota de polimerização. Os dispositivos fotovoltaicos foram preparados utilizando a configuração de heterojunção no volume e a maior eficiência alcançada foi de 1,84 %, o que representa um desempenho promissor para um novo material. As nanopartículas de dióxido de titânio foram sintetizadas usando a técnica hidrotermal assistida por micro-ondas em diferentes condições reacionais, tais como pH, temperatura e tempo, de modo a obter a morfologia nano dimensionada bem definida, rendimentos elevados e alta área superficial. Além disso, estudou-se a influência dos íons Na^+ no crescimento cristalino dos óxidos e em sua morfologia, onde foram obtidas nanopartículas, estruturas tipo agulas e estruturas tipo nanotubos. As nanopartículas híbridas foram sintetizadas utilizando os óxidos sintetizados e um polímero, P3HT, funcionalizado de modo a ligar-se covalentemente aos óxidos. As nanopartículas foram opticamente caracterizadas e concluímos que estas podem ser utilizadas para estudar a transferência de carga em sistemas híbridos.

Palavras chaves: TiO_2, hidrotermal assistido por micro-ondas, derivados de fulerenos, poli(azafuleroide)s, nanopartículas enxertadas.

BREGADIOLLI, B. A., **Etude et développement de matériaux pour des applications dans les cellules solaires hybrides.** 2016. 167f. Thèse (Docteur en Science et Technologie des Materiaux) – UNESP et (Doctorat en Chimie des Polymères)- UPPA, Bauru, 2016.

RÉSUME

Ce travail vise à étudier et à développer des matériaux pour des applications dans les cellules solaires de troisième génération. Les matériaux synthétisés sont des dérivés de fullerène, l'oxyde de titane et des nanoparticules hybride (polymère@oxyde). Les polymères dérivés de fullerène, de type n, ont été conçues pour contenir C_{60} dans la chaîne principale. Trois produits différents ont été obtenus, en faisant varier la longueur du comonomère en utilisant une nouvelle voie de polymérisation. Les dispositifs photovoltaïques ont été préparés en utilisant la configuration à hétérojonction en vrac et le rendement le plus élevé atteint était de 1,84 %, ce qui représente une performance prometteuses pour un nouveau matériau. Les nanoparticules de dioxyde de titane ont été synthétisés en utilisant la technique hydrothermique assistée par micro-ondes dans différentes conditions de réaction, tels que le pH, la température et le temps, afin d'obtenir ainsi défini nanométrique morphologie, avec des rendements élevés et une grande surface spécifique. En outre, on a étudié l'influence des ions Na^+ sur la croissance cristalline des oxydes et morphologies des oxydes, où c'etait obtenu des nanoparticules, des aiguilles et des structures ressemblant des nanotubes. Les nanoparticules hybrides ont été synthétisés en utilisant l'oxyde synthétisé et un polymére, P3HT, fonctionnalisés afin de lier de manière covalente avec les oxydes. Les nanoparticules sont optiquement caractérisés et ont conclu à être possible d'utiliser pour les études de transfert de charge dans les systèmes hybrides.

Mots-Clés: TiO_2, hydrothermal assistée par micro-ondes, les dérivés de fullerène, poly(azafuleroide)s, greffé nanoparticules.

LIST OF FIGURES

LIST OF TABLES

LIST OF SCHEMES

ABBREVIATIONS

ATRAP	Atom-transfer radical-polymerization
BET	N_2 adsorption at 77 K – Brunauer Emmett Teller
CV	cyclic voltammetry
DEA	diethanolamine
DMF	dimethylformamide
DSSC	dye sensitized solar cell
DTPA	diethylenetriaminepentaacetic acid
EA	ethanolamine
EDA	ethylenediamine
EDTA	ethylenediaminetetraacetic acid
EDX	energy dispersive X-ray spectroscopy
EPA	exciton-polaron annihilation
FF	fill factor
FLIM	fluorescence-lifetime imaging microscopy
FTIR	Fourier transformed-infrared spectroscopy
FWHM	full width at half maximum
GPC	gel permeation chromatography
HOMO	highest occupied molecular orbital
IDA	iminodiacetic acid
LUMO	lowest unoccupied molecular orbital
M_n	number average molecular weight
M_w	weight average molecular weight
N3	dye (cis-Bis(isothiocyanato) bis(2,2'-bipyridyl-4,4'-dicarboxylato ruthenium(II))
N719	dye (di-tetrabutylammonium cis-bis(isothiocyanato)bis(2,2'-bipyridyl-4,4'-dicarboxylato)ruthenium(II))
NMR	nuclear magnetic resonance spectroscopy
o-DCB	ortho-dichlorobenzene
OPV	organic photovoltaic

P3HT	Poly(3-hexylthiophene-2,5-diyl)
PAF	poly(aziridinofulerene)
PCBM	[6,6]-phenyl-C_{61}-butyric acid methyl ester
PCE	power conversion efficiency
PEDOT	poly(3,4-ethylenedioxythiophene)
PL	photoluminescence
PPV	poly(p-phenylene vinylene)
PSS	polystyrene sulfonate
PVA	polyvinyl alcohol
RT	room temperature
SACAP	sterically controlled azomethine ylide cycloaddition polymerization
SC	solar cell
SEC	size exclusion chromatography
SEM	scanning electron microscopy
TBA	tetraethylammonium
TCO	transparent conducting oxide
TEA	tetraethylammonium
TEAOH	tetraethylammonium hydroxide
TEM	transmission electron microscopy
TG	thermogravimetric analysis
THF	tetrahydrofuran
TTIP	titanium (IV) isopropoxide
UV-Vis	Spectroscopy in the UV-Visible region
XRD	X-ray diffratometry
Z907	dye (bis(isothiocyanato)(4,4'-dicarboxylato-2,2'-bipyridine)(4,4'-dinonyl-2,2'-bipyridine)ruthenium(II))

SUMMARY

FOREWORD

This thesis is about the results obtained from October 2011 to September 2016 in a *Doutorado Direto* project in a co-tutelle thesis agreement between Universidade Estadual Paulista "Júlio de Mesquita Filho" (UNESP) and Université de Pau et des Pays de l'Adour (UPPA). The research was conducted most of the time at *Laboratório de Novos Materiais e Dispositivos* (LNMD) of *Departamento de Física – Faculdade de Ciências* at UNESP (Bauru - SP, Brazil) under supervision of Professor Carlos Frederico de Oliveira Graeff. The period in Brazil was supported by FAPESP (2011/02205-3). A research period at *Equipe Physique et Chimie des Polymères* (EPCP) of *Institut des Sciences Analytiques et de Physico-chimie pour l'Environnement et les Matériaux* (IPREM) in UPPA (Pau, France), under supervision of Dr. Roger Hiorns from January to December 2013 was funded by the Project CAPES/COFECUB (BEX 11216-12-3). Considering the contribution of the period abroad in this PhD research, the agreement for the international joint supervision of thesis between the Brazilian and French universities was approved. The thesis is divided into 5 chapters that are briefly described below:

A brief description of the issue addressed in this thesis, such as the main materials use in third generation photovoltaics, is presented in Chapter 1. Chapter 2 describes the characterization techniques and its conditions used in this work. Chapter 3 presents a structural and opto-electrical characterization and application as electron acceptor in OPV of the fullerene derivatives synthesized. Chapter 4 describes the work on TiO_2. Lastly in Chapter 5 is demonstrated the hybrid nanoparticles synthesis of TiO_2 or Nb_2O_5 oxide with P3HT. The grafted TiO_2@P3HT and Nb_2O_5@P3HT are characterized by structural and morphological properties. In addition, a deeply study in its optical properties were performed using FLIM characterization in order to better understand their charge transport characteristics.

CHAPTER 1

INTRODUCTION: MATERIALS FOR THIRD GENERATION PHOTOVOLTAICS

In order to supply the growing demand of electricity consumption, the use of renewable energies, such as photovoltaic cells – solar cells (SC), is rising as a promising option as a form of clean and efficient energy to reduce the use of fossil fuels as non-renewable and polluting (MOULE, 2012). Nevertheless, photovoltaics do not have significant participation in the Brazilian energy matrix (AMBIENTE, 2012). The main reason for the low participation of photovoltaic devices in the energy market is still high cost of energy produced from such devices (ENERGIA, 2012), since the current industry involves devices as silicon-based and single and multi-junction, due to its high efficiency in power conversion (FRAUNHOFER INSTITUTE FOR SOLAR ENERGY SYSTEMS, 2015) with efficiencies of 15 to 25 % (FRAUNHOFER INSTITUTE FOR SOLAR ENERGY SYSTEMS, 2015).

The first SCs were constructed by Charles Fritts in 1890 (ZACHARY A. SMITH, 2008). They used selenium as a semiconductor and thin layers of gold to form the junctions. The model was improved by Russell Ohl in 1941 (ZACHARY A. SMITH, 2008). He developed the first silicon cell, now known as first generation solar cells, which consist mainly of bulk crystalline silicon p-n junctions. The first generation of SC was the dominant technology in terms of commercial production, until the advent of the single and multi-junction solar cell (FRAUNHOFER INSTITUTE FOR SOLAR ENERGY SYSTEMS, 2015).

The second generation of SC uses thin films as semiconductors. Many materials are employed in this devices, such as amorphous silicon, silicon polycrystalline or microcrystalline and cadmium telluride (REYNOLDS, 1954). Thin film technologies were chosen in order to reduce the amount of material required to production and therefore costs. Nowadays, the single and multi-junctions devices have the best research efficiencies, as observed in the efficiency chart in the Figure 1.

Figure 1: Best research-cells efficiencies chart.

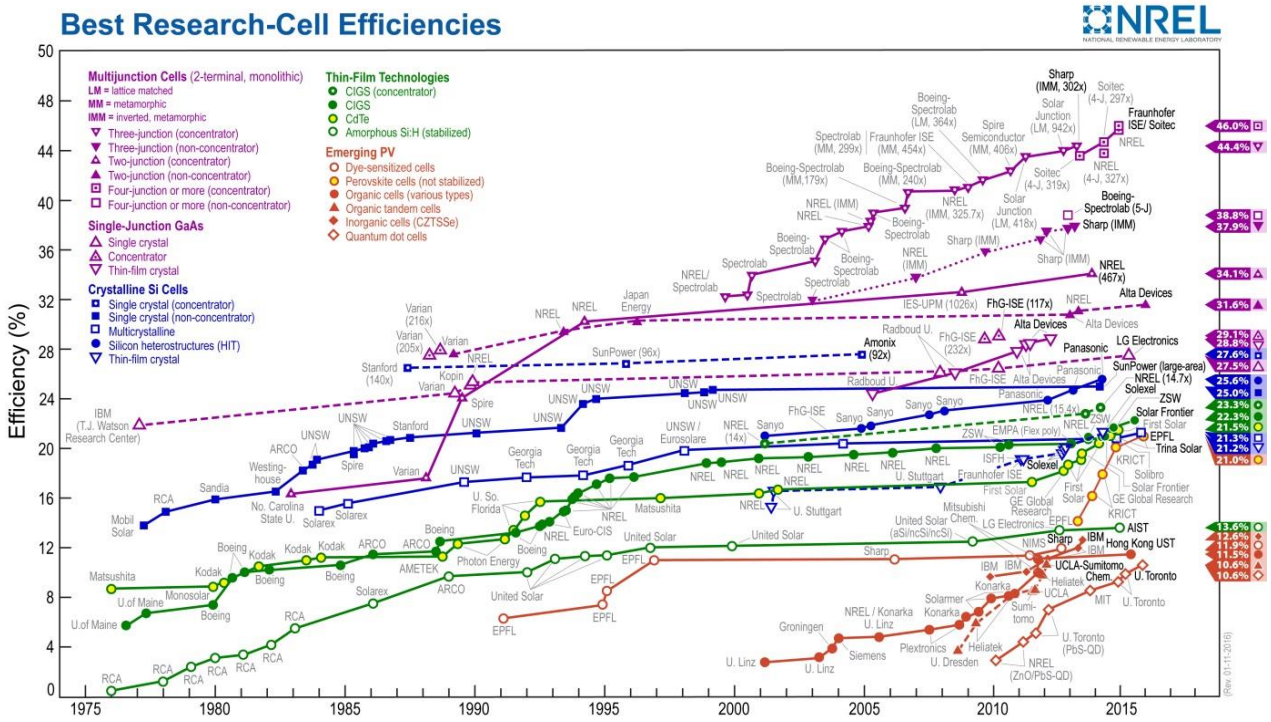

From: http://www.nrel.gov/ncpv/images/efficiency_chart.jpg (May 2016)

The third generation of solar cells are devices that are potentially able to overcome the Shockley–Queisser limit of 31–41 % power efficiency for single bandgap solar cells. Theoretically, an infinite number of junctions would have a limiting efficiency of 86.8% under highly concentrated sunlight. (SHOCKLEY, 1961; CONIBEER, 2007). Common third-generation systems include multi-layer cells made of amorphous silicon or gallium arsenide and dye-sensitized (DSSC), organic, polymer and perovskite solar cells.

This work will focus in materials for hybrid (DSSC) and organic (bulk heterojunction) systems. These SCs have low energy conversion efficiency, from 10 – 13 % as observed in Figure 1, but they are good candidates for the current market due to their high optical absorption, ease of processing, allowing production on an industrial scale and good cost benefits (J. CHANDRASEKARAN, 2011). Therefore, research into hybrid systems aims to maintain the low cost of production with the differential to combine semiconductor, optical and electrical

properties of inorganic materials with properties as mechanical resistivity and easy processability of organic compounds, such as polymers and presents great potential in energy conversion efficiency (REYNOLDS, 1954; ARICI, 2003; SHAHEEN, 2005; J. CHANDRASEKARAN, 2011).

1.1 Dye Sensitized Solar Cells (DSSC)

The dye sensitized solar cells (DSSC), also known as Grätzel solar cells, were firstly developed by Professor Michael Grätzel team in Switzerland in 1991 (B. O´REGAN, 1991). In this kind of device, the photoanode is made by a porous film of a semiconductor material deposited on a transparent conducting oxide (TCO) and sensitized by a dye. The positive terminal of the cell, the cathode, is coated with a catalytic material such as platinum layer on TCO. The electrolyte, usually an iodide/triiodide redox pair solution, is interposed between the two electrodes. Specifically, in a DSSC device, the photon of light incident is absorbed by the dye, generating a photo-electron that is injected into the conductive band of the nanocrystalline semiconductor, as presented in Figure 2. The electron diffuses to the negative electrical contact through a circuit and is collected by the cathode, in which, with the aid of the catalyst, enables the reduction reactions of the electrolyte. The dye molecule is oxidized to reduced state original redox couple through a liquid within the pores of electrode (B. O´REGAN, 1991; GRATZEL, 2001; GRÄTZEL, 2003).

Figure 2: The electron injection process and energy levels diagram of a DSSC.

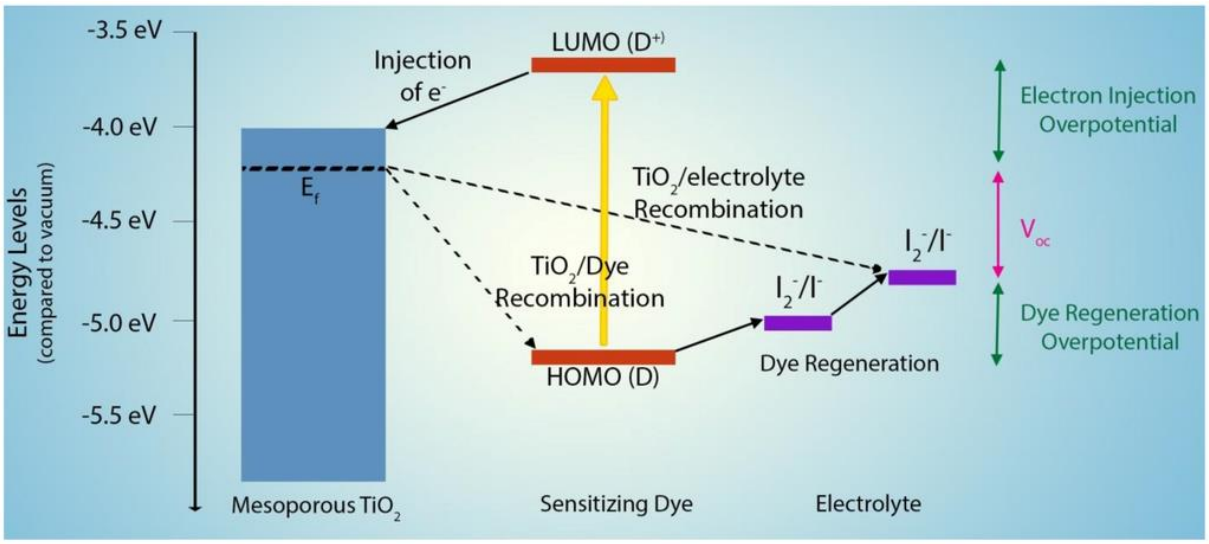

From: http://www.mdpi.com/2072-666X/5/2/171/htm#B117-micromachines-05-00171

The dyes most used in DSSC are ruthenium complexes, such as N3, N719 and Z907 (YE, 2015). Those materials are very effective due to their intense absorption in the whole visible range. However, these complexes contain Ru as a heavy metal, which is undesirable from environmental and cost aspects. Alternatively, natural dyes such as phthalocyanines and anthocyanins, can be used for the same purpose with great availability, low cost and an acceptable efficiency, up to 1.7% (HALME, 2010; NARAYAN, 2012). The electrolyte is responsible for the inner charge carrier transport between electrodes and continuously regenerates the dye and itself during DSSC operation (WU, J., 2015). Also, the semiconductor film plays an important role in the device efficiency (JOSE, 2009; DHAS, 2011). It should be composed of a material with adequate energy levels and morphology. So far, the most used materials are metal oxides such as TiO_2 and ZnO (QUINTANA, 2007). Properties such as particle size, surface area, good adhesion to the substrate and appropriate morphology to promote greater interaction dye/oxide are desirable (JOSE, 2009). Thus, a depth study of the

properties of these materials is crucial role in the performance of devices (M. M. RASHAD, 2012).

Since TiO_2 has been the material of choice for the development of the first DSSC and a fundamental material for photovoltaic devices, this oxide was used as subject of this PhD thesis. In this work, we will focus on the synthesis and characterization of TiO_2 with different morphologies synthesized by microwave assisted hydrothermal technique.

1.2 TiO_2

Nanocrystalline titania (TiO_2) has been intensively investigated due to its numerous applications in many fields such as photocatalysis, photovoltaic cells and gas sensors (CHEN, X., 2007). It is cheap, abundant, chemically stable and a multi-functional material. The properties of TiO_2 are significantly dependent on the crystalline phase (anatase, rutile or brookite, illustrated in Figure 3). Wherein, anatase and rutile have a significant role in industrial applications. Experimental data on TiO_2 brookite is limited due to its rarity and difficult preparation (LANDMANN, 2012). The rutile phase is typically found in mineral form, being the thermodynamically stable phase. Anatase has a low electron hole recombination rate and due to its high photoactivity is believed to be the most favorable phase for solar energy conversion (CHEN, D., 2009) and photocatalysis (ISMAIL, 2011). It is a n-type semiconductor with an indirect band gap of 3.2 eV (TANG, 1995). Particle size has great influence on the structure and properties of TiO_2. In the nanometric regime, anatase is the most stable polymorph (DAR, 2014).

Figure 3: TiO_2 crystalline structure for a) rutile, b) anatase and c) brookite. Oxygen atoms represented in red and titanium in white.

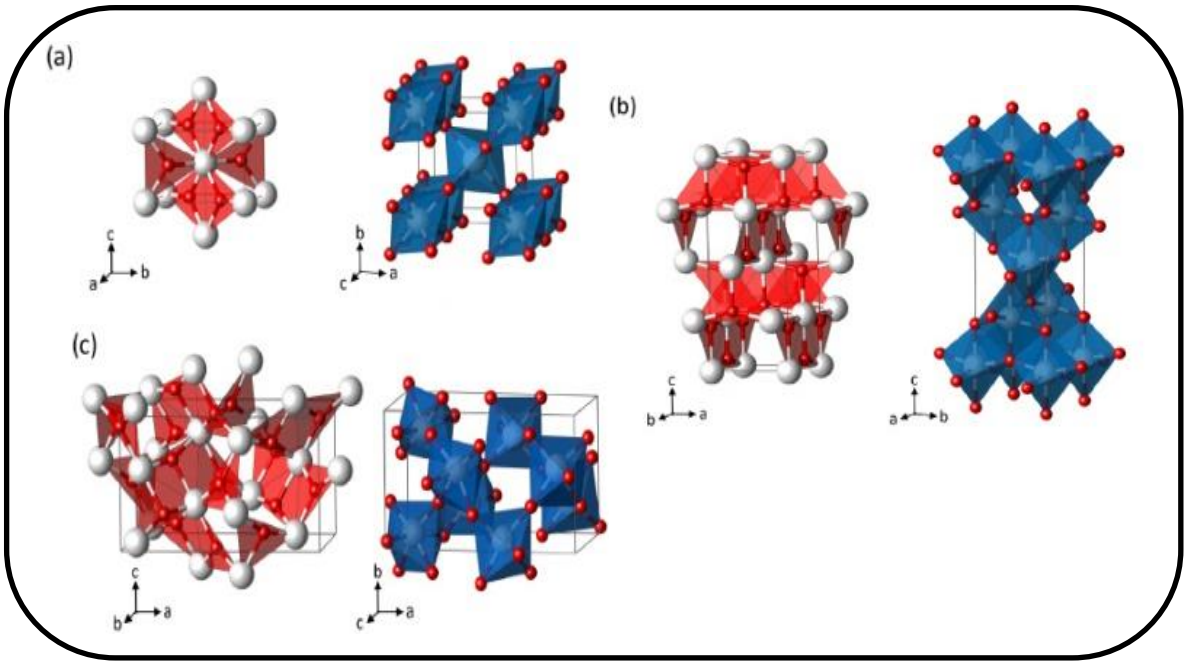

From: Adapted of Landman *et al.* 2012. (LANDMANN, 2012)

The chemical structure of TiO_2 is composed by an octahedron with Ti^{+4} ion in the center, surrounded by six atoms of O^{-2}. Anatase and rutile crystalline phases differ in the number of atoms per unit cell; anatase has four molecules TiO_2 and rutile two. Consequently, the anatase structure is more bulky, elongated and less dense than the rutile (CHEN, X., 2007). Furthermore, the anatase phase, due to its structure, has low recombination rate of the electron-hole system (DHAS, 2011). Nanostructured anatase TiO_2 electrodes are believed to be essential for achieving high conversion efficiencies and good long-term stability in DSSCs. Although there is no generally accepted explanation, this fact is commonly attributed to the structure and chemical composition of the TiO_2 surface in this particular phase. (MUNIZ, 2011) The particle size has great influence on the device efficiency: small particle size have a greater surface area, which optimizes charge transfer process to the surface and decreases the recombination of charges in the bulk, and increase the contact surface with the dye (LANDMANN, 2012). Also,

anatase nanoparticles with 10 - 20 nm could result in transparent pastes (ITO, S., 2007). Surface area is another important parameter once large surface area is needed for sufficient dye loading. Thus, for each application, careful tailoring of specific properties such as phase composition, surface area and morphology is requested.

Several TiO_2 nanostructures such as spheres (DAR, 2014), nanorods (MELCARNE, 2010) and nanotubes (BAVYKIN, 2006; LIU, N., 2014) have been synthesized using different techniques like sol-gel, electrochemical, sonochemical and hydrothermal (BAVYKIN, 2006; OU, 2007). Hydrothermal synthesis is an environmentally friendly methodology to synthetize nanostructured materials (MAO, 2007). The starting material, synthesis conditions and processing can drastically change the end material. For example, Kim et al, (KIM, D.S., 2007) obtained well-defined spherical mesoporous TiO_2 prepared from Titanium(IV) isopropoxide (TTIP). Kasuga et al. (KASUGA, 1998) has obtained titanates nanotubes from TiO_2 nanopowder with high concentrations of NaOH. The hydrothermal synthesis is typically done using an autoclave with Teflon liners under controlled temperature and/or pressure in aqueous solutions (JIANG, 2006; CHEN, X., 2007; CHEN, D., 2009; NAKAHIRA, 2010). Despite its advantages, the synthesis can take several hours to be completed (CORRADI, 2005). Microwave assisted reactions were found to reduce the hydrothermal synthesis time of TiO_2 by typically 1/3 (CORRADI, 2005; MANFROI, 2014; SHEN, 2014), and in addition can produce single crystal, with less waste and lower temperatures. TTIP is commonly used in conventional and microwave assisted hydrothermal synthesis of TiO_2 under acid conditions (BAVYKIN, 2006; CHEN, X., 2007; OU, 2007; ISMAIL, 2011; LIU, N., 2014; PANG, 2014), but less in alkaline (SAPONJIC, 2005).

Another important characteristic of nanomaterials is the morphology. The size and shape of the nanocrystals, as well as the surface topography is the key to increased electron capture efficiency. Several studies have been conducted to the size control and forms of these

nanocrystals and their influence on devices (CHEN, X., 2007; VITTADINI, 2007; HUANG, C.-H., 2011; XIN, 2011). The morphology control of nanomaterials mainly occurs during the synthesis. However, the synthesis of nanoparticles is not a trivial task. These can be obtained from colloidal suspensions, using several different techniques and methods. Table 1 and 2 present some works about the synthesis of TiO_2 using hydrothermal and microwave assisted hydrothermal technique in acid and alkaline conditions.

Table 1: Brief summary of TiO_2 derivatives synthesized by hydrothermal and microwave assisted hydrothermal in acidic media.

Reactants	Synthetic conditions	Nanoparticles characteristics	Reference
TTIP, complexing agents EDTA, DTPA and IDA, and the alkalis TEA, EDA, EA, DEA and TEAOH.	Sol-gel followed by microwave assisted hydrothermal using 900 W, 140 °C, 5 - 7 bar during 1 to 20 min.	Variable diameter and nanoparticles in anatase phase with 5-45 nm with irregular shape.	Arin *et al.*(ARIN, 2013)
$TiCl_4$, H_2SO_4, hydrochloric acid 2 M.	Microwave assisted hydrothermal using 300 W, 120 to 180 °C and from 30 to 120 min.	Anatase aggregated nanoparticles with spherical form and particle sizes similar in all tested conditions.	Baldassari *et al.* (BALDASSARI, 2005)
TTIP, propylamine, KCl and ethanol.	Sol-gel followed by microwave assisted hydrothermal at 200 °C, 280 psi and 260 W for 80 min.	Mesoporous spherical nanoparticles with diameter of 400 to 600 nm with nanocrystals of 10 nm as building blocks and surface area of 132.49 $m^2 \cdot g^{-1}$.	Chen *et al*. (CHEN, P., 2013)
$TiOCl_2$ in water.	Hydrothermal and microwave assisted hydrothermal at 195 °C from 1 to 32 h for conventional system and 5 min to 1 h using the microwave.	Regardless of the synthetic method was obtained rutile as the predominant phase. The microwave synthesis gave aggregated particles with spherical morphology of ~ 10 nm and conventional synthesis yielded larger acicular crystals, 50 to 100 nm.	Corradi *et al.* (CORRADI, 2005)
Commercial TiO_2 nanoparticles (P25) and 2-propanol in water and HNO_3.	Hydrothermal at 200 °C for 15 h and microwave assisted hydrothermal at 145 °C from 5 to 360 min.	Anatase thin films with surface area from 140 to 300 $m^2.g^{-1}$.	Wilson *et al.* (WILSON, 2006)
TTIP in ethanol and water with acetic acid as catalyst.	Particles synthesized by sol-gel, followed by microwave assisted hydrothermal at 225 and 450 °C using 400 ± 50 W e 425 ± 75 W.	Similar crystallinity in anatase phase for all conditions used.	Hart *et al.* (HART, 2004)
$TiCl_4$, ethanol and citric acid.	Sol-gel followed by microwave assisted hydrothermal at 120 to 180 °C from 30 to 120 min.	Mesoporous anatase nanoparticles with size from 5 to 7 nm and surface area from 217 to 323 $m^2 \cdot g^{-1}$.	Huang *et al*. (HUANG, C.-H., 2011)

$TiCl_4$, HCl and water.	Microwave assisted hydrothermal at 190, 100, 50 and 250 psi, equivalent to 192, 164, 138 and 116 °C, respectively from 2 min to 2 h.	Rutile and anatase nanoparticles with different morphologies and yields from 25 to 95 %.	Komarneni *et al.* (KOMARNENI, 1999)
TTIP, water, hydrochloric acid and $NaHPO_4$–Na_2HPO_4,	Sol-gel followed by hydrothermal or microwave assisted hydrothermal at 240 °C, from 100 to 550 psi and from 1 to 2 h.	Anatase nanoparticles with brookite as secondary phase with size from 5 to 10 nm.	Lu *et al.* (LU, C.-W., 2014)

Table 2: Brief summary of TiO_2 derivatives synthesized by hydrothermal and microwave assisted hydrothermal in alkaline media.

Reactants	**Synthetic conditions**	**Nanotubes characteristics**	**References**
Homemade rutile and anatase powders with the addition of crystalline nanoparticles after sintering	Microwave assisted hydrothermal using 195 W for 90 min.	Nanotubes with internal width of 4.48 nm and 12.82 nm in diameter.	Xing Wu *et al.* (WU, X., 2007)
TiO_2 powder and aqueous NaOH.	Microwave assisted hydrothermal during 6 h.	Titanate nanotubes with high purity. Length up tens of μm and diameter of 7 nm.	Wang *et al.* (WANG, Y.-A., 2005)
Homemade TiO_2 and commercial TiO_2 (P25) in NaOH 10 M.	Microwave assisted hydrothermal using 195 W for 90 min.	Nanotubes with width of 8 to 12 nm and lengths from 200 to 1000 nm. Surface area of 145.8 $m^2 g^{-1}$.	Xing Wu *et al.* (WU, X., 2005)
Nanoparticles synthesized on the surface of a Ni substrate using commercial TiO_2, PVA and NaOH in aqueous media.	Microwave assisted hydrothermal using 150 to 200 °C for 3 to 5 h.	Nanotubes from 4 to 5 multilayers approximately 10 nm in width and tens of nm long.	Cui *et al.* (CUI, 2012)
Commercial anatase and rutile powders in NaOH 10 M.	Hydrothermal at 150 °C for 48 h and HCl washing until pH=7	Titanate with 8 to 11 nm width with 2 to 4 walls. Surface area from 222 to 267 $m^2 g^{-1}$.	Choi *et al.* (CHOI, 2010)

Commercial TiO_2 (P25) in 10 N NaOH.	Hydrothermal from 110 to 150 °C for 24 h and HCl 0.1 N washing until pH < 7.	Surface area from 207 to 399 $m^2 g^{-1}$.	Tsai *et al.* (TSAI, 2004)
TiO_2 nanopowders in solutions 5 to 10 M NaOH.	Hydrothermal at 110 °C for 20 h a 110 °C followed by 0.1 N HCl washing until pH < 7.	Needle like macrometer structures in anatase phase, nanotubes with diameter of 8 nm and length of 100 nm and surface area of 400 $m^2 g^{-1}$.	Kasuga *et al.* (KASUGA, 1998)
Commercial TiO_2 (P25) in 10 M KOH.	Microwave assisted hydrothermal using 500 W, 0.5 to 3 MPa (equivalent to 175 to 260 °C) for from 40 to 70 min.	TiO_2 nanowire in anatase phase with diameter from 5 to 10 nm and length from 500 nm to 2 μm.	Li *et al.* (LI, L., 2011)
Commercial anatase TiO_2 in 10 M NaOH.	Microwave assisted hydrothermal using from 130 to 200 °C from 30 to 4 h followed by washing until pH 6.	Titanate nanotubes, $Na_2Ti_6O_{13}$, few μm lenght and average of 11 nm diameter (130 °C / 4 h) and 20 nm (150 °C / 4 h).	Manfroi *et al.* (MANFROI, 2014)
Commercial rutile TiO_2 in 10 M NaOH.	Microwave assisted hydrothermal using 200 °C for 45 min, followed by 0.1 M HNO_3 washing.	Nanotubes in rutile phase with diameter of 3-10 m and surface area of 214 $m^2 g^{-1}$.	Huang *et al.* (HUANG, K.-C., 2013)
Commercial TiO_2 (P25), Ag–TiO_2 powder in 10 M NaOH.	Microwave assisted hydrothermal using 195 W, 150 °C for 4 h followed by 5 N HCl washing until pH ~7.	Multi-walled nanotubes titanates structures with a diameter from 8 to 10 nm and a length of some μm with surface area ranging from 52 to 130 $m^2 g^{-1}$.	Rodrigues-Gonzalez *et al.* (RODRÍGUEZ-GONZÁLEZ, 2012)

1.3 Hydrothermal and microwave assisted hydrothermal techniques

Hydrothermal synthesis has been widely applied to obtain advanced materials, since it allows the morphology control, high purity crystals and control of particle growth using relatively low temperatures (BYRAPPA, 2001a). The method is based on the formation of crystal structures by dissolution and crystallization process with single or heterogeneous-phase reactions in aqueous solution under pressure generated by the system (SU, 2006). This synthesis takes place in aqueous, gels or suspensions mediums denominated as precursor solutions. Also, mineralizers may be added to change the pH of the system and help solubilisation of the precursors and reaction kinetics. To control the dispersion and particle morphology, other reagents such as surfactants or peptizing agents may be added in the reaction (YANG, J., 2001). The reactor is an autoclave (BYRAPPA, 2001a) and it is an important item in the synthesis, and it can variate according with the final objective product and the synthetic environment, however, it must satisfy the following characteristics (BYRAPPA, 2001b): i. be inert to acids, bases and oxidizing agents, ii. easy to assemble and disassemble, iii. having a sufficient length to the desired temperature gradient, iv. be leak-proof in working temperatures and pressures, and v. sturdy enough to withstand high pressures and temperatures in long-term experiments. For the synthesis of metal oxides, for example, typically are used Teflon-coated stainless steel reactors which could be externally heated. Currently, this synthesis method have been used for the synthesis of new materials and stages, stabilizing complexes, crystal growth from various inorganic compounds, the preparation of films, leaching of materials in the extraction of metals, synthetic organic materials among others (SU, 2006). The materials are obtained at low temperatures in a short treatment time and fewer processing steps, which makes economically viable, environmentally friend and industrially interesting technique.

In the 90s, Komarneni et al. combined microwave radiation with hydrothermal system for the synthesis of ceramic powders (BYRAPPA, 2001a). The development of this new synthetic route allowed the formation of oxides with different characteristics and properties (BALDASSARI, 2005). In general, the effects caused by microwave radiation are able to encourage chemical reactions that would not occur in conventional heating (BYRAPPA, 2001a; CORRADI, 2005). These effects result from the direct coupling of the material with microwaves, independent of temperature and reaction. Thus, the method is fast, clean and more economical than conventional hydrothermal and has received special attention due to advantages such as, rapid heating and temperature control, which leads to time and energy saving, increased reaction rate for one or two orders of magnitude, formation of new phases and selective crystallization (KOMARNENI, 1999; CORRADI, 2005; HUANG, C.-H., 2011; CUI, 2012; CHEN, P., 2013; ZHU, Y.-J., 2014).

In this work, we present an easy and fast route for TiO_2 nanostrucutres synthesis using microwave assisted hydrothermal technique in alkaline and acidic mediums. We demonstrate an environmentally friendly synthesis that uses mild conditions, low reaction times and temperatures and gives nanoparticles with different morphologies, high yield and high surface area. We have obtained titanate needle like particles after 30 min of synthesis using TTIP in alkaline media. The facility in producing these nanostructures, its reproducibility and low cost make it attractive for industrial applications.

1.4 Bulk heterojunction solar cells

Organic polymer-based photovoltaic devices (OPV) have attracted attention for their low cost, ease of processing, for being light, and even flexible, form of clean and renewable energy (LU, L., 2015). New organic precursors have achieved a power conversion efficiency of the

OPVs higher than 10%, as observed in Figure 1. Bulk heterojunction solar cells were firstly reported in 1995 (G. YU, 1995). Since then, much efforts has been made to improve the system (LU, L., 2015). In an organic photovoltaic cell a thin film of organic semi-conductor materials (polymers, oligomers or small molecules) acts as active layer. This layer is placed in between the TCO and a metal electrode, as presented at Figure 4. Materials having a delocalized π electron system can absorb sunlight, create photo-generated charge carriers and transport them (GÜNES, 2007b). Typically, the organic semiconductors are either having an electron donating (donors) or electron accepting (acceptors) properties. The active layer of this device is composed of both electron donor and acceptor materials (KAUR, 2014). For example poly(3-hexylthiophene) - P3HT, a p-type hole conducting material, works as electron donor, whereas phenyl-C_{61}-butyric acid methyl ester - PCBM and its derivatives show a n-type, electron conducting behavior and serve as electron-acceptor material (DANG, 2011).

Figure 4: Illustration of bulk heterojunction solar cell.

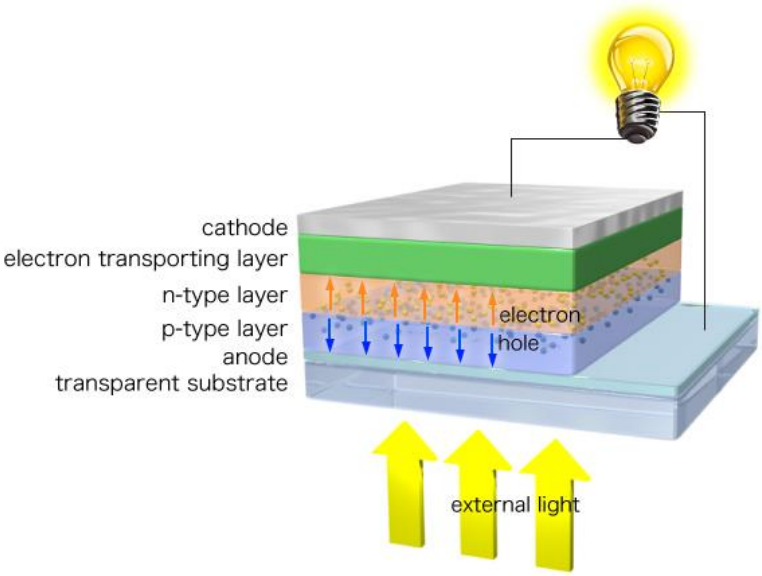

From: http://www.cstf.kyushu-u.ac.jp.

The organic solar cells work as follow: in photon absorption, an electron is excited from the HOMO to the LUMO. This electron-hole pair (exciton) relaxes with a binding energy between 0.1–1.4 eV (MAYER, 2007). The excitons must migrate to an interface where there is a sufficient chemical potential energy drop to drive dissociation into an electron-hole pair across the donor and acceptor (MIHAILETCHI, 2004; MAYER, 2007). The phase separation orientations in these devices are random and percolation paths of pure donor or acceptor material can connect the two electrodes. In its place, the current flow is controlled by the use of electrodes having sufficiently different work functions. Such that the anode electrode is chosen as a high work function material and the cathode selected as a low work function metal.

As the efficiency of a solar cell is dependent of the open circuit voltage (V_{oc}), short circuit current density (J_{sc}) and the fill factor (FF), Scharber *et al.* (SCHARBER, 2006) have predicted 10% as an attainable efficiency of a bulk heterojunction as a function of the band gap and the LUMO level of the donor, optimizing the LUMO level of the donor polymer optimizes the device's open circuit voltage and consequently the FF, having as high as possible charge carrier mobility of electrons and holes in the donor-acceptor blend, as illustrated in the Figure 5. As observed, it describes the efficiency of bulk-heterojunction solar cells that comprise a donor with a variable band gap in conjunction with an acceptor with a variable LUMO. For highest efficiencies, the difference between the LUMO levels needs to be 0.3 eV, and a band gap in the range of 1.2–1.7 eV, which would correspond to donor HOMO levels of –5.2 to –5.7 eV if the acceptor is PCBM (whose LUMO is assumed to be 4.3 ev). (DENNLER 2009)

Figure 5: Contour plot showing the calculated energy-conversion efficiency (contour lines and gray scale) versus the bandgap and the LUMO level of the donor polymer. Straight lines starting at 2.7 eV and 1.8 eV indicate HOMO levels of –5.7 eV and –4.8 eV, respectively. A schematic energy diagram of a donor PCBM system with the bandgap energy (E_g) and the energy difference (ΔE) are also shown.

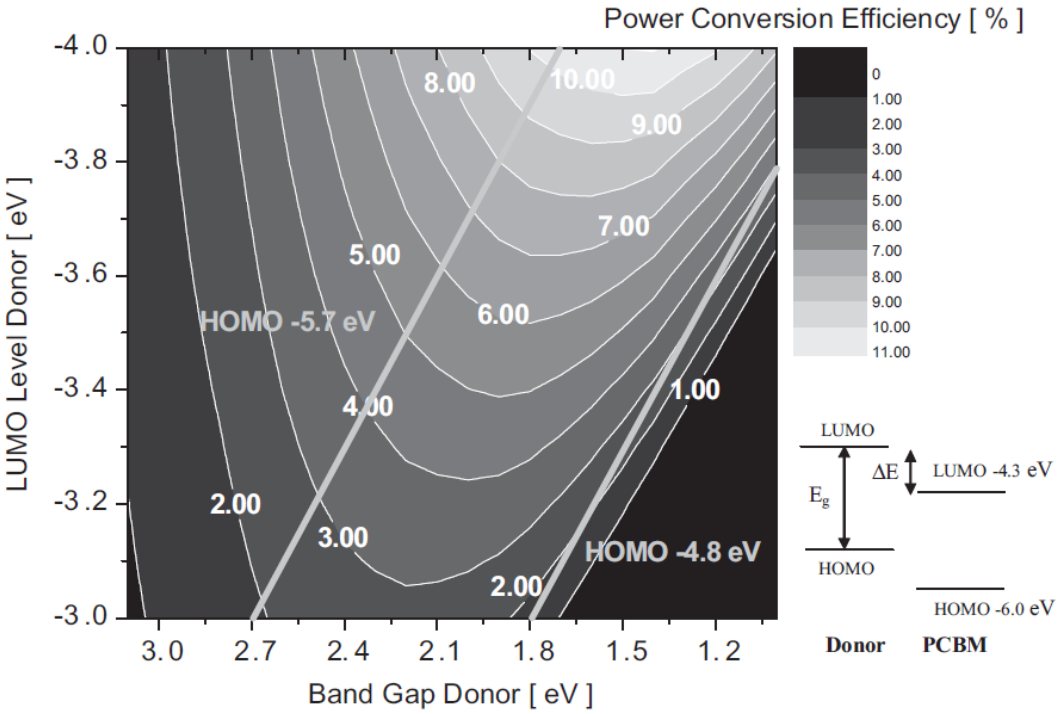

From: Adapted from (DENNLER 2009)

For this propose novel materials have been prepared to reach better performance and high efficiencies. Several strategies were investigated to increase the efficiency of solar cells. In this work, we are targeting a new n-type polymer based on fullerenes in the backbone. Fullerene is well-known as an excellent electron acceptor, and it is expected that its polymers will have good solubility to give rise uniform thin films.

1.5 Fullerenes

Fullerenes are a key topic on nanotechnology and industrial research nowadays. The high electron affinity and superior ability to transport charge make fullerenes the best acceptor component currently available (NAZARIO MARTIN, 2009). Fullerenes were discovered in 1985 by Kroto, Curl and Smalley (IIJIMA, 1991), and resulted in the Nobel Prize in Chemistry in 1996. It became available in notable amounts after 1990 with the preparation process of Krätschmer and Huffman (W. KRÄTSCHME, 1990). The energetically deep LUMO of fullerenes endows the molecule a very high electron affinity relative to the numerous potential organic donors. The triply-degenerate low LUMO of C_{60} and C_{70}, Figure 6, also allows the molecule to be reversibly reduced with up to six electrons, thus explaining its ability to stabilize negative charge (KAUR, 2014). The carbon atoms within a fullerene molecule are sp^2 and sp^3 hybridized, of which the sp^2 carbons are responsible for the considerably angular strain presented within the molecule. C_{60} has a localized π-electron system, which prevents the molecule from displaying superaromaticity properties.

Figure 6: Illustration of C_{60} and C_{70} structures.

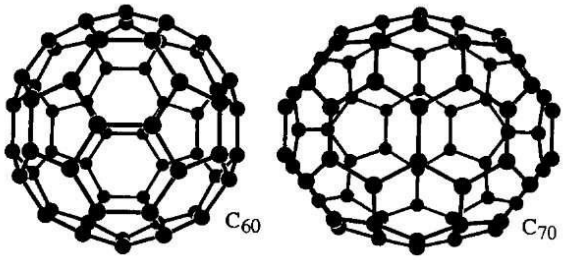

From: http://what-when-how.com/nanoscience-and-nanotechnology/nanocrystalline-materials-synthesis-and-properties-part-1-nanotechnology/

The development of chemical reactions able to modify the chemical structure of C_{60} led to new fullerene derivatives which exhibits a variety of outstanding electronic, magnetic,

conducting, superconducting, electrochemical and photo physical properties (NAZARIO MARTIN, 2009). The combination of the advantage of this molecule with the properties of other materials as polymers is very challenging. Combination of fullerenes and polymer chemistry is an interdisciplinary field in which all knowledge on the synthesis and study of natural as well as artificial macromolecules can be applied to fullerenes to achieve novel fullerene-based architectures with unprecedented properties and realistic applications (GIACALONE, 2006). Figure 7 shows the representation of some synthesized C_{60}-containing polymers.

Figure 7: Representation of C_{60}-containing polymers.

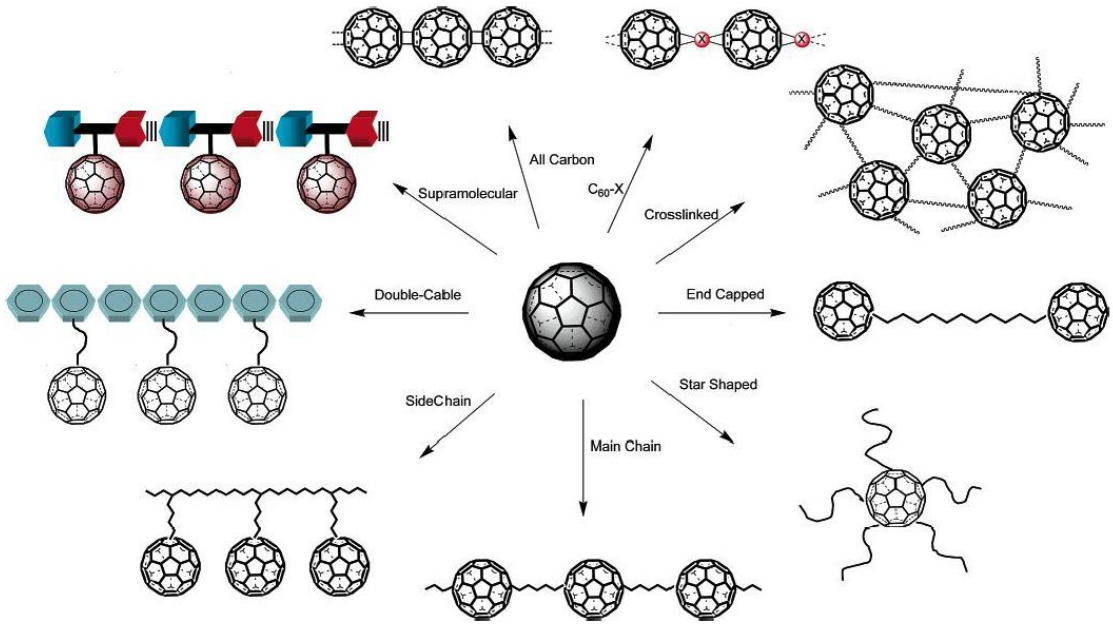

From: Giancalone *et al.*2006 (GIACALONE, 2006).

Nowadays, the chemical reactivity of C_{60} is well established, and a large number of fullerene derivatives have been prepared (GIACALONE, 2006). The extraordinary electronic properties of the fullerene C_{60} as an n-type semiconductor with relatively high carrier mobility have evoked continued interest in the development of a wide variety of chemically modified fullerene derivatives to application in organic devices, as solar cells (MILLER, 2006; LIAO,

2012; LI, C.-Z., 2013). Polymer solar cell advantages include low cost of fabrication, ease of processing, mechanical flexibility and versatility of chemical structure through advances in organic chemistry (GÜNES, 2007b; THOMPSON, 2008). The photo-charge generating layer is made from a blend of a semiconducting chromophoric electron donating p-type polymer, such as the standard bearer P3HT, and an acceptor n-type small molecule, typically $PC_{61}BM$ (HIORNS, 2006).

While much has been done to vary p-type materials, not least the introduction of the so-called low-band gap polymers to capture greater degrees of available light and reach efficacies greater than 10 % (BOUDREAULT, 2011; GREEN, 2014), relatively few papers deal with the modification of the fullerene derivative. $PC_{61}BM$ is widely used because of its excellent electron affinity and good charge mobility arising with crystallization (THOMPSON, 2008). However, it forms µm-scale crystals, through a thermally enhanced leaching process, that diminish device efficiencies (MOORE, 2013). Incorporating C_{60} into a polymer may permit stabilization of the active layer. Moreover, the creation of a metal-free method of polymerizing fullerene would expand the possibilities for use of C_{60} in anti-cancer and anti-viral treatments (KHARISOV, 2009; LUCAFÒ, 2012; LUCAFÒ, 2013; MARINA A. ORLOVA, 2013; LUCAFÒ, 2014), as it would make possible the exploitation of poly(fullerene) nano- and meso-structures such as micelles and vesicles (J. HOLDER, 1998).

C_{60} is typically incorporated into polymers as a moiety pendent to the main-chain as it is relatively simple to control just one addition to the sphere (DREES, 2005; ADAMOPOULOS, 2006; BALL, 2006; GIACALONE, 2006; HEISER, 2006; SIVULA, 2006; BARRAU, 2008), but such polymers can result in excessive aggregation of C_{60}s (GHOLAMKHASS, 2010). Using C_{60} as a monomer may reduce the degrees of freedom of movement of C_{60}, making excessive aggregation in the solid state less likely. Incorporating C_{60} directly into the polymer main-chain, however, is generally not simple as there are 30 [6,6]-

double bonds. Prior methods have included using Diels-Alder chemistry (GÜGEL, 1996), methano-bridges (SHI, 1992) and tether-directed pre-modification of C_{60}(ITO, H., 2006), but these can give cross-linking, intractable products, or require multi-step preparative chemistry, respectively. An attempt to resolve this was made using atom transfer radical addition polymerisation (ATRAP) as the reaction is based on radical bis-additions around just one C_{60} 1,4-phenylic ring (RAMANITRA 2016) One down-side of this system though was the high amounts of CuBr required, leading to metal impurities of which even trace amounts can be detrimental to device performances (URIEN, 2007; NIKIFOROV, 2013). An alternative and recently discovered method, the so-called sterically controlled azomethine ylide cycloaddition polymerization (SACAP) of C_{60}, showed that it was possible to reach high molecular weight poly(fullerene)s with certain co-monomers under forced conditions (RAMANITRA 2016). This stimulated us to see if new metal-free polymerizations of fullerene could be developed with different routes.

Aziridinofullerenes, are useful synthetic intermediates for highly efficient and regioselective addition of spherical fullerene cages, as acid-induced 1,4-bisaddition of aromatic compounds, [2+2] cycloaddition with alkynes and isomerization to azafulleroids. The aziridino fullerenes have been widely prepared by 1,3 dipolar cycloaddition of azides to C_{60} followed by thermal or photochemical denitrogenation of the triazolinofullerene adducts (YANG, H.-T., 2014). The reaction results in two isomeric products such as [5,6]-open fulleroids and [6,6]-closed methanofullerenes (YANG, C., 2009a), all the isomeric procuts are presented in Figure 8. From an electronic-structure point of view, the [5,6]-open isomers are appealing since they conserve the 60 π electrons of the C_{60}.

Figure 8: Aziridinofullerenes isomeric products.

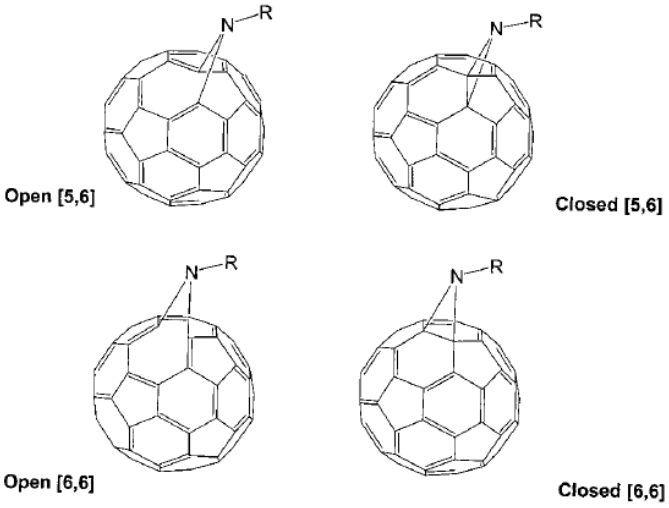

From: Cases et al. (CASES, 2000)

Prior work has demonstrated that imino-C_{60} mono-adducts can exhibit high charge mobilities (YANG, C., 2009a). We were therefore particularly interested to see if the bis-imino adduct chemistry (SCHICK, 1996) could be extended to prepare stable polymers with high electron mobilities, and to explore their applicability to organic photovoltaic devices (OPVs). We report for the first time the discovery that it is possible to deliver oligo- and poly(aziridinofullerene)s (PAFs). The macromolecular structures are prepared using 1,3-dipolar cyclo-additions of diazido comonomers to C_{60} under catalyst-free conditions and the methodology is such that metals are avoided in the final synthesis.

1.6 Hybrid particles

Hybrid nanocomposite materials combine the advantages of inorganic (stability, high electron mobility, nano-scale electrical and optical properties) and organic materials (easy processability, high coefficient absorption) (WRIGHT, 2012). Even though inorganic-organic systems have already been applied in (opto)electronics, including solar cells (GÜNES, 2007a),

light emitting diodes (YANG, Y., 2008) and sensors (LEVELL, 2010), the interface between conjugated polymers and nanocrystals is a challenge due to their different properties. The efficient energy transfer between organic and inorganic semiconductors is a widely sought property. However, issues in the interfacial charge separation and transport are not fully understood, there is a critical need for a deeper fundamental understanding of the influence of long-range ordering on collective phenomena such as exciton diffusion and recombination and carrier transport. It is commonly believed that a photogenerated exciton dissociates to generate a bound complex with charge transfer character at a donor/acceptor heterojunction and then separates into fully dissociated charge carriers (LIU, R., 2014). The interfacial charge separation is an important step in the photovoltaic processes of the hybrid materials. For improvement of devices performance and enhance properties of hybrid materials a strategy is to attach the components by covalent bonds (BOUSQUET, 2014). The combination between TiO_2 attached with π-conjugated semiconducting polymers serving as photoactive charge transport material have been study by others researchers (BEEK, W. J. E., 2002; BEEK, WALDO J. E., 2004; ODOI, 2006; ZHANG, Y., 2006; XU, 2012; BOON, 2014).

In those hybrid systems, there is the possibility of precisely synthesize inorganic nanocrystals and organic polymers with high degree of structural control, to optimize properties of the components, building functional materials. Passivation of nanocrystals surface with organic materials, such as polymers, is one strategy to prevent aggregation and enhance their dispersion in solutions. The most used surfactants with non-conjugated satured chains do not facilitate electron transfer between the materials (XU, 2012). In order to understand the key issues in association with photoinduced charge separation/transportation processes and to improve overall power conversion efficiency, various combinations with nanostructures of hybrid systems have been investigated. Typically, the domain sizes within either component of the heterojunction should be comparable to the diffusion length of an exciton in that material

(ARICI, 2003; BRISENO, 2010; BOON, 2012; ISHII, 2012; BABU, 2014; JAYARAMAN, 2014). For soluble media, the large interfacial area is achieved spontaneously by blending the acceptor and donor components together in a solution, which is then cast into thin films (BOUCLE, 2007).

Awada et al. have create a macromolecular self-assembled monolayer that could be applied to different metal oxide surfaces and represents a new one-pot strategy based on triethoxysilane coupling reaction (AWADA, 2014). Some other works grew the polymers directly into the oxides. Xu et al. have investigated the charge transfer between triethoxy-2-thienylsilane covalently link P3HT onto TiO_2 nanorods. They have found to have a more coil-like conformation in the chemically linked samples with more twisted defects that led to torsional relaxation with a larger amplitude and a longer decay time than those in pristine P3HT and physically mixed samples. Beek et al (BEEK, W. J. E., 2002) have studied grafted TiO_2@oligothiophene via a carboxylic acid functionalized group and the influence of alkyl linker length. They have found the rate of electron transfer decreasing as the alkyl spacer length increased. Later (BEEK, WALDO J. E., 2004), they have study heterosupramolecular assemblies of terthiophene moieties and TiO_2 nanoparticles, linked by alkyl spacers of different lengths in the rate of charge transfer monitoring the changes in the competing fluorescent decay. They also have found that longer spacers lower the charge transfer rate. Zhag et al.(ZHANG, Y., 2006) grew P3HT onto TiO_2 nanotubes via a covalent silane linker, which exhibited more efficient charge transfer from P3HT to TiO_2 than physisorbed P3HT. However, the alkyl group used in the linker might cause electron transfer to take place in a weakly-coupled nonadiabatic regime.

In this study, we have synthesized grafted nanoparticles, TiO_2@P3HT and Nb_2O_5@P3HT using triethoxysilane-terminated P3HT and homemade TiO_2 and Nb_2O_5 nanoparticles. The energy migration in P3HT and charge transfer from P3HT to the oxides were

studied by comparison with the polymer and physically mixed P3HT/oxides. The charge transfer was found to occur evidenced by photoluminescence (PL) quenching and a decay of the life time constant of the grafted samples, differing from the polymer.

CHAPTER 2

METHODOLOGY AND CHARACTERIZATION TECHNIQUES

2.1 Methodology

2.1.1 Polyfullerenes

Chemicals and reagents were used as received from Aldrich unless otherwise indicated and stored in the glove box when required. Solvents were dried from over their respective drying agents under dry nitrogen.

All reactions were performed under pre-dried nitrogen and in flame-dried glassware. All polymerizations were performed under stringently controlled anaerobic conditions using typical Schlenk line techniques. Solvents, such as 1,2-dichlorobenzene and toluene, were repeatedly degassed under reduced pressures and flushed with dry nitrogen prior to use. Chemicals were similarly placed under reduced pressure and covered with nitrogen. Syringes used to transfer reagents or solvents were nitrogen purged.

Comonomers Synthesis (All the NMR spectra are presented in a special Section in the end of Chapter 3)

*Synthesis of 1,4-bis(octyloxy)benzene **(2)***

Scheme 1: Synthesis of 1,4-bis(octyloxy)benzene (**2**) from hydroquinone (**1**).

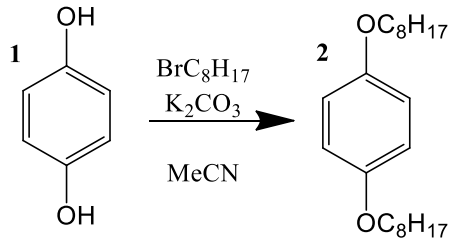

Hydroquinone (10.0 g, 0.09 mol) and K_2CO_3 (37.6 g, 0.27 mol) were stirred with acetonitrile (100 mL) for 30 min at room temperature under nitrogen. 1-Bromooctane (12 mL,

0.07 mol) was added dropwise and the reaction heated at reflux for 48 h. On cooling to room temperature, the solution was dropped into iced water (500 mL) and the product recovered by filtration. Purification was performed by twice dissolving the product in chloroform and precipitating it from methanol to yield white crystals (16.6 g, 54 %).

^{1}H NMR (400.6 MHz, $CDCl_3$) δ = 0.91 (t, *J* = 6.0 Hz, 6H, -$OCH_2(CH_2)_6CH_3$), 1.32-1.85 (m, 24H, -$OCH_2(CH_2)_6CH_3$), 3.95 (t, *J* = 6.0 Hz, 4H, -$OCH_2(CH_2)_6CH_3$), 6.87 (s, 4H, aromatics) ppm.

Synthesis of 1,4-bis(dodecyloxy)benzene ***(3)***

Scheme 2: Synthesis of 1,4-bis(dodecyloxy)benzene (**3**) from hydroquinone (**1**).

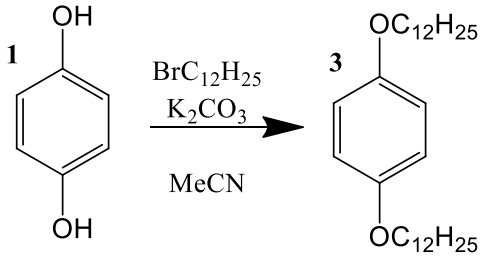

Hydroquinone (5.0 g, 0.045 mol) and K_2CO_3 (18.82 g, 0.14 mol) were stirred with acetonitrile (100 mL) for 30 min at room temperature under nitrogen. 1-Bromododecane (32.7 mL, 0.014 mol) was added dropwise and the reaction heated at reflux for 48 h. Once cooled to room temperature, the solution was dropped into iced water (500 mL) and the product recovered by filtration. Purification was performed by twice dissolving the product into chloroform and precipitating it from methanol to yield a white crystalline material (6.7 g, 44 %).

^{1}H NMR (400 MHz, room temperature, $CDCl_3$) δ = 0.91 (t, *J* = 6.0 Hz, 6H, -CH_3), 1.51–1.22 (m, 36H, -CH_2-), 1.78 (t, *J* = 8.0 Hz, 4H, -CH_2-), 1.88 (t, *J* = 6.0 Hz, 4H, -CH_2-), 3.92 (t, *J* = 6.0 Hz, 4H, -O-CH_2), δ 6.84 (s, 4H, *-aromatic*) ppm.

*Synthesis of 1,4-bis(hexadecyloxy)benzene **(4)***

Scheme 3: Synthesis of 1,4-bis(hexadecyloxy)benzene (**4**) from hydroquinone (**1**).

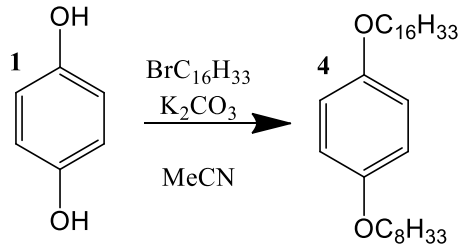

Hydroquinone (5.0 g, 0.045 mol) and K_2CO_3 (18.82 g, 0.14 mol) were stirred with acetonitrile (100 mL) for 30 min at room temperature under nitrogen. 1-Bromohexadecyldecane (41.6 mL, 0.14 mol) was added dropwise and the reaction warmed to reflux for 48 h. Once cooled to room temperature, the solution was dropped into iced water (500 mL), and the product recovered by filtration. Purification was performed by twice dissolving the product into chloroform and precipitating it from methanol to yield a white crystalline material (7.8 g, 31 %).

^{1}H NMR (400 MHz, room temperature, $CDCl_3$): δ 0.91 (t, *J* = 6 Hz, 6H, -CH_3), 1.51–1.22 (m, 56H, -CH_2-), 1.78 (q, *J* = 6,0 Hz, 4H, -CH_2-), 1.87 (q, *J* = 6 Hz, 4H, -CH_2-), 3.93 (t, *J* = 6,0 Hz, 4H, -O-CH_2), 6.84 (s, 4H, -aromatic).

*Synthesis of 1,4-bis(bromomethyl)-2,5-bis(octyloxy)benzene **(5)***

Scheme 4: Synthesis of 1,4-bis(bromomethyl)-2,5-bis(octyloxy)benzene (**5**).

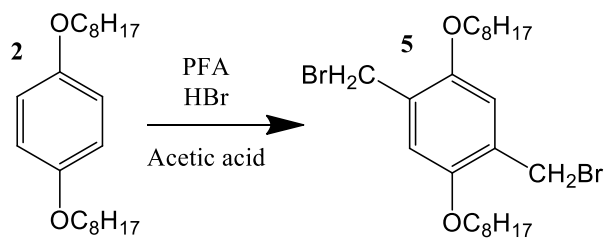

1,4-Bis(octyloxy)benzene (5.0 g, 0.015 mol) and the paraformaldehyde (1.12 g, 0.04 mol) were stirred with acetic acid (150 mL) under nitrogen. HBr 31 % in acetic acid (8.3 mL, 0.05 mol) was added dropwise and the reaction warmed to 70 °C for 2 h. Once cooled to room temperature, the solution was quenched with 300 mL of water and the product recovered by filtration. Purification was performed by twice dissolving the product into chloroform and precipitating it from methanol to yield a brownish material (3.78 g, 48 %).

^{1}H NMR (400.6 MHz, $CDCl_3$) δ = 0.91 (t, 6H -$OCH_2(CH_2)_6CH_3$), 1.32-1.85 (m, 24H, -$OCH_2(CH_2)_6CH_3$), 4.01 (t, *J* = 4.0, 4H, -$OCH_2(CH_2)_6CH_3$), 4.55 (s, 4H, -CH_2Br), 6.87 (s, 4H, aromatics) ppm.

Synthesis of 1,4-bis(bromomethyl)-2,5-bis(dodecyloxy)benzene ***(6)***

Scheme 5: Synthesis of 1,4-bis(bromomethyl)-2,5-bis(dodecyloxy)benzene (**6**).

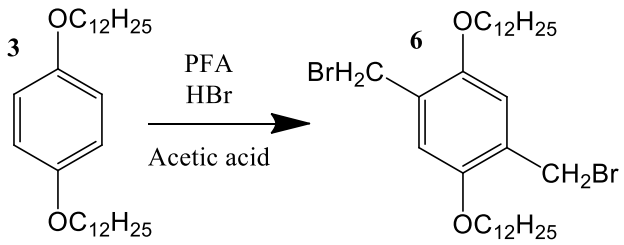

1,4-bis(dodecyloxy)benzene (5.0 g, 0.011 mol) and the paraformaldehyde (0.84 g, 0.028 mol) were stirred with acetic acid (150 mL) under nitrogen. HBr 31 % in acetic acid (6.8 mL, 0.036 mol) was added dropwise and the reaction warmed to 70 °C for 2 h. Once cooled to room temperature, the solution was quenched with 300 mL of water and the product recovered by filtration. Purification was performed by twice dissolving the product into chloroform and precipitating it from methanol of yield a brownish material (4.5 g, 64 %).

^{1}H NMR (400.6 MHz, $CDCl_3$) δ = 0.91 (t, *J* = 6.0, 6H -$OCH_2(CH_2)_{10}CH_3$), 1.20-1.55 (m, 36H, -$OCH_2(CH_2)_{10}CH_3$), 1.83 (m, 4H, -CH_2-), 4.00 (t, *J* = 6 Hz, 4H, -$OCH_2(CH_2)_{10}CH_3$), 4.56 (s, 4H, -CH_2Br), 6.87 (s, 2H, aromatics) ppm.

*Synthesis of 1,4-bis(bromomethyl)-2,5-bis(hexadecyloxy)benzene **(7)***

Scheme 6: Synthesis of 1,4-bis(bromomethyl)-2,5-bis(hexadecyloxy)benzene (**7**).

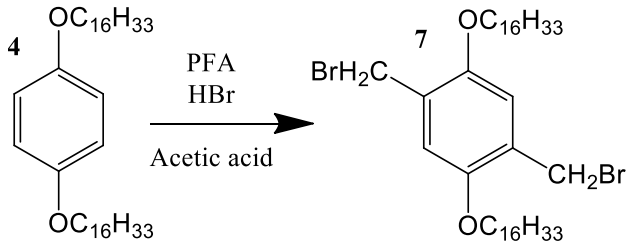

1,4-bis(hexadecyloxy)benzene (5.0 g, 0.009 mol) and the paraformaldehyde (0.67 g, 0.02 mol) were stirred with acetic acid (150 mL) under nitrogen. HBr 31 % in acetic acid (5.7 mL, 0.03 mol) was added dropwise and the reaction warmed to 70 °C for 2 h. Once cooled to room temperature, the solution was quenched with 300 mL of water and the product recovered by filtration. Purification was performed by twice dissolving the product into chloroform and precipitating it from methanol to yield a brownish material (3.2 g, 48 %).

^{1}H NMR (400 MHz, room temperature, $CDCl_3$): δ 0.91 (t, *J* = 6 Hz, 6H, -CH_3), 1.51–1.22 (m, 56H, -CH_2-), 1.78 (q, *J* = 6 Hz, 4H, -CH_2-), 1.87 (q, *J* = 6 Hz, 4H, -CH_2-), 3.93 (t, *J* = 6 Hz, 4H, -O-CH_2), 4.56 (s, 4H, -CH_2¬Br), 6.84 (s, 2H, -aromatic).

*Synthesis of 1,4-bis(azidomethyl)-2,5-bis(octyloxy)benzene **(8)***

Scheme 7: Synthesis of 1,4-bis(azidomethyl)-2,5-bis(octyloxy)benzene (**8**).

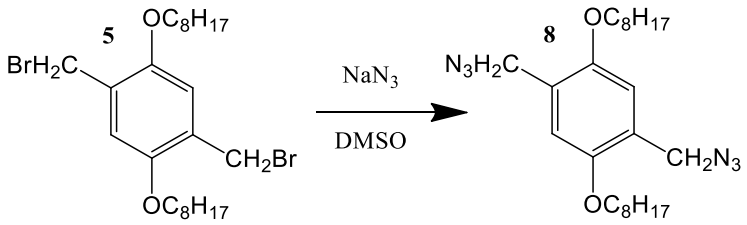

1,4-bis(bromomethyl)-2,5-bis(octyloxy)benzene (3 g, 5.76 x 10^{-3} mol) and sodium azide (1.11 g, 0.017 mol) were stirred with dimethyl sulfoxide (40 mL) under nitrogen for 12 h. The solution was dropped into iced water (150 mL), and the product recovered with diethyl ether (100 mL). Purification was performed by twice washing the solution with brine and recovering with diethyl ether. Drying over $MgSO_4$, roto-evaporation of the solvent, filtration and drying under air yielded white crystals (1.72 g, 67 %).

^{1}H NMR (400.6 MHz, $CDCl_3$) δ = 0.91 (t, *J* = 6.0, 6H -$OCH_2(CH_2)_6CH_3$), 1.32-1.85 (m, 24H, -$OCH_2(CH_2)_6CH_3$), 4.01 (t, 4H, -$OCH_2(CH_2)_6CH_3$), 4.45 (s, 4H, -CH_2N_3), 6.87 (s, 4H, aromatics) ppm.

^{13}C NMR (100.16 MHz, $CDCl_3$) δ = 14.34 (s, O-$CH_2(CH_2)_6CH_3$), 22.70 (s, O-$CH_2(CH_2)_5CH_2CH_3$), 26.08 (s, O-$CH_2CH_2CH_2(CH_2)_4CH_3$), 29.23 - 29.33 (m, O-$CH_2(CH_2)_6CH_3$), 31.74 (s, O-$CH_2(CH_2)_4CH_2CH_2CH_3$), 49.81 (-CH_2-N_3), 68.93 (s, O-$CH_2(CH_2)_6CH_3$), 113.74 (s, aromatic), 124.88 (s, *aromatic*-CH_2N_3), 150.56 (s, *aromatic*-OC_8H_{17}) ppm.

*Synthesis of 1,4-bis(azidomethyl)-2,5-bis(dodecyloxy)benzene **(9)***

Scheme 8: Synthesis of 1,4-bis(azidomethyl)-2,5-bis(dodecyloxy)benzene (**9**).

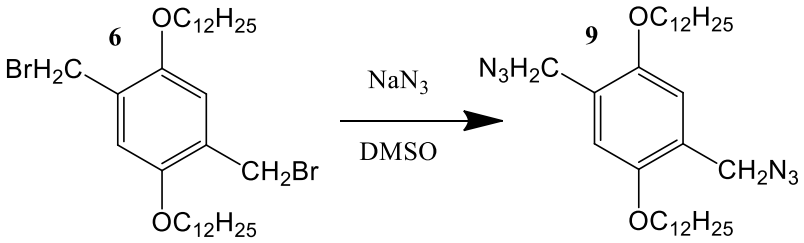

1,4-Bis(bromomethyl)-2,5-bis(dodecyloxy)benzene (3 g, 4.74 x 10^{-3} mol) and sodium azide (0.31 g, 0.014 mol) were stirred with dimethyl sulfoxide (40 mL) under nitrogen for 12 h. The solution was dropped into iced water (150 mL), and the product recovered with diethyl ether. Purification was performed by twice dissolving the product in brine and recovering with diethyl ether and dried over $MgSO_4$ to a yield a white material (2.3 g, 68 %).

^{1}H NMR (400 MHz, $CDCl_3$) δ 0.91 (t, *J* = 6 Hz, 6H, -C*H*$_3$), 1.63 (m, 40H, -C*H*$_2$-),1.82 (t, *J* = 6 Hz, 4H, -C*H*$_2$-), 4.39 (s, 4H, -C*H*$_2$-N_3), 6.85 (s, 2H, -*aromatic*).

^{13}C NMR (100.16 MHz, $CDCl_3$) δ = 14.11 (s, O-$CH_2(CH_2)_{10}$*C*H_3, 22.69 (s, O-$CH_2(CH_2)_9$*C*H_2CH_3), 26.08 (s, O-CH_2*C*H_2*C*$H_2(CH_2)_8CH_3$), 29.38 (s, O-CH_2*C*H_2*C*H_2*C*$H_2(CH_2)_7CH_3$), 49.95 (s, -*C*H_2-N_3), 68.91 (s, O-CH_2*C*H_2*C*H_2*C*H_2*C*$H_2(CH_2)_6CH_3$), 76.70 - 77.34 (m, O-*C*$H_2(CH_2)_{10}CH_3$), 113.46 (s, aromatic), 124.18 (s, *aromatic*-CH_2N_3), 150.64 (s, *aromatic*-$OC_{12}H_{25}$) ppm.

*Synthesis of 1,4-bis(azidomethyl)-2,5-bis(hexadecyloxy)benzene **(10)***

Scheme 9: Synthesis of 1,4-bis(azidomethyl)-2,5-bis(hexadecyloxy)benzene (**9**).

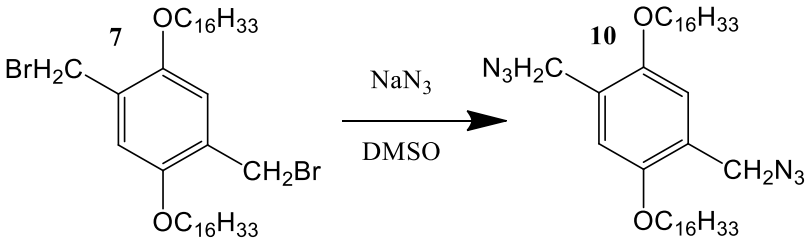

1,4-Bis(bromomethyl)-2,5-bis(hexadecyloxy)benzene (3 g, 4.03 x 10^{-3} mol) and sodium azide (0.78 g, 0.012 mol) were stirred with dimethyl sulfoxide (120 mL) under nitrogen for 12 h. The solution was dropped into iced water (150 mL), and the product recovered with diethyl ether (100 mL). Purification was performed by twice washing the product with brine, recovering with diethyl ether, drying over MgSO4 and then evaporation of the solvents under air. The yield of a creamy-white powder (1.4 g, 52 %).

^{1}H NMR (400 MHz, $CDCl_3$) δ 0.91 (t, *J* = 6 Hz, 6H, -C*H*$_3$), 1.30 (m, 56H, -C*H*$_2$-), 1.82 (t, *J* = 6 Hz, 4H, -C*H*$_2$-), 4.00 (s, 4H, -C*H*$_2$-N$_3$), 4.55 (s, 2H, -*aromatic*).

Poly(aziridinofullerene) synthesis

In this synthesis a novel route for polymerization has been stablished, based os the mechanism of the cycloaddition of azidoalkyls to C_{60}, which is well understood (CASES, 2000).

Figure 9: Poly(aziridinofullerene) synthesis.

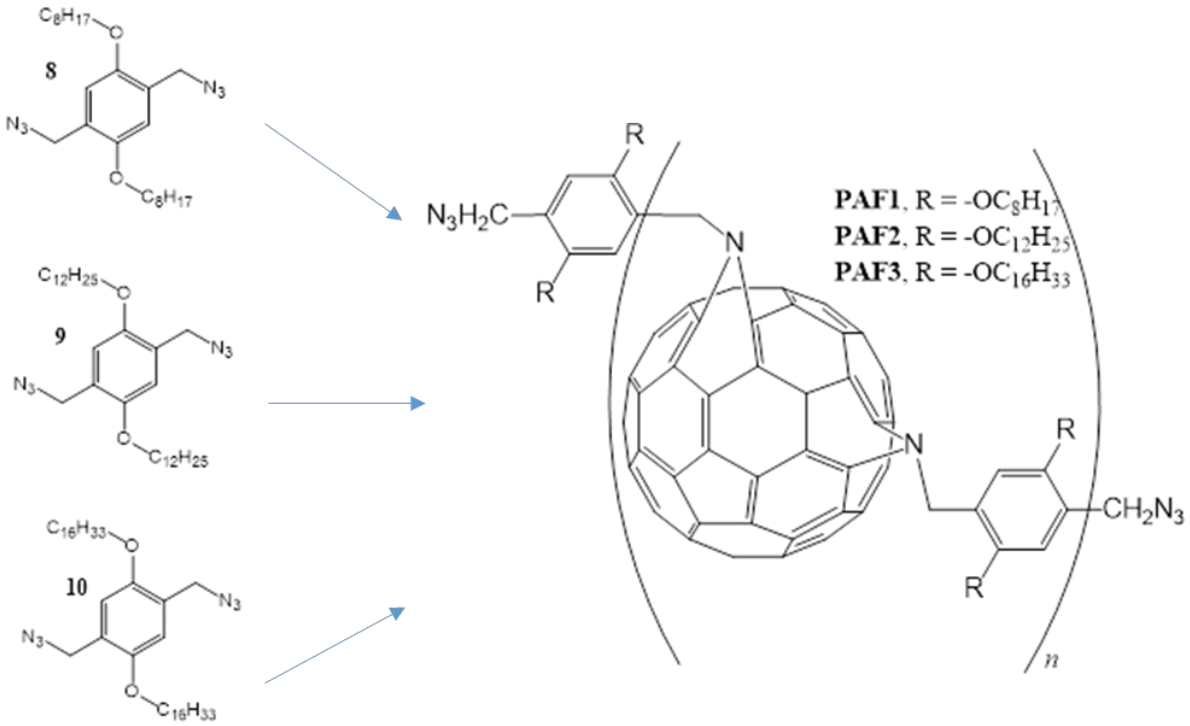

Synthesis of PAF1

Thoroughly nitrogen flushed 1,2-dichlorobenzene (1,2-DCB, 80 mL) and C_{60} (1.0 g, 1.38 x 10^{-3} mol) were stirred under dry N_2 for 30 min at room temperature prior to the addition of the comonomer **8**, 1,4-bis(azidomethyl)-2,5-bis(octyloxy)benzene (0.613 g, 1.38 x 10^{-3} mol), and a subsequent heating at 60 ˚C for 24 h. The solution was stirred for a further 2 h at 100 ˚C. The product was recovered by precipitation in methanol (500 mL), using toluene (5 mL) to add transfer. Soxhlet cycled washing over periods of 12 h and 3 days with, respectively, methanol and hexane, followed by drying under reduced pressure at 100 ˚C resulted in 0.92 g (yield, 56 %) of a black powder.

^{1}H NMR (400.6 MHz, C_6D_6) δ = 6.95 (broad, -*aromatic*), 6.3 (d, *J* = 220 Hz, -C*H*$_2$-N=), 5.3 (broad, -C*H*$_2$-N$_3$), 4.2 (broad, -OCH$_2$-), 2.8, 1.6 and 1.3 (broad peaks, -C*H*$_2$-), 0.93 (broad, -C*H*$_3$).

Synthesis of PAF2

Degassed 1,2-dichlorobenzene (1,2-DCB, 80 mL) and C_{60} (1.38 x 10^{-3} mol, 1 g) were stirred under dry N_2 for 30 min at room temperature prior to the addition of the comonomer **9**, 1,4-bis(azidomethyl)-2,5-bis(dodecyloxy)benzene (1.38 x 10^{-3} mol, 0.768 g), and a subsequent heating to 60 ˚C for 24 h. The solution was stirred for 2 h at 100 ˚C. Toluene (5 mL) was added, and the product recovered from precipitation in methanol. Soxhlet cycled washing over periods of 12 h and 3 days with, respectively, methanol and hexane, followed by drying under reduced pressure at 100 ˚C resulted in 1.24 g (yield, 68 %) of a brownish powder.

^{1}H NMR (400.6 MHz, C_6D_6) δ = 6.95 (broad, -*aromatic*), 6.3 (d, *J* = 220 Hz, -C*H*$_2$-N=), 5.3 (broad, -C*H*$_2$-N_3), 4.2 (broad, -OCH_2-), 2.8, 1.6 and 1.3 (broad peaks, -C*H*$_2$-), 0.93 (broad, -C*H*$_3$).

Synthesis of PAF3

Degassed o-DCB (80 mL) and C_{60} (1.38 x 10^{-3} mol, 1 g) were stirred under dry N_2 for 30 min at room temperature prior to the addition of the comonomer **10**, 1,4-bis(azidomethyl)-2,5-bis(hexadecyloxy)benzene (1.38 x 10^{-3} mol, 0.929 g), and a subsequent heating to 60 ˚C for 24 h. The solution was stirred for 2 h at 100 ˚C. Toluene (5 mL) was added, and the product recovered from precipitation in methanol. Soxhlet cycled washing over periods of 12 h and 3 days with, respectively, methanol and hexane, followed by drying under reduced pressure at 100 ˚C resulted in 1.22 g (yield, 63 %) of a brownish powder. Soxhlet cycled washing over periods of 12 h and 3 days with, respectively, methanol and hexane, followed by drying under reduced pressure at 100 ˚C resulted in 1.24 g (yield, 68 %) of a brownish powder.

^{1}H NMR (400.6 MHz, C_6D_6) δ = 6.95 (broad, -*aromatic*), 6.3 (d, *J* = 116 Hz, -C*H*$_2$-N=), 5.8 (broad, -C*H*$_2$-N_3), 4.1 (broad, -OCH_2-), 2.9, 2.7 and 2.3 (broad peaks, -C*H*$_2$-), 0.89 (broad, -C*H*$_3$).

Device Fabrication (Made by Christine Luscombe's group UW – USA).

Bulk heterojunction organic solar cells were fabricated using glass coated with ITO as transparent substrate. The substrates were cleaned by consecutive sonication in detergent, acetone and isopropyl alcohol in an ultrasonic bath (VWR Model 50T), followed by UV-ozone cleaning (PDC 32G) for 10 min in order to prepare the surface for PEDOT:PSS deposition. PEDOT:PSS (poly(3,4-ethylenedioxythiophene) polystyrene sulfonate - Heraeus Clevios P VP Al4083, 40 nm thickness) was spin-coated onto the clean substrate surface, followed by 10 min of annealing in air at 140 ºC to remove remaining water. The samples were cooled to room temperature and transferred into a N_2-filled glovebox. P3HT (Rieke 4002-E)/PCBM (American Dye Source), P3HT/PAF1 or P3HT/PAF2 (1:0.6 wt%/wt%) solutions in anhydrous chorobenzene (CB) (40 mg/mL) were prepared, heated at 60 ºC and stirred overnight inside the glove box. Prior to deposition, the solutions were filtered through a 0.2 μm filter. The photovoltaic active materials were then spin-coated on top of the PEDOT:PSS layer to produce an active layer of 100 nm, followed by annealing at 130 ºC for 10 min. The aluminium cathode (100 nm thick) was thermally evaporated through a shadow mask under high vacuum about 4.0×10^{-7} torr. Solar characterization of the devices was done in N_2 ambient, using a Keithley 2400 source meter unit and an Oriel Xenon Lamp (450 W) coupled with an AM1.5 filter (*Air Mass* 1.5, 1.5 atmosphere thickness, corresponds to a solar zenith angle of z=48.2°) as a light source and a light intensity of 100 $mWcm^{-2}$ was used in all the measurements. Devices parameters were tested for at least 16 devices for each sample.

2.1.2 Inorganic oxide

Titanium tetraisopropoxide (TTIP) (Alfa-Aesar 97%), HNO_3 (Dinâmica) and NaOH (Synth) were used as received. For the acidic synthesis, 12 mL (0.4 mol) of TTIP was added

dropwise in 100 mL of water with 0.5 mL of HNO_3, 0.01 M (DAR 2014). For the alkalyne synthesis, 12 mL (0.4 mol) of TTIP was added dropwise in NaOH solutions with different concentrations: 0.1, 1 and 10 M. In both cases, the precursor solution was stirred for 6 h at 80 °C. The solution was placed into a Teflon autoclave for the microwave treatment. A modified domestic microwave (Panasonic Piccolo 800 W) coupled with an external temperature controller (Incon CNT120) was used. The synthesis temperature varied from 110 to 150 °C and time from 2 to 60 min. After the microwave treatment, the colloidal solution was washed with water. The solutions were centrifuged at 2500 rpm for 5 min and dried in an oven at 60 °C. The samples were named as follow: a prefix HM (for the acidic media) or HMB (for the alkaline media), followed by the temperature and time of treatment. The concentration of NaOH is presented after the time. The sample HM150-30-10 was washed with HCl 0.1 M in order to remove the excessive Na^+ ions (KASUGA, 1998). Details about the synthesis parameters used are presented in the Table 7.

2.1.3 Hybrid nanoparticles

Grafting triethoxysilane-terminated P3HT onto oxide nanoparticles

The anatase TiO_2 nanoparticles used was HM150-30. The Nb_2O_5 nanoparticles were synthesized by microwave assisted hydrothermal technique. It was used niobium (V) oxide as precursor in acidic media at 150 ºC in 60 min. Functionalized P3HT with the triethoxysilane group was synthesized as previously described by Awada *et al.* (AWADA, 2014) and presented at Scheme 10. For the graft reaction, the nanoparticles where separately dispersed in THF (2 mg/mL) by ultrassonication during 1 h. The solution of triethoxysilane-P3HT (20 mg/mL) in THF was added to the mixture.

Scheme 10: Synthesis of functionalized P3HT and graft reaction.

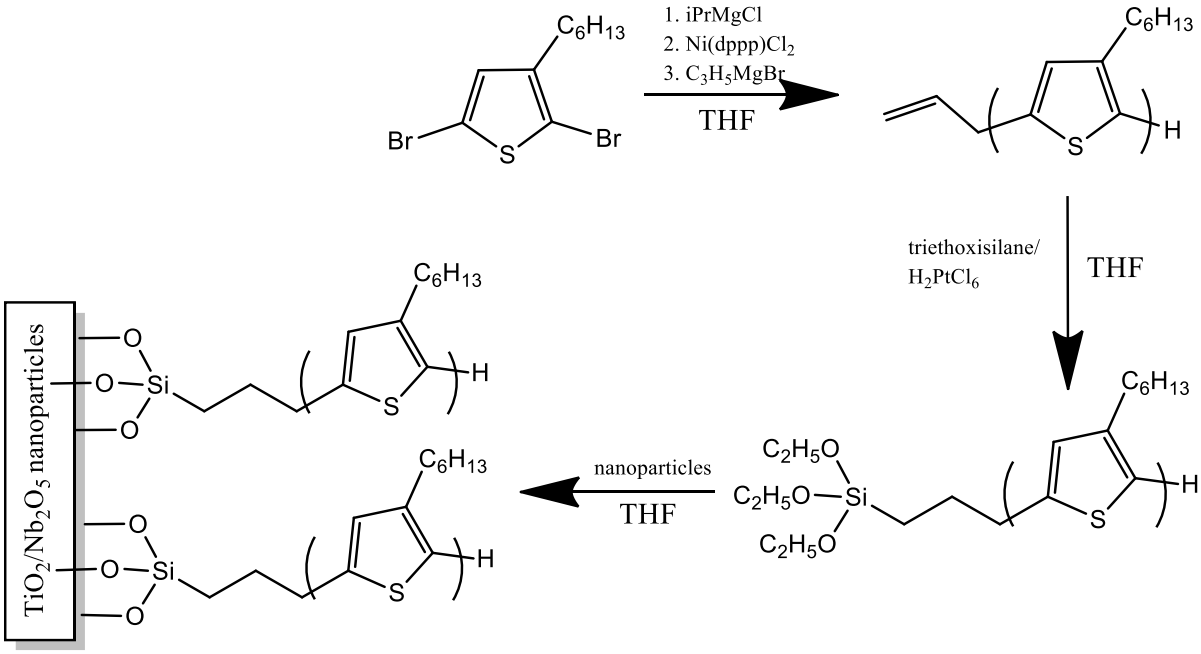

From: Adapted from Awada *et al.* (AWADA, 2014)

The unreacted chains were removed at the end of the reaction by solubilization and washing. The reaction was then preceded at 60 °C for 12 h under inert atmosphere. The medium was cooled to room temperature and the grafted nanoparticles were purified by centrifugation (10.000 rpm, 10 min) with removal of the supernatant containing excess of organic component. The precipitated particles were collected, dried, and stored under nitrogen. A change in the color of the nanoparticles was clearly observable from white to violet after grafting (anchoring the polymer on the oxide) for the TiO_2 and from white to orange to Nb_2O_5 (solid state) probably due its different surface area.

2.2 Characterization Techniques

2.2.1 X ray diffratometry (XRD)

X rays are electromagnetic radiations that have higher energies and shorter wavelengths. When a beam of X-ray focuses on a solid material, a fraction of this beam is scattered in various directions by electrons associated with each atom or ion (CALLISTER, 1994). Considering two parallel planes of atoms which have the same Miller index *h*, *k* and *l* which are separated by a d_{hkl} interplanar spacing and assuming a beam of X-rays parallel monochromatic and coherent (in phase), with wavelength λ focusing on these two planes, according to an angle θ, the condition for diffraction is defined by Equation (1), known as the Bragg's Law, where *n* represents the order of the reflection, which can be any integer number (1,2,3,...).

$$n\,\lambda = 2\,d_{hkl}\sin\theta \qquad \text{Equation (1)}$$

The average crystal (grain) size (D) is calculated using the Scherrer equation, Equation (2) (PATTERSON, 1939):

$$D = \frac{0{,}9\,\lambda}{\beta\cos\theta} \qquad \text{Equation (2)}$$

Where 0.9 is a dimensionless shape factor, λ is the irradiation wavelength (0.154 nm for CuKα), β is the full width at half maximum (FWHM) - the width of a spectrum curve measured between those points on the y-axis which are half the maximum amplitude - and θ is the Bragg angle.

The formation of crystalline phases, depending on the variation of the parameters studied was accompanied by X-ray diffraction using a Rigaku X-ray diffractometer, model

RINT2000 at Unesp/Bauru. The experimental conditions were from 20° to 80° with an increase $\Delta 2\theta = 0.02°$ and scan speed of 2°/min, Cukα radiation, 40 kV, 20 mA.

2.2.2 Scanning electron microscopy (SEM)

Electronic microscopic is an extremely useful tool in the study and characterization of materials. It allows to correlate microstructure with different characteristics and properties (CALLISTER, 1994). The scanning electron microscopy is a technique in which the surface of a sample to be examined is traced with a collimated beam of electrons. The reflected electron beam (or backscattering) is collected and then displayed on a cathode ray tube. The image that appears on the screen, which can be photographed, is the sample surface characteristics. The surface may or may not be polished, but it must necessarily be electrically conductive; an extremely thin metal coating can be applied on the surface of non-conductive materials, such as polymers. It is possible to have magnifications ranging from 10 to over 80,000 times under SEM. The use of the SEM with FEG (field emission gun) provides magnifications ranging from 10 to more than 300,000 times (CALLISTER, 1994).

Samples for SEM were prepared from the dispersion of the powder in acetone for 15 minutes. Then, the solution was dropped on a silicon substrate previously cleaned and dried, adhered to the sample holder with carbon tape (3M). The contacts were made with silver paste, and cured at 120 °C for 10 minutes in order to reach maximum conductivity.

The microscopy images were made at the Interdisciplinary Laboratory of Electrochemistry and Ceramics (LIEC) – Chemistry Department at UFSCar with a FEI Inspect F50 equipment and Structural Characterization Laboratory (LCE) of the Department of Materials Engineering (DEMa) of the Federal University of São Carlos - UFSCar with equipment Philips XL30-FEG.

2.2.3 Energy Dispersive X-ray Spectroscopy (EDX)

Energy Dispersive X-ray Spectroscopy (EDS or EDX) is a chemical microanalysis technique used in conjunction with scanning electron microscopy (SEM). This technique detects X-rays emitted from the sample during bombardment by an electron beam to characterize the elemental composition of the analyzed volume. All elements from atomic number 4 (Be) to 92 (U) can be detected in principle. The X-ray energy is characteristic of the element from which it was emitted. Features or structural phases of the nanoparticles as small as 1 μm or less can be analyzed (UTSUNOMIYA, 2003).

2.2.4 Transmission electron microscopy (TEM)

The transmission electron microscope comprises an electron beam and a set of electromagnetic lenses that control the beam enclosed in an evacuated column at a pressure of about 10^{-5} mmHg. It has six magnetic lenses, and various electromagnetic coils deflection and openings located along the path of the electron beam (PADILHA, 2012). Among these components, we highlight the following three for their importance with respect to the phenomena of electron diffraction: objective lens, lens aperture and selective opening of diffraction. The function of projectors lenses is to produce a parallel incident beam of sufficient intensity on the sample surface. The electrons leave the sample through the lower surface with a distribution of intensity and direction controlled mainly by diffraction pattern imposed by the crystalline arrangement of the atoms in the sample. Then, the objective lens is responsible for forming the image of the angular distribution of the diffracted electron beams. After this process, the remaining lenses will be used to increase the image or diffraction diagram for

observing the screen. The equipment using 200 kV accelerating voltage is the ideal for the study of materials (metal, ceramic and polymer) (PADILHA, 2012).

The oxide powder was suspended in isopropyl alcohol (Synth P.A.) and allowed to ultrasound for 15 minutes. Then, a copper with carbon film grid (TedPella) was duly immersed in the solution with the sample. The morphology and particle size of nanostructured TiO_2 was evaluated by a TEM (Philips CM120) operating at 200 kV at UNESP – Araraquara and as part of the training performed at DEMa UFSCar.

2.2.5 N_2 adsorption at 77 K – Brunauer Emmett Teller (BET)

The adsorbates retention capacity is commonly measured by adsorption isotherms. The shape of the isotherm is first tool in the analysis of adsorption nature. An adsorption isotherm is a series of measurements of the adsorbed amount depending on the gas equilibrium pressure at constant temperature (FERNANDES, 2008). The isotherm shape is the type of solid porosity. There are several known isotherms, but there are five main changes that have been suggested by Brunauer in 1938.

The analysis of the surface area (S_{BET}) was made by nitrogen adsorption at 77 K in a Micromeritics equipment, ASAP 2010 model, with collaboration of Prof. Margarida Juri Saeki, IBB-UNESP Botucatu. The samples were annealed at 100 °C under vacuum before being exposed to adsorption process. The treatment at 100 °C was done until the vacuum level in the sample compartment reach 4 - 5 μmHg and that the variation is less than 1 μmHg in a minute. The calculation of the surface area was made using the adsorption isotherm data.

2.2.6 Size-exclusion chromatography (SEC)

Size-exclusion chromatography (SEC) is a chromatographic method in which molecules in solution are separated by their size, and in some cases, molecular weight. It is usually applied to large molecules or macromolecular complexes such as proteins and industrial polymers. Typically, when an aqueous solution is used to transport the sample through the column, the technique is known as gel-filtration chromatography, versus the name gel permeation chromatography, which is used when an organic solvent, such as THF, is used as a mobile phase. SEC is a widely used polymer characterization method because of its ability to provide good molar mass distribution (Mw) results for polymers (PAUL-DAUPHIN, 2007).

SEC was done at EPCP – UPPA/France in a Viscoteck equipment coupled with digital refractometer (Viscotek), UV-Visible spectrophotometer (Viscotek) and multi-angle light scattering (Wyatt) using THF as solvent.

2.2.7 Nuclear magnetic resonance spectroscopy (NMR)

Nuclear magnetic resonance spectroscopy, NMR spectroscopy, is a research technique that exploits the magnetic properties of certain atomic nuclei. Frequently used in organic molecules, it is applicable to any kind of sample that contains nuclei possessing spin. It relies on the phenomenon of nuclear magnetic resonance and can provide detailed information about the structure, dynamics, reaction state, and chemical environment of molecules. The intramolecular magnetic field around an atom in a molecule changes the resonance frequency, thus giving access to details of the electronic structure of a molecule. NMR spectra are unique, well-resolved, analytically tractable and often highly predictable for small molecules (RABI, 1938).

^{1}H and ^{13}C NMR spectra of nuclear magnetic resonance (NMR) spectra were obtained at EPCP – UPPA/France using a Bruker 400 MHz machine in $CDCl_3$, 1,2-dichlorobenzene-d_4 and C_6D_6 for monomers and for polymers at room temperature unless specified.

2.2.8 Fourier Transformed-Infrared Spectroscopy (FTIR)

Fourier Transform-Infrared Spectroscopy (FTIR) is an analytical technique used to identify organic and inorganic materials. This technique measures the absorption of infrared radiation by the sample material versus wavelength. The infrared absorption bands identify molecular components and structures. The FTIR spectrometer uses an interferometer to modulate the wavelength from a broadband infrared source. A detector measures the intensity of transmitted or reflected light as a function of its wavelength. The signal obtained from the detector is an interferogram, which must be analyzed with a computer using Fourier transforms to obtain a single-beam infrared spectrum (MATERIALS EVALUATION AND ENGINEERING, 2016).

The infrared spectra (FTIR) were performed at UPPA – France on a Bruker FT ALPHA-T equipment. Samples were prepared by pressing 200 mg KBr pellets containing 3 mg of the material to be analyzed.

2.2.9 Thermogravimetry (TG)

In this technique, the weight losses of a substance is measured as a function of temperature, as the same is subjected to a controlled temperature program. Thus, registers a weight loss curve in function of temperature, known as thermogravimetric curve where T_i is the initial temperature, i.e. the temperature at which the weight change reaches a magnitude

such that the thermobalance can be sufficiently sensitive to detect, and T_f the final temperature, i.e. the temperature at which the mass loss reaches its maximum value at the end of the reaction. This instrument allows for the continuous weighting of a sample as a function of temperature as it is heated or cooled. The TG curves allow drawing conclusions on the thermal stability of the sample for composition and stability of intermediates and the waste composition, among others. Thermogravimetry is an effective method to quantify the loss of mass in materials. (WENDLANT, 1974). The glass transition, T*g*, is the reversible transition in amorphous materials (or in amorphous regions within semicrystalline materials) from a hard and relatively brittle "glassy" state into a viscous or rubbery state as the temperature is increased.

The thermal analysis was carried out at EPCP – UPPA/France in a Netzsch equipment – Model STA 409C, using synthetic air atmosphere and temperature range 30 to 700 °C.

2.2.10 Differential scanning calorimetry (DSC)

Differential scanning calorimetry or DSC is a thermoanalytical technique in which the difference in the amount of heat required to increase the temperature of a sample and reference is measured as a function of temperature. Both the sample and reference are maintained at nearly the same temperature throughout the experiment. Generally, the temperature program for a DSC analysis is designed such that the sample holder temperature increases linearly as a function of time. The reference sample should have a well-defined heat capacity over the range of temperatures to be scanned. By observing the difference in heat flow between the sample and reference, DSC are able to measure the amount of heat absorbed or released during a physical transformation, such as phase transition and glass transition (FRANK K. KO, 2014).

Differential scanning calorimetry was performed at EPCP – UPPA/France on a Perkin Elmer DSC8000 with solid samples in aluminium crucibles at a heating/cooling rate of 10 °C min^{-1} under a flux of N_2 maintained at 20 mL min^{-1}. Data treatment was performed with a Pyris™ series DSC8000 software.

2.2.11 UV-Vis spectroscopy

Ultraviolet-Visible spectroscopy is used to obtain the absorbance (or transmittance) of a compound in solution or in solid state. The measurement is the absorbance of the light energy or electromagnetic radiation which excites electrons from the ground state to the first singlet excited state of the material. The UV-Vis range is 1.5 – 6.2 eV, equivalent to wavelength of 800 – 200 nm. The Beer-Lambert law is the principle used to absorbance spectroscopy, as presented in Equation 3:

$$A(\lambda) = \varepsilon(\lambda)bc \qquad \text{Equation (3)}$$

where A is the measured absorbance as absolute number, ε is the molar absorptivity of the compound ($M^{-1}cm^{-1}$), *b* is the path length of the cuvette (usually 1 cm) and *c* is the concentration of the solution (M). UV-Vis spectroscopy data can give quantitative and qualitative information about the materials (BARRON, 1992).

UV-Visible spectra were acquired on a Shimadzu spectrophotometer UV-2450PC at EPCP-UPPA/France and in a Shimadzu UV-mini 1240 at LNMD – Unesp/Bauru, in solution in chloroform or in the form of thin films prepared using solutions 30 mg/mL in 1,2-dichlorobenzene deposited by spin coating using a first step of 500 rpm for 3 s and a second step of 3000 rpm for 60 s, as mentioned in the text.

2.2.12 Optical band gap

In order to calculate the bad gap values, UV-visible optical absorption of the solutions was used. The optical band gap is comparative with the electronic gap (MICARONI, 2002; JI, 2014). In this method, used for materials with the same multiplicity of spins, we graph the low-energy side of the absorption band as a plot of hv versus $(A \times hv)^2$, where hv is the photon energy in eV and A is the absorbance. A fit of the linear portion of this plot will then yield an intercept, which correspond to the optical bandgap.(TAUC, 1966)

2.2.13 Atomic Force Microscopy (AFM)

Atomic Force Microscopy (AFM) is a form of scanning probe microscopy (SPM) where a small probe is scanned across the sample to obtain information about the sample's surface. The information gathered from the probe's interaction with the surface can be as simple as physical topography or as diverse as measurements of the material's physical, magnetic, or chemical properties. The images are made as the probe is scanned in a raster pattern across the sample to form a map of the measured property relative to the X-Y position. Areas as large as 100 μm^2 to less than 100 nm^2 can be imaged (BINNIG, 1986).

The films were prepared using solutions 30 mg/mL in 1,2-dichlorobenzene deposited in glass or FTO by spin coating using a first step of 500 rpm for 3 s and a second step of 3000 rpm for 60 s. The films were analyzed without annealing in Bruker AFM equipment - Multimode 8 in EPCP – UPPA/France.

2.2.14 Cyclic Voltammetry (CV)

Cyclic voltammetry is a convenient tool to study electrochemistry reactions and obtain qualitative information about electron transfer processes. The voltage applied to the working electrode is scanned linearly from an initial value, E_i, to a predetermined limit, $E_{\lambda 1}$, (known as the switching potential) where the direction of the scan is reversed. The operator can halt the scan anywhere or let the instrument cycle between $E_{\lambda 1}$ and some other preselected value, $E_{\lambda 2}$. The current response is plotted as a function of the applied potential. Often there is very little difference between the first cycle and successive scans. However, the changes that do appear on repetitive cycles are important keys to unlocking information about reaction mechanism (MABBOTT, 1983).

Cyclic voltammetry was performed in a N_2 glovebox at ambient temperature using a Ag working electrode (diameter 1.6 mm), Ag/AgCl as reference electrode and a Pt wire as counter electrode. The three-electrode cell was connected to an Autolab potentiostat PGSTAT. The solutions (30 mg/mL in 1,2-dichlorobenzene) were droped on top of the working electrode and dryed to make a film. Acetonitrile and tetrabutylammonium hexafluorophosphate (0.1 M) was used as supporting electrolyte.

2.2.15 Energy levels calculation

Since the electrochemical measurements were carried out in solution, the values must be corrected with respect to the vacuum level, for each reference electrode and solution used (MICARONI, 2002; JI, 2014). In our system, the HOMO energy level can be estimated using Equation (4) and the LUMO Equation (5):

$$E_{HOMO} = [-e\ (E_{ox}^{\ onset} + 4.4)]\ eV \qquad \text{Equation (4)}$$

$$E_{gap} = E_{LUMO} - E_{HOMO} \qquad \text{Equation (5)}$$

where e is the elementary charge, E_{red} is the reduction potential. (MICARONI, 2002; NEMATI BIDEH, 2016)

2.2.16 Photoluminescence spectroscopy (PL)

Photoluminescence spectroscopy is a contactless, nondestructive method of probing the electronic structure of materials. Light is directed onto a sample, where it is absorbed and imparts excess energy into the material in a process called photo-excitation. One way this excess energy can be dissipated by the sample is through the emission of light, or luminescence. In the case of photo-excitation, this luminescence is called photoluminescence. Photo-excitation causes electrons within a material to move into permissible excited states. When these electrons return to their equilibrium states, the excess energy is released and may include the emission of light (a radiative process) or may not (a non-radiative process). The energy of the emitted light (photoluminescence) relates to the difference in energy levels between the two electron states involved in the transition between the excited state and the equilibrium state. The quantity of the emitted light is related to the relative contribution of the radiative process (BARRON, 1992; NREL, 2016).

The photoluminescence measurements were performed on a Varian fluorimeter - Cary Eclipse. The samples were measured in solution of chloroform with concentrations of $1x10^{-5}$ mg/mL.

2.2.17 Fluorescence lifetime imaging microscopy (FLIM)

Fluorescence lifetime imaging microscopy (FLIM) is a technique in which the mean fluorescence lifetime of a chromophore is measured at each spatially resolvable element of a microscope image. The avalanche detector can reponse at 70 ps. The nanosecond excited-state lifetime is independent of probe concentration or light path length but dependent upon excited-state reactions such as fluorescence resonance energy transfer. These properties of fluorescence lifetimes allow exploration of the molecular environment of macromolecules (BASTIAENS, 1999).

The measures confocal microscopy coupled with photoluminescence were performed in a fluorescence confocal microscope Zeiss (LSM model 780 inverted) with excitation by a (1P) and two (2P) photons ranging in the spectral region of 375 nm to 1100 nm. The samples were measured in solid state, as films for P3HT and nanoparticles for the grafted systems. Also, measurements in solution, nanoparticles suspended in chloroform, with concentrations of $1x10^{-5}$ mg/mL, were performed. These measurements were made at IQSC – USP with collaboration of Prof. Francisco E. G. Guimarães.

2.2.18 Electrical characterization

The solar cell performace is measured by performing an *J* - *V* curve, which is done by scanning an applied voltage across the solar cell and measure its current response. A solar simulator is typically used for precise measurements. In this way, it will be acquired a current voltage curve, where the current of the solar cell is plotted against the applied voltage. The power conversion efficiency (η) is calculated as shown in Equation (6):

$$\eta = \frac{P_{max}}{P_{in}} = \frac{V_{max} J_{max}}{P_{in}} \qquad \text{Equation (6)}$$

where V_{max} and J_{max} are, respectively, the voltage and the current density at which electric power generated by the cell is maximum (P_{max}).

Another important parameter in the study of solar cells is the fill factor given by Equation (7):

$$FF = \frac{V_{max} J_{max}}{V_{OC} J_{SC}} \qquad \text{Equation (7)}$$

where J_{sc} (A/cm^2) is the short curt photo-current (V = 0) and V_{oc} (V) is the open circuit voltage (J = 0).

Solar characterization of the devices was done in N_2 ambient, using a Keithley 2400 source meter unit and an Oriel Xenon Lamp (450 W) coupled with an AM1.5 filter as a light source and a light intensity of 100 mWcm^{-2}. Devices parameters were tested for at least 16 devices for each sample in University of Washington under supervision of Dr. Christine Luscombe.

CHAPTER 3

SYNTHESIS OF FULLERENE DERIVATIVES

Three similar comonomers of varying size were initially chosen to explore the effect of steric bulk on the feasibility of the polymerization. Aromatic-oxy-ether links were incorporated due to their expected photo-stability (SILVA, 2014). Furthermore, it was found that having oxygenated phenylene comonomers made a great difference to the ease of their synthesis. Initial attempts to prepare analogous comonomers without ether groups were made, however, the bromomethylation of the co-monomers in accordance with the work of van der Made *et al.* (VAN DER MADE, 1993), resulted in very low yields due to the inactivity of the aromatic substrate and the steric bulk of the alkyl chains that hinder the substitutions.

The successful route with ethylated comonomers is shown in Scheme 11. The first step consisted of a facile Williamson alkylation of hydroquinone (WANG, B., 1997), giving simple control over the steric bulk of the comonomer through varying the length of the side chain. The reactions were facile and smoothly formed bis-alkyl ethers with the groups -$O(CH_2)_7CH_3$ (**2**), -$O(CH_2)_{11}CH_3$ (**3**), and -$O(CH_2)_{15}CH_3$ (**4**) in respective yields of 54, 44 and 38 %. The reduction in yield with increasing chain length is most likely due to steric hindrance and increasing difficulty in purifying the products; indeed on attempting with higher ethers, for example, -$O(CH_2)_{14}CH_3$, although we managed yields of around 38 %, they were generally less consistent. We aimed to make the syntheses as simple as possible so **2** and **3** were recovered pure by reprecipitation in cold methanol, **4** would normally have necessitated column purification. We decided nevertheless to pursue the chemistry even with the later showing creamy brown color due to the presence of salts, confirmed by the ^{1}H NMR. The bisbromomethylation step leading to molecules **5, 6** and **7** was found to be more troublesome, as alluded to above. Made *et al.* showed that it was possible to bromomethylate small aromatic compounds using small excesses of HBr in acetic acid and paraformaldehyde (VAN DER MADE, 1993). With these sterically encumbered molecules we found that much greater quantities of HBr were required (*ca* 7 times excess); indeed, high temperatures alone did not help and more often led to mixtures of bis- and

tris-bromomethylated products. We also found that it was harder under these conditions to maintain consistent yields, although they were mostly not far from 50 %. Finally, azidization was found to be facile using NaN_3 (O'NEIL, 2007), where yields were consistently of the order of 67 %, except in the case of **10** where the larger side-chains again hindered the reaction and made purification more complex due to the waxy nature of the product. Attempts to prepare analogues of **8**, **9** and **10** with bis-azide groups attached directly to the aromatic ring, i.e., 1,4-diazido-2,5-bis(alkyloxy)benzene, to explore the possibility of *peri*-conjugation through proximate phenyl rings (KOOISTRA, 2010), gave consistently low yields (<20 %) in our hands, even when using promoted catalysts as detailed by Zhu *et al*. (ZHU, W., 2004a), and were not further explored. It should be noted that azides are well known for their explosive tendencies when employed with compounds of low carbon to nitrogen ratios (BRÄSE, 2005). Therefore, all reactions with sodium azide were above the commonly recognized safety limit for handling, i.e., at least 3 carbon atoms to each nitrogen atom in the azide carrying molecule (ZHU, W., 2004b).

Scheme 11: Syntheses of the comonomers and PAFs: a) 1-bromooctane, K_2CO_3, **1**, acetonitrile, 54 %; b) 1-bromododecane, K_2CO_3, **1**, acetonitrile, 44 %, c) 1-bromohexadecane, K_2CO_3, **1**, acetonitrile, 32 %;d) **2**, PFA, HBr, acetic acid, 48%, e) **3**, PFA, HBr, acetic acid, 64 %, f) **4**, PFA, HBr, acetic acid, 48 %, g) **5**, NaN_3, DMSO, 67 %, h) **6**, NaN_3, DMSO, 68 %, i) **7**, NaN_3, DMSO, 52 %, j) C_{60}, **8**, DCB, 56 %, k) C_{60}, **9**, DCB, 68 % l) C_{60}, **10**, DCB, 63 %.

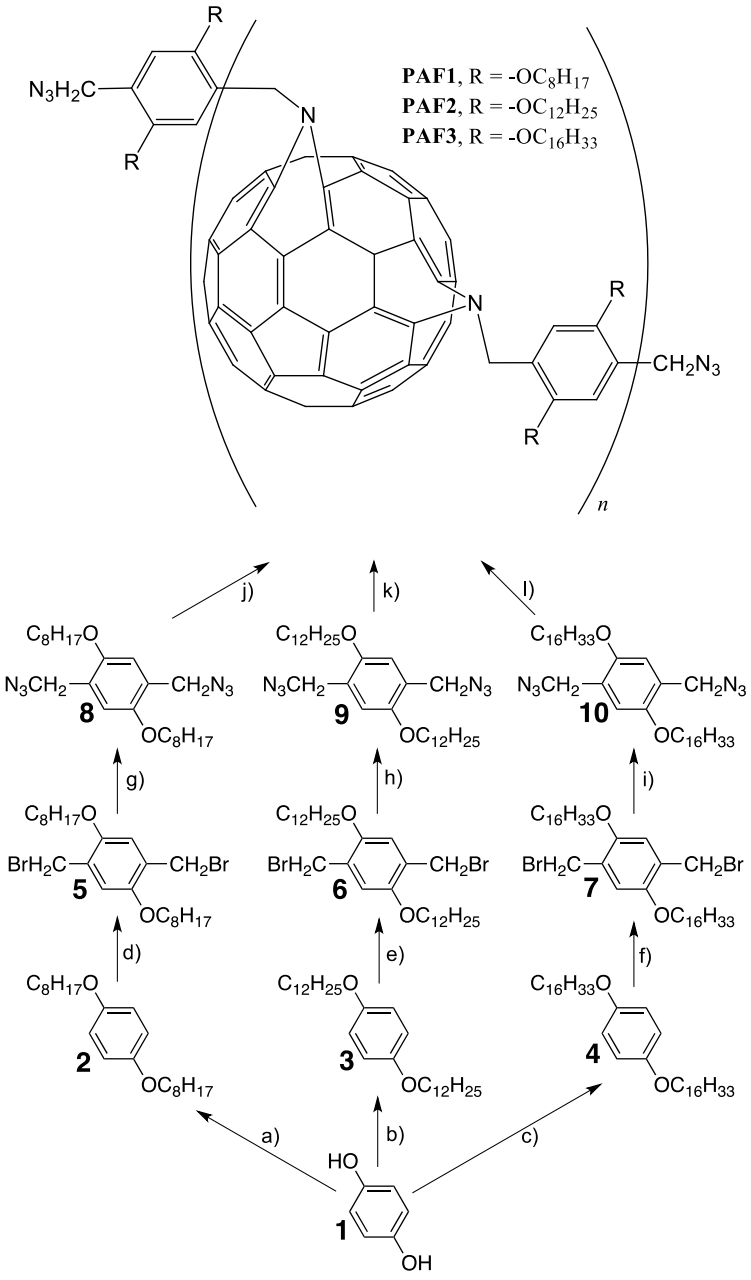

The syntheses of the PAFs were performed using a facile one-pot, two-step reaction. The mechanism of the cycloaddition of azidoalkyls to C_{60} is well understood (CASES, 2000). The

first step, at lower temperatures, involves the addition of the azide group to the fullerene [6,6]-bond between adjacent phenyl rings to give a full 5-membered ring. This intermediate is unstable on further heating so that with the loss of N_2 at around 100 ˚C, an adjacent [5,6]-bond is brought into the reaction and leads to the synthesis of open [5,6]-bridge azafulleroids with a single remaining nitrogen, as shown in the PAF structure in Scheme 11. A smaller number of closed [6,6]–bridge aziridino fullerenes also result (GRÖSSER, 1995; YANG, C., 2009a).

We were greatly encouraged by work identifying the preparation of bisadducts in high yields, even though the chemistry generally required long reaction times and temperatures from 70 ˚C up to reflux in chlorinated solvents (SCHICK, 1996). While reflux temperatures could have been chosen in order to drive the reaction forward towards high molecular weights, we minimized the risk of tris-additions, which would lead to cross-linking, by working at relatively low temperatures. This meant that long reaction times, of the order of a day, were used. The reaction was only warmed to higher temperatures at the end so as to drive off N_2 in the second step of the mechanism.

The polymerization can effectively be considered a polyaddition (IUPAC. COMPENDIUM OF CHEMICAL TERMINOLOGY; FLORY, 1953), and as such it is expected to deliver high molecular weights only when strictly equimolar quantities of the comonomer and C_{60} are used. Accordingly, care was taken over this point. It is possible to observe the formation of oligomers and low *Mw* polymers, as indicated in the SEC curve in Figure 10.

Figure 10: SEC curves of PAF1, PAF2 and PAF3 (THF, 30 ˚C, 350 nm).

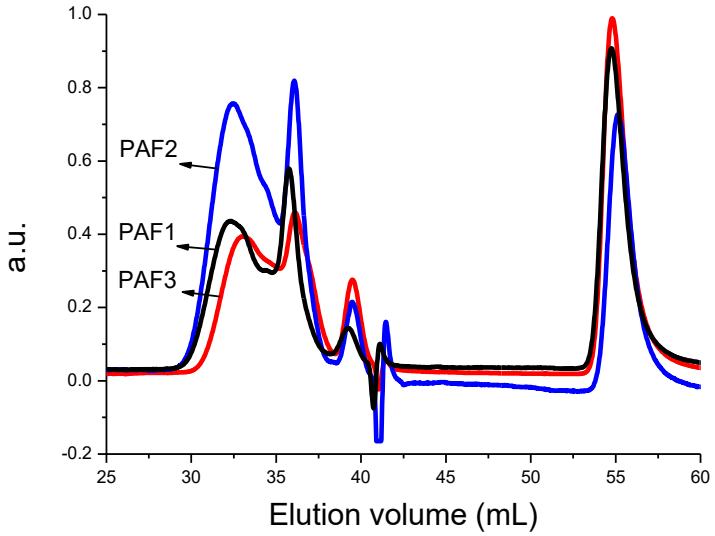

It is well known that C_{60} elutes very late from the SEC column, often appearing after toluene (AUDOUIN, 2004). Polystyrene standards cannot be used to indicate the correct masses, and those shown in Table 3 are clearly erroneous! A much more effective route was proposed by Gügel *et al.* (GÜGEL, 1996) whereby it is assumed that each addition of a repeating unit to the chain results in a definitive peak. Figure 10 indicates that PAF1 and PAF3 contains a large quantity (*ca* 15 % by deconvolution) of mono(azafulleroid) along with oligomers containing between 2 and around 12 C_{60}s. PAF2, however, contains much less mono(azafulleroid) but more dimers and increasingly large macromolecules up to around 14 repeating units i.e., equivalent to a molecular weight of *ca*. 17100 g mol^{-1}. The dispersities ($Đ = M_w/M_n$) (FLORY, 1953; R. F. T. STEPTO, 2009; R. C. HIORNS, 2012) are all lower than 2, the value expected from polyadditions (P. J. FLORY, 1936; FLORY, 1953; ODIAN, 2004). This reduction in $Đ$ is the result of the recovery and purification stages removing lower oligomers. That higher molecular weights were not attained was probably due to quite low reaction temperatures.

Table 3: Molecular weight distributions as indicated by SEC against polystyrene standards. Note that molecular weights should be multiplied from between 4 and 10 gain a better indication of the actual value. where *M*n = the number average molecular weight, *M*w = the weight average molecular weight and *Đ* = Polydispersity index.

Sample	*M*n (g mol^{-1})	*M*w (g mol^{-1})	*Đ*
PAF1	1090	1620	1.49
PAF2	1200	1935	1.62
PAF3	980	1430	1.46

The feasibility of the reactions was confirmed by the removal of the IR-peak at 2100 cm^{-1} due to *v* (N_3) vibrations of the comonomers, Figure 11.

Figure 11: FTIR data for PAF1, PAF2 and PAF3.

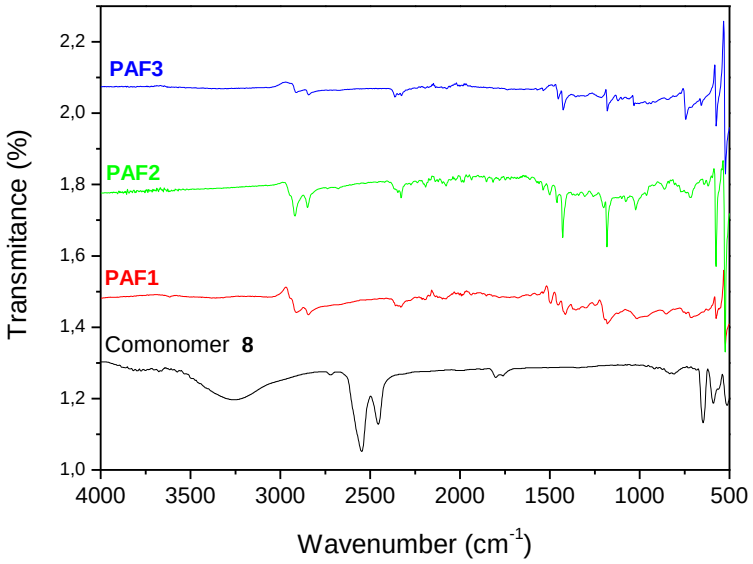

Much to our chagrin, it was not possible to easily purify the materials. While reprecipitation from chlorobenzene would have been preferred (YANG, C., 2009b), this risked excessive contact between the materials and air; fullerenes are known to easily form crosslinked ethers with oxygen (PENN, 1997). All were treated with extensive methanol and hexane Soxhlet

washing over a period of several days to respectively remove comonomers and fullerene, the latter known to be an effective technique when performed for long periods of time (RAMANITRA 2016). Assuming that the absorbance of C_{60} and the repeating unit are the same, deconvolution of the SEC curves of PAF1, PAF2 and PAF3 showed that they contained, respectively, 21, 38 and 40 % each of unreacted fullerene. This would either indicate that crosslinking was retaining impurities, or that non-bonding interactions between the tertiary amines and fullerenes are strong, suggesting that PAFs would be useful to arrest movement of fullerene in devices. Generally, the longer the alkyl chain, the easier the removal of C_{60}. As a general note, we found that the PAFs were extremely soluble when handled without drying; once they had been dried then their solubility was considerably reduced. The products were nevertheless submitted to simple solubility tests of 1 mg/mL in some commonly used solvents, and the results were found to be in accordance with expectations i.e., in the order of solubility PAF3 > PAF2 > PAF1. The solubility test picture is present in the Figure 12.

Figure 12: Photographs of solutions of C_{60}, PAF, PAF2 and PAF3, running from left to right, in 1,2-DCB, THF, chloroform, toluene and DMF.

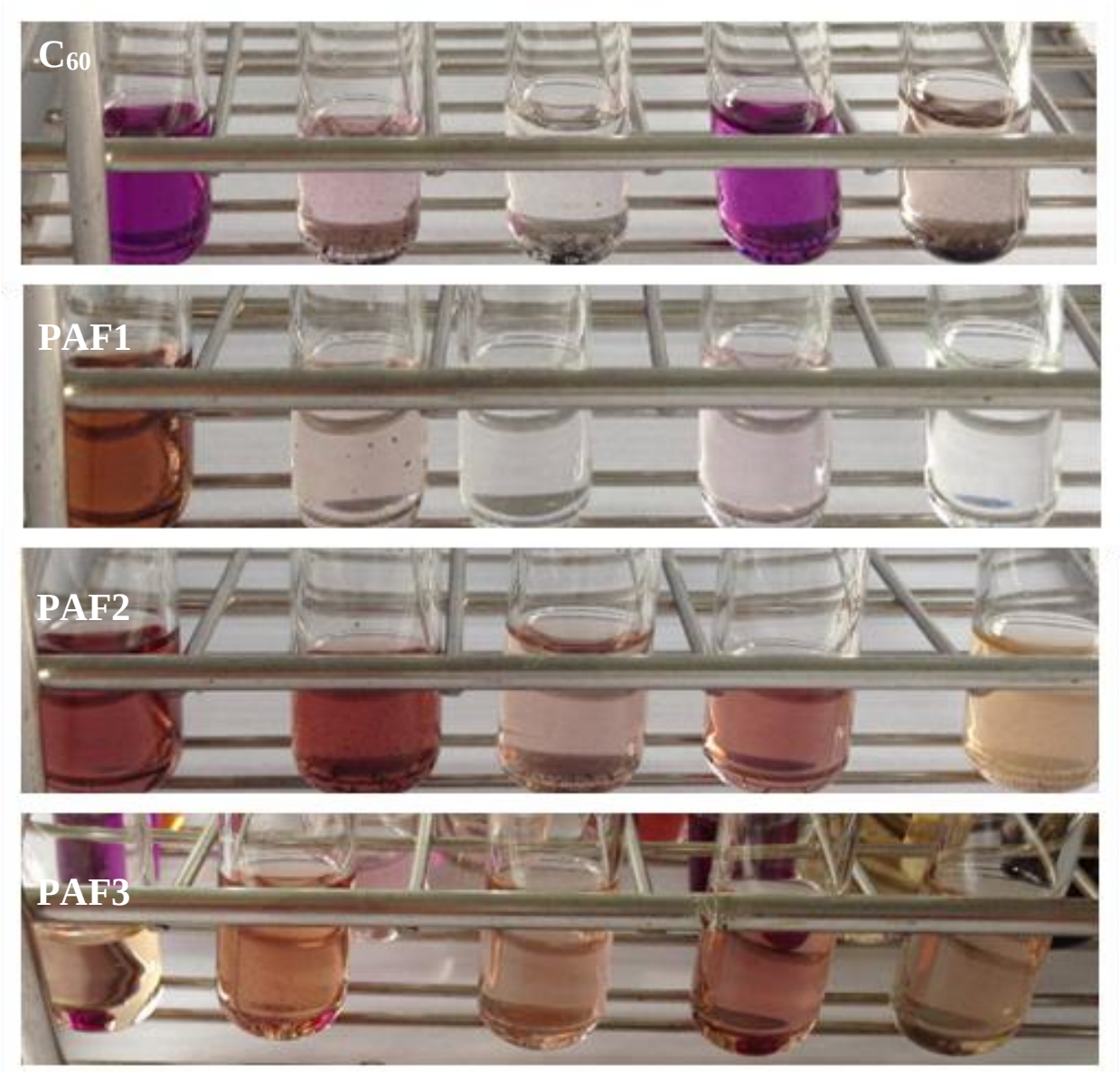

This difficulty in handling redissolution of the compounds meant that NMR studies were not facile. ^{13}C NMRs of the oligomers were not possible, and ^{1}H NMRs of PAF1 could not be carried out with C_6D_6 or $CDCl_3$, and 1,4-dichlorobenzene-d_4 gave only an initial glimpse of the structure as shown in Figure 13. The rapidly relaxing alkyloxy side-chains could be well observed with the oxymethylene at *ca* 4.3 ppm and alkyl protons from 0.9 to 2.3 ppm. The

chain-end (-CH_2N_3) groups could be surmised from peaks at around 5.3 ppm. The intra-chain methylenes (C_{60}=N-C*H*$_2$-) could not, however, be observed, most likely due to their low relaxation and the poor solubilisation of the macromolecule. The characterisation of PAF2 was more facile, even if the spectra had to be run overnight in C_6D_6. The NMR in Figure 14 shows similar peaks to those of PAF1, however, it is now possible to also find a wide doublet centred around 6.3 ppm (J = 220 Hz) indicative of the aforementioned intra-chain methylenes and confirming that they are in a highly restrained environment leading to their diastereotopic nature. The inequivalence of integrals pointed to highly different relaxation environments along the chain, in accordance with the proposed structure. However, it proved difficult to remove impurities, which may point to some cross-linking or strong interactions between fullerenes with amino-groups trapping solvents. For PAF3 the characterisation was even more difficult due to the amount of impurities, as presented in Figure 15. Even after excessive Sohxlet washing in various solvents such as methanol and hexane, the spectra presents a lot of unidentifiably peaks.

Figure 13: ^{1}H NMR (400.6 MHz, 1,4-dichlorobenzene-d4, 85 °C) of PAF1.

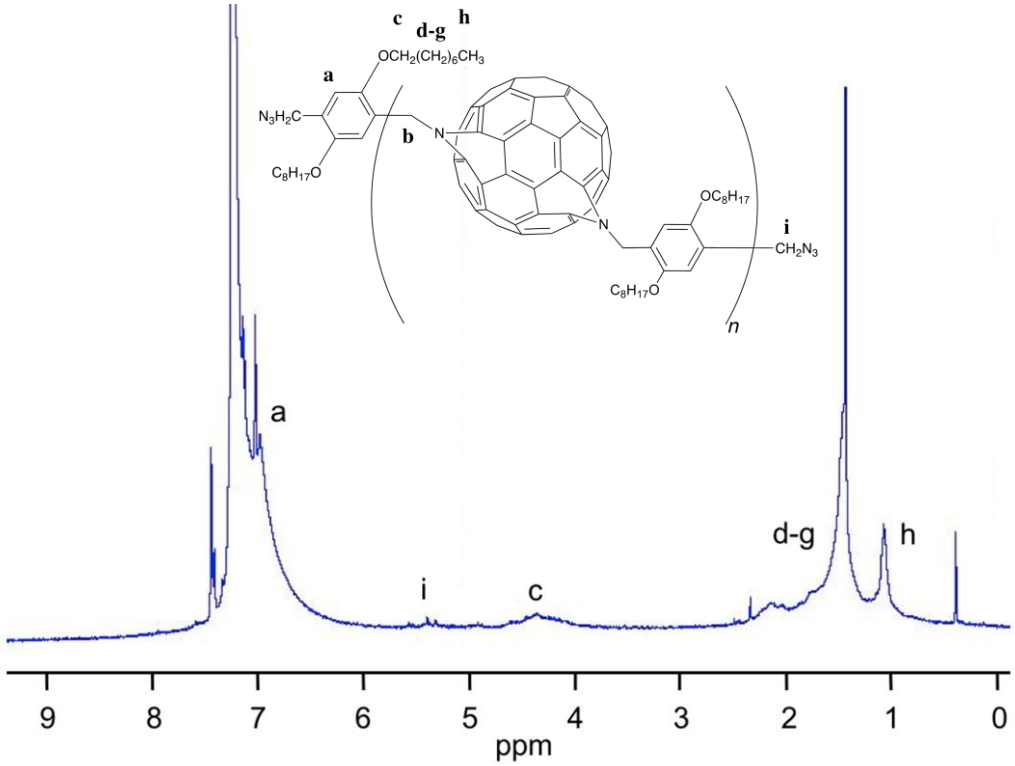

Figure 14: ^{1}H NMR (400 MHz, C_6D_6, room temperature) of PAF2. Note peaks due to impurities at 2.9 and 3.8 ppm, most likely arising from methanol.

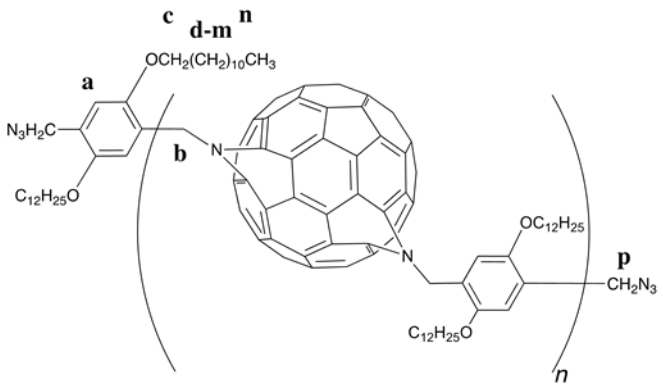

Figure 15: ^{1}H NMR (400 MHz, C_6D_6, room temperature) of PAF3. Note peaks due to impurities at 2.7, 2.3, 2.1 and 1.9 ppm, from solvents.

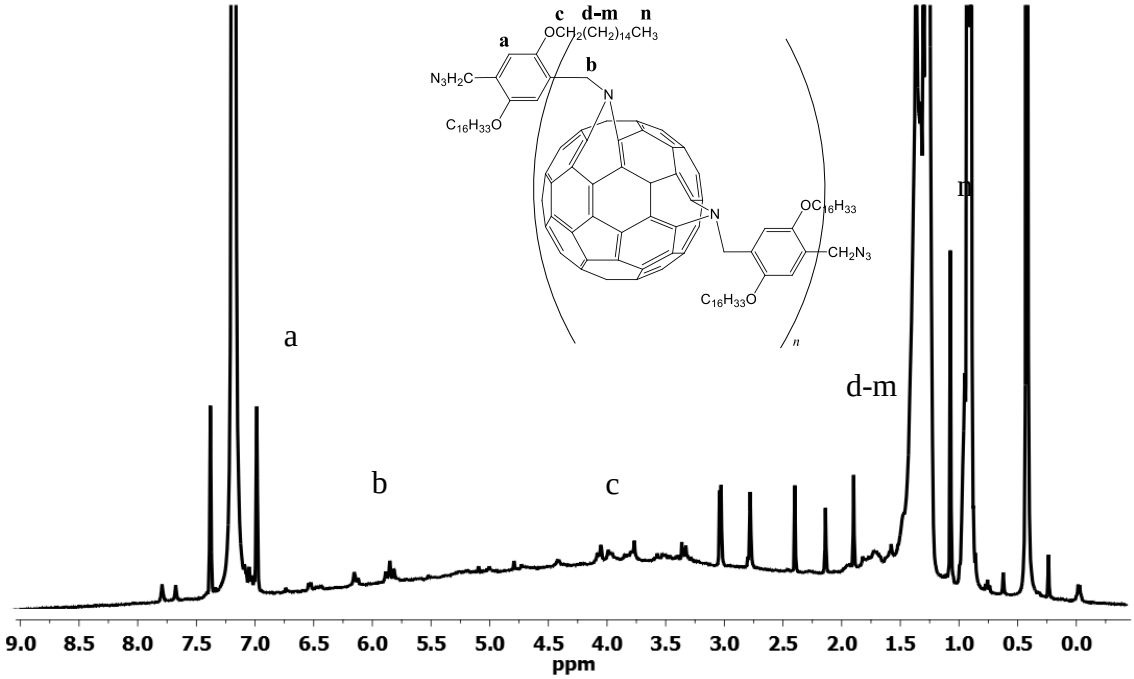

The thermal gravimetric (TG) studies, presented in Figure 16, showed a similar degradation passage for both polymers, PAF1 and PAF2 whereas PAF3 presents high thermal instability. PAF1 and PAF2 have degradation onsets at 100 and 80 ˚C, respectively leading to small but quantifiable losses of around 2 and 1 %wt, most likely arising from trapped solvents. Both undergo a second minor degradation from 160 ˚C up to 350 ˚C, of the order of 3 % wt. Given the small amount of the mass loss, it can be related to removal of excess N_2 from in-chain 5-membered rings to form the final aziridinofullerene products. Finally, PAF1 and PAF2 suffer, respectively, losses of 10 % wt at 360 and 4 % wt at 340 ˚C likely due to oxyalkyl side-chains. The process for PAF3 is very different, with around 9 % weight loss occurring between 50 and 160 ˚C, most likely due to solvents trapped in the long, waxy, side-chains and the inherent difficulties of purifying this material. Figure 17 shows a representative differential scanning calorimetry (DSC) thermogram of PAF2 where a glass transition, T_g is indicated at

240 °C. Given the high temperature it is probable that this transition arises from a main-chain rotation, suggesting that symmetrical in-chain *trans* isomers are preferred. To our knowledge this is the first example of a polyfullerene with a T_g. This may facilitate high temperature processing. PAF1 and PAF3, however, showed no clear characteristics.

Figure 16:Thermogravimetric study of: (a) PAF1; (b) PAF2; and (c) PAF3.

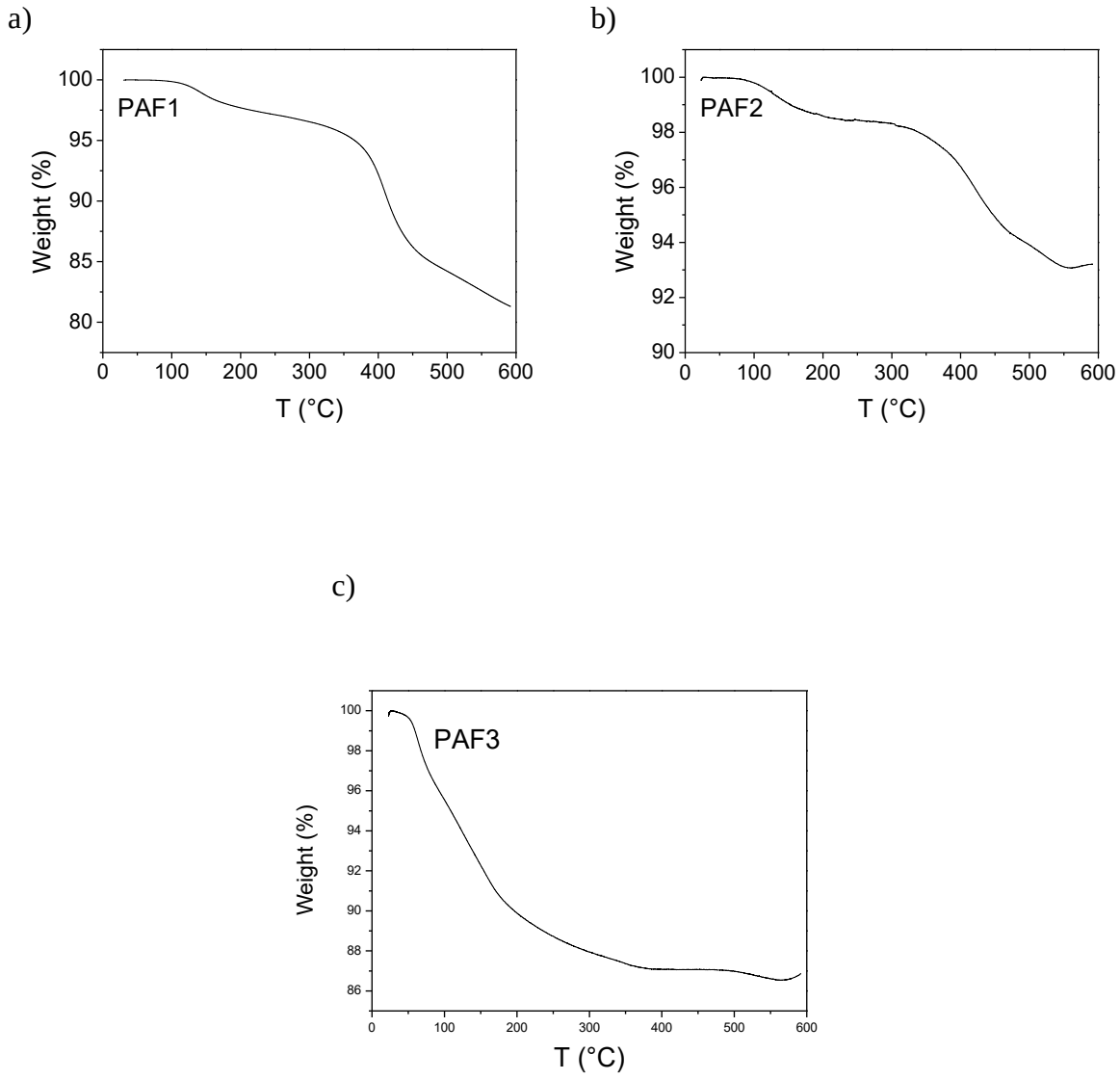

Figure 17: DSC thermogram of PAF2.

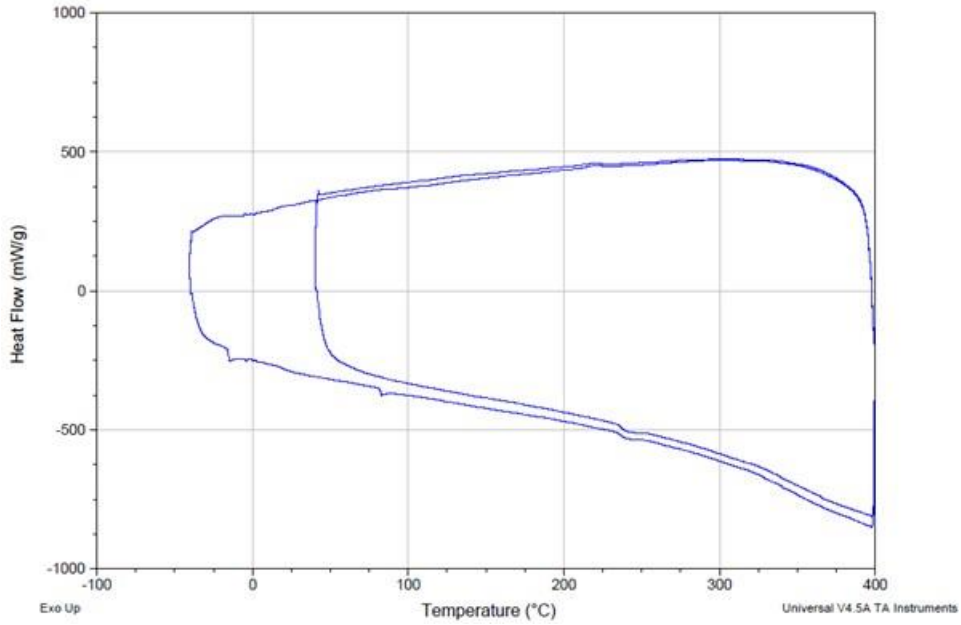

In an analogous reaction forming bisadducts, the *equatorial* bisadduct was found to be the most prevalent isomer, followed by *trans*-2, *trans*-3 and *cis*-3 isomers (SCHICK, 1996). We expected that the polymer would give rise to a mixture of isomers spread throughout the length of the macromolecules, with perhaps a lower number of *cis*-3 and equatorial isomeric repeating units due to steric forces resulting from the larger comonomers. Given the relatively low solubility of the oligomers with respect to the needs for NMRs, it was not possible to determine the ratio of various isomers in the structure.

In order to be able to perform initial studies of the electronic structures of the PAFs, it was assumed that the most likely structure would be that based on a *trans*-3 position due to steric effects of the comonomers and in-chain C_{60}s, in accordance with analogous cycloadditions reactions (RAMANITRA 2016). To reduce calculation time, a simple repeating unit of PAF1 was studied alone, therefore long-range conformational effects could not be taken in account. However, combining a semi-empirical (PM6 level) study, made by Ms. Rodrigo Marques Ferreira under Prof. Dr. Francisco Carlos Lavarda supervision, of the example *trans*-3 isomer,

to find the most stable conformer, and then by applying the DFT/B3LYP/6-31G(d) level of theory it was possible to find that the HOMOs and LUMOs were found to be, respectively, -5.23 and -2.98 eV with one adduct, and -5.14 and -3.05 eV for the bis-adduct. Figure 18 shows the frontier orbitals wherein one can see that the first LUMO is well and truly on the C_{60} and the HOMO on the comonomer, as is expected.

Figure 18: Representation of HOMO and LUMO frontier orbitals calculated at the DFT/B3LYP/6-31G(d) theoretical level.

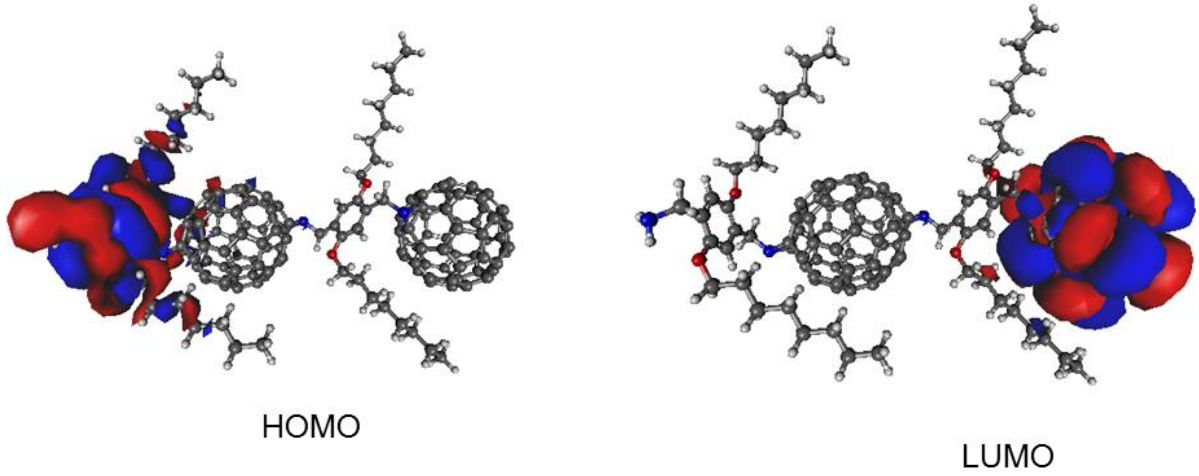

To empirically determine the HOMO and LUMO levels for the synthesized PAFs, cyclic voltammetry was performed on PAF1, PAF2 and PAF3. The voltammograms, Figure 19, exhibit two oxidation and reduction peaks. It is important to highlight that the samples were submitted to 30 cycles with slight degradation, demonstrating stability of the PAFs. The oxidation potential onset, E_{ox}, was calculated from the first oxidation peak and the gap using UV-vis spectra and calculated using the Tauc's plot, Figure 20. Since the measurements were carried out in solution, the values are corrected with respect to the vacuum level for each reference electrode and solution used (MICARONI, 2002; JI, 2014). The calculated values are presented in Table 4. There is a very similar values of the HOMO and LUMO energies in PAF1

and PAF2, which would tend to suggest greater crossover and interactions between C_{60} orbitals in the former macromolecule. Aside from PAF3, there are few variations between the PAF samples. When compared to PCBM though, we can see that the reduction values are more negative by around 80 mV or so. Prior work has shown a similar, if not quite so strong a reduction, for mono-adducts (YANG, C., 2009a) where the higher electronegativity of the nitrogen atom relative to carbon explains the reduced electron density in the fullerene shell. With the bis-additions in PAF1, PAF2 and PAF3, a major reduction in the electronic density can be expected.

Figure 19: Cyclicvoltammetry of (a) PCBM; (b) PAF1; (c) PAF2 and (d) PAF3. The oxidation potential (E_{ox}) is pointed by the blue arrow and the reduction potential (E_{red}) is pointed by the red arrow.

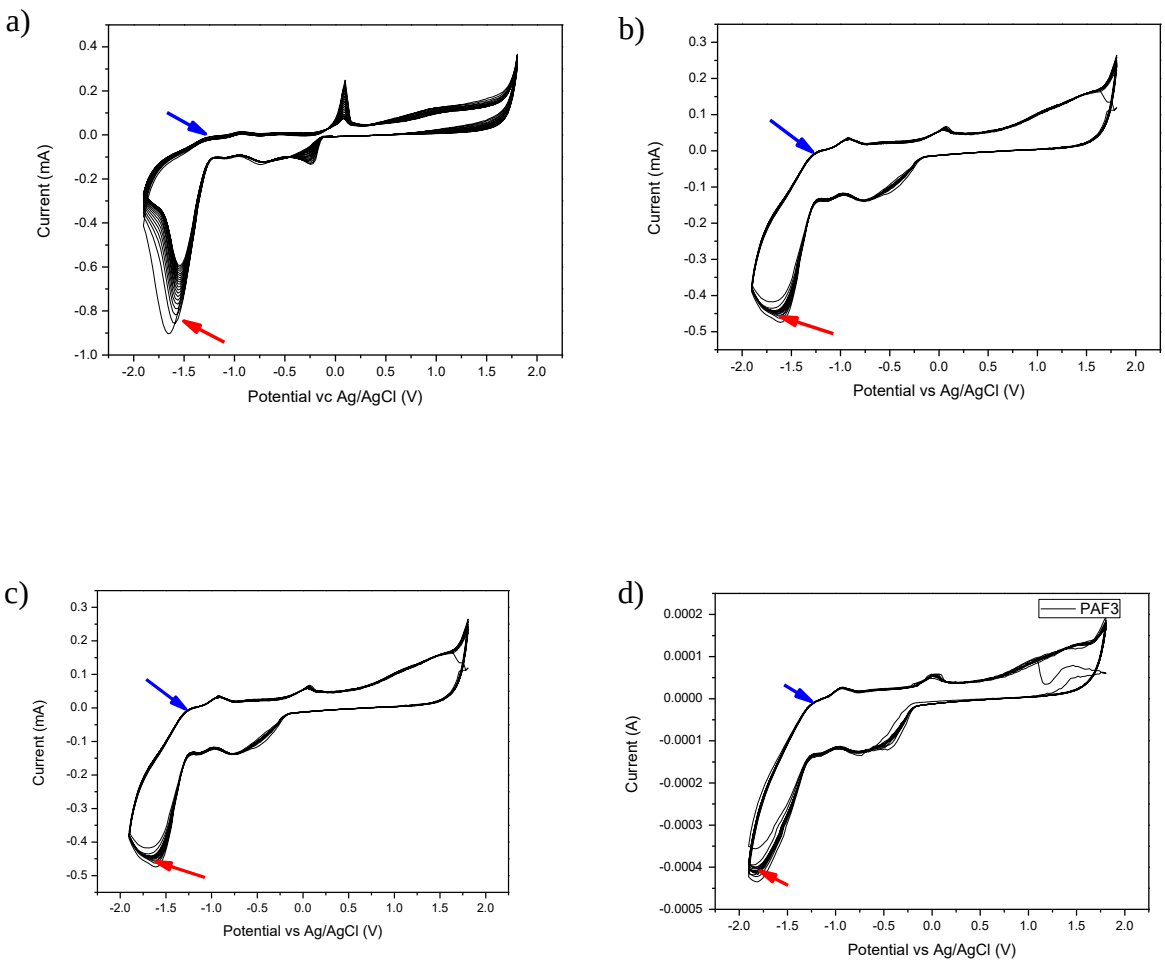

Figure 20:Tauc's plot used to calculate the optical band gap.

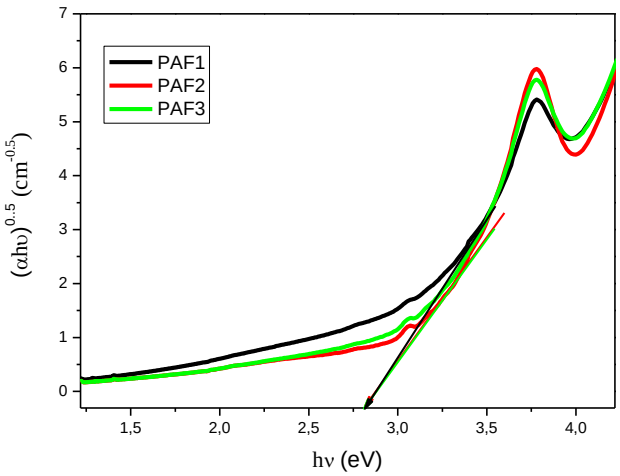

Table 4: Electronic data for PCBM and the PAFs.

Sample	**E_{ox}**	**$E_{1/2}$**	***E*LUMO (eV)**	***E*gap (eV)**	***E*HOMO (eV)**
PCBM	-1.29	-1.44	-3.64	1.9 (1.7)*	-5.69 (5.74 to 5.54)*
PAF1	-1.27	-1.44	-2.86	2.81	-5.67
PAF2	-1.27	-1.52	-2.86	2.81	-5.67
PAF3	-1.25	-1.54	-2.84	2.81	-5.65

* maximum and minimum values reported.

Figure 21 shows the UV-Visible absorption characteristics of C_{60}, PAF1, PAF2 and PAF3 in chloroform. PAFs show well-defined UV curves would indicate that the materials are well dissolved, and do not undergo aggregative behaviour in solution. Both PAF1 and PAF2 retain the main opto-electronic features of C_{60}. However, there is an increased absorption at around 400-600 nm due to the modification of the C_{60} sphere, which would tend to hint that there are more LUMO states available for charge transfer. PAF3 however does not show the characteristic peaks from C_{60}. Interestingly, it is possible to relate the colours of the solution to the structures of the materials. PAF solutions, shown in Figure 12, present red wine colours, similar to those found by Kim *et al*. (KIM, G., 2013) for [5,6]-open azafulleroids. Further evidence that PAFs are based on [5,6]-open azafulleroid repeating units can be found on closer

inspection of the UV-visible curves. Notably, the characteristic absorption for [6,6]-closed fullerene derivatives at 420 nm is not observed (YANG, C., 2009a; KIM, B., 2012) whereas the shoulder at ~ 416 nm, characteristic of an open fulleroid structure (KIM, G., 2013), is seen (detailed in Table 5). Significantly, PAFs absorptions are stronger than those for C_{60} in the visible range, possibly benefiting solar light harvesting and photocurrent conversion for devices.

Table 5: Comparison of absorption peaks of PAFs and C_{60} in chloroform.

Compound	**Absorption (nm)**
C_{60}	330, 405, 540, 600, 623(sh)
PAF1	329, 405, 416, 540, 602
PAF2	328, 405, 416, 540, 600
PAF3	328, 405, 449, 600

Figure 21: UV-Visible absorption spectra of solutions of C_{60}, PAF1, PAF2 and PAF3 in chloroform.

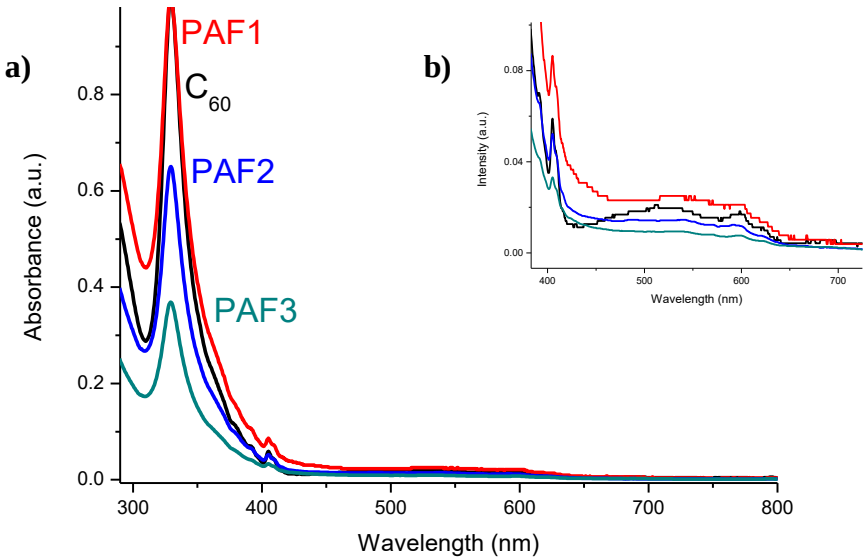

For the deposition of films, solutions with concentration of 30 mg/mL of each PAF in o-DCB were prepared. The solution was deposited in glass by spin coating using 500 rpm for

3 s and 3,000 rpm for 30 s. PAF1 films showed little uniform coating of the substrate. However, PAF2 and PAF3 films showed good homogeneity and uniform coating.

The transmittance spectra of the films were conducted and presented in Figure 22. These spectra shown similar behavior for PAF2 and PAF3 samples, however, PAF1 presents different spectrum without the characteristic band at around 400 nm, which may suggest the sample is oxidized.

Figure 22: Transmittance spectra for PAFs thin films.

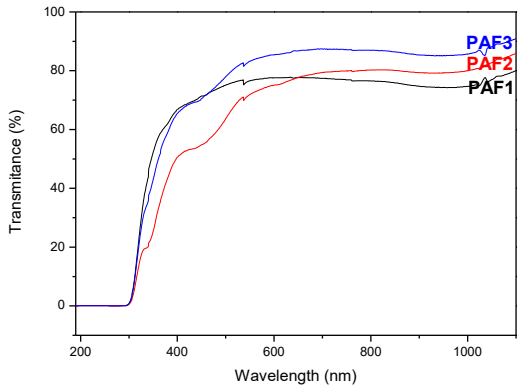

In order to analyze the surface of the films, AFM measurements were performed for PAF1 and PAF2. Analyzing the AFM images, Figure 23, it is possible to observe that the films are homogeneous, without the formation of aggregates. The calculated roughness (RMS) is around 1 nm, low value for this type of material.

Figure 23: AFM for a) PAF1 and b) PAF2 films.

a)

b)

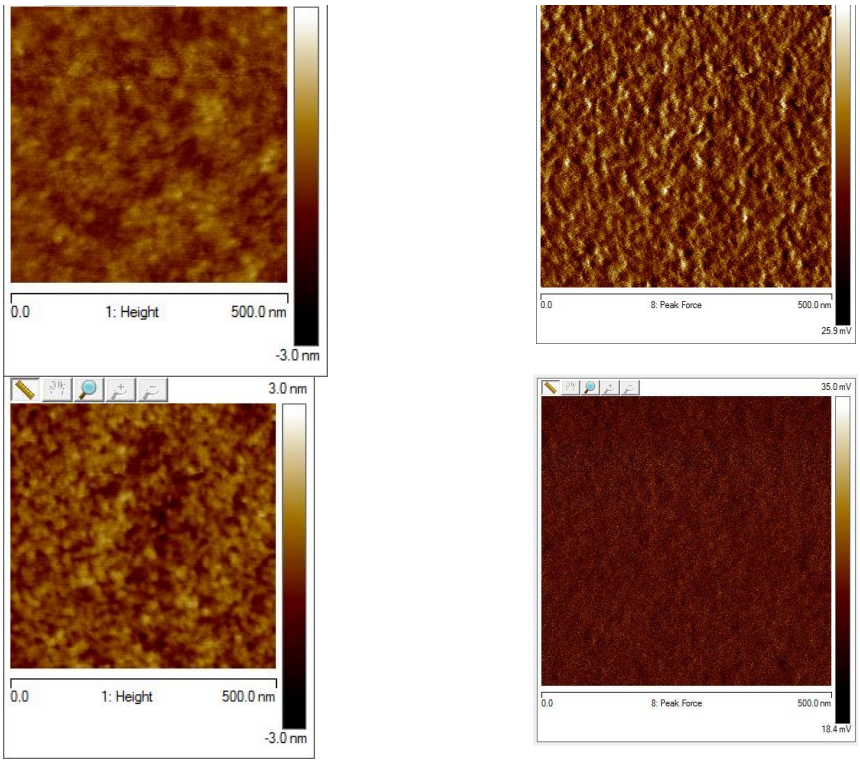

Usual configuration organic solar cells (ITO/PEDOT:PSS/active layer/aluminium) were made combining P3HT with the as-prepared PAFs. Devices with commercial $PC_{61}BM$ were also fabricated and used as reference cells to compare PAF1, PAF2 and PAF3. Figure 24 show the photovoltaic characteristics for all four devices. The performance of the devices constructed with the PAFs synthetized by us were lower than those made by PCBM, with average power conversion efficiencies around 0.19, 1.38 and 0.54 % for PAF1, PAF2 and PAF3 respectively and 2.64 % for PCBM based devices. Analougous system as the stardard, in the literature, have obteained efficiency up to 3.05 %. (GONZÀLEZ 2015)

Figure 24: Statistical studies (at least 10 devices) of the photovoltaic devices made using PAFs or PCBM with P3HT.

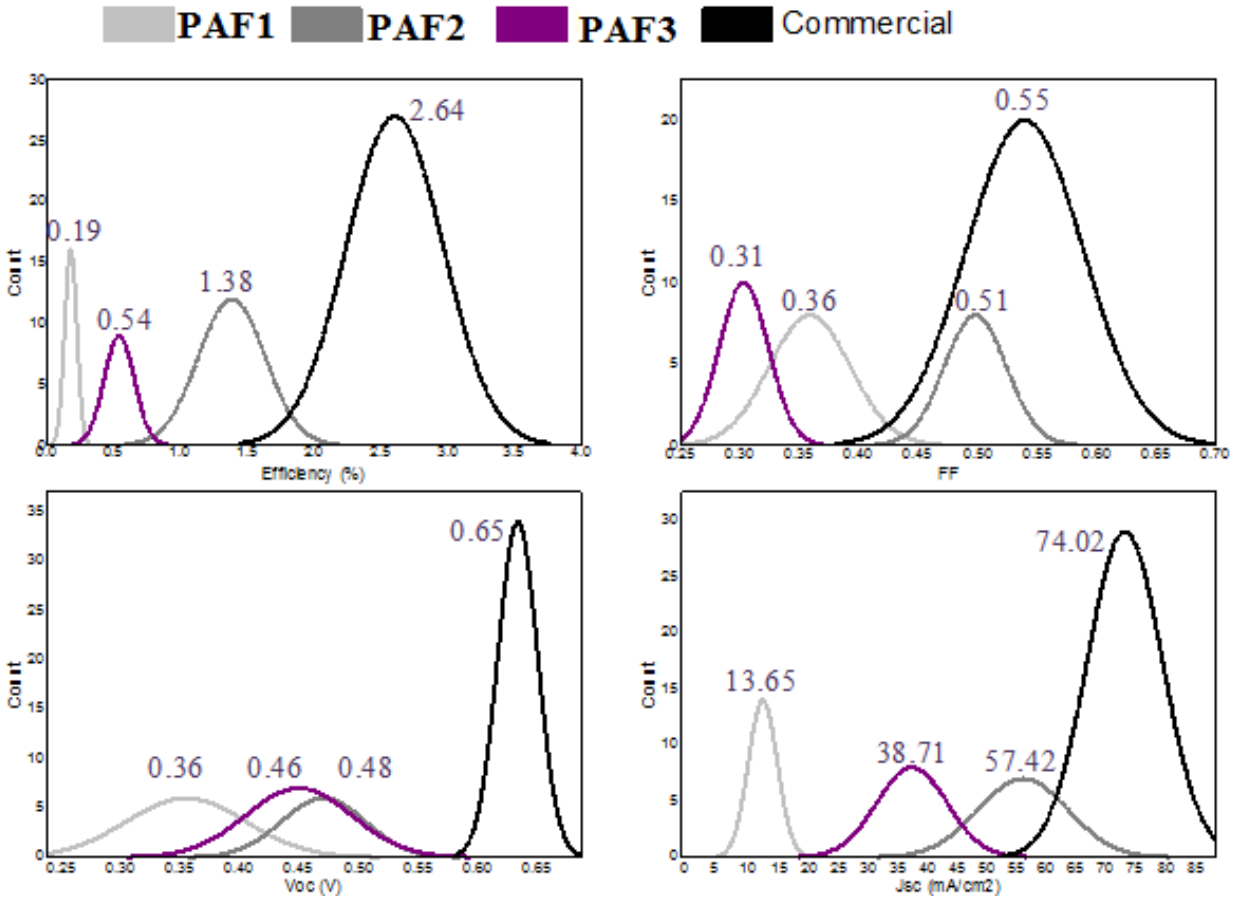

The devices were re-made with purified products by Sohxlet washes with methanol and hexane. The devices were made using only PAF1 and PAF2, once PAF3 even further the second purification still has impurities. The results are presented in Figure 25, 26 and Table 5. Performance of the devices made using re-purified PAFs were still lower than those made by PCBM, with average power conversion efficiencies around 0.2 % and 1.4 % for PAF1 and PAF2 respectively and 2.6 % for PCBM Nevertheless, PAF2 shows an enhanced final performance (V_{OC}, J_{SC}, and *FF*) in comparison to PAF1. The improvement of short circuit current and fill factor can be related to a better electron transport favoured for the PAF2 structure. It should be stated that these devices were made from electrodes and solvents that were non-optimised for the PAF materials, and as such the values can be considered very encouraging for initial results.

Figure 25: *J-V* curves of the photovoltaic devices made using PCBM, PAF1 and PAF2.

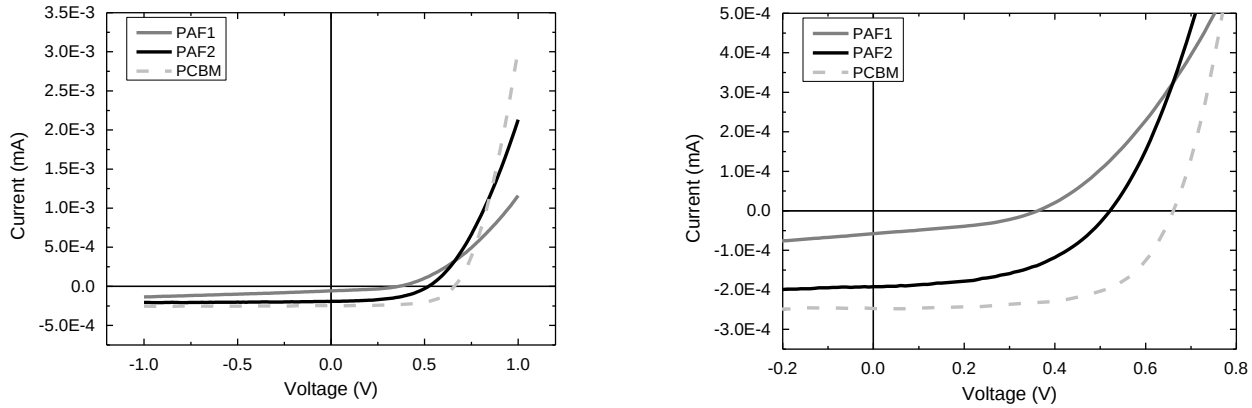

Figure 26: Statistical studies of the main parameters (16 devices for PAFs and 56 for PCBM).

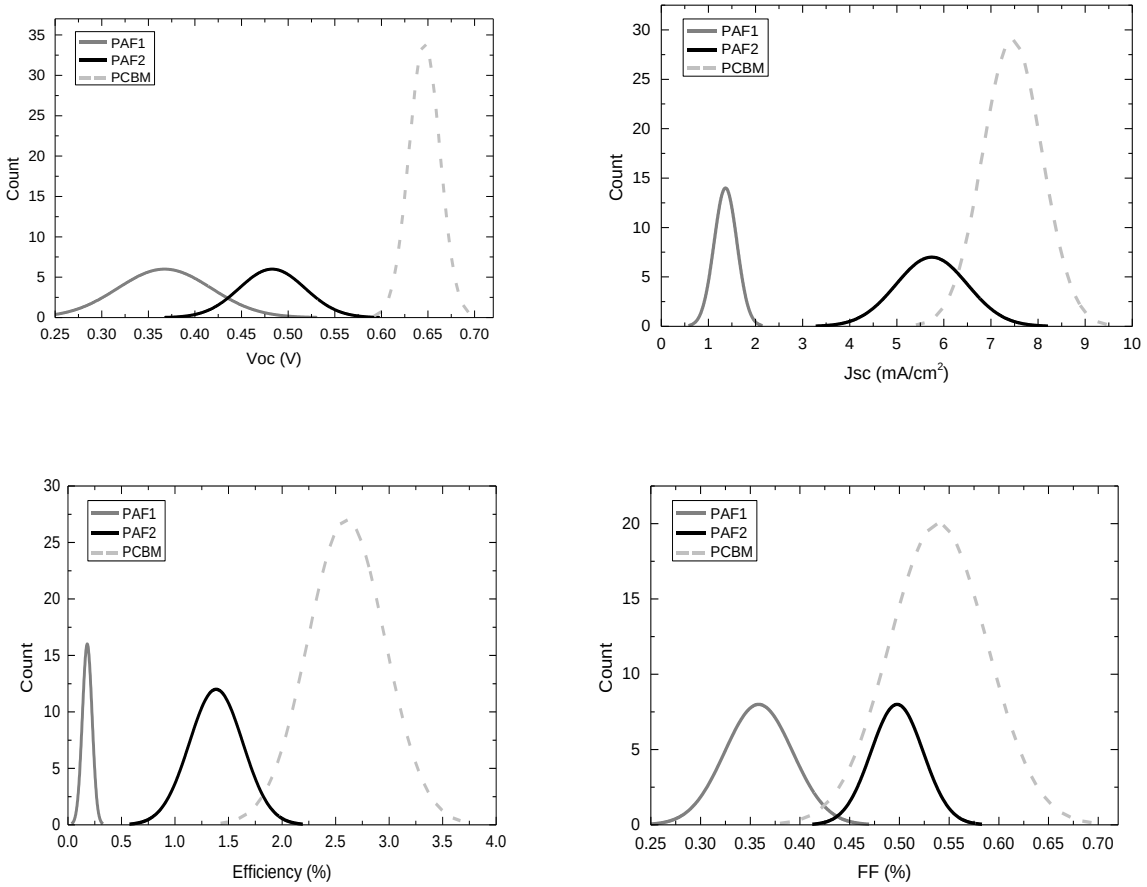

Table 6: Summary of the results shown in Figure 25, where SD denotes standard deviation.

Sample	V_{OC} **(V)**	J_{SC} **(mA/cm^2)**	***FF* (%)**	η **(%)**
PCBM	0.65 (± 0.01)	7.5 (± 0.6)	0.54 (± 0.05)	2.64 (±0.3)
PAF1	0.37 (± 0.04)	1.36 (± 0.2)	0.36 (± 0.02)	0.19 (±0.04)
PAF2	0.48 (± 0.03)	5.74 (± 0.7)	0.50 (± 0.03)	1.38 (± 0.2)

Conclusion

In conclusion, we have discovered a novel route, easy and clean, to polymerize C_{60}. The oligomers are formed by a polyadditon by way of [3+2] cycloadditon mechanism. Based on NMR and UV-Visible results, the predominant structure obtained was the [5,6]-open azafulleroid. The materials obtained were soluble in various organic solvents, and produced homogeneous thin films. However, resolvation can prove difficult where required. Additionally, the theoretical study of the electronic levels enables raised LUMO levels, in accordance with the experimental electronic studies results. Solvation and opto-electronic properties are improved for PAF2 and future studies will vary side-chains to permit extensive studies. The initial OPV results of the materials make them worthy of further attention. For the solar cells, PAF2 exhibited the best photovoltaic performance with a 1.38 % efficiency for the cell, and a FF comparable to the standard PCBM devices.

NMR SPECTRA

Comonomers Synthesis

Synthesis of 1,4-bis(octyloxy)benzene (2)

Hydroquinone (10.0 g, 0.09 mol) and K_2CO_3 (37.6 g, 0.27 mol) were stirred with acetonitrile (100 mL) for 30 min at room temperature under nitrogen. 1-Bromooctane (12 mL, 0.07 mol) was added dropwise and the reaction heated at reflux for 48 h. On cooling to room temperature, the solution was dropped into iced water (500 mL) and the product recovered by filtration. Purification was performed by twice dissolving the product in chloroform and precipitating it from methanol to yield white crystals (43.7 g, 54 %).

^{1}H NMR (400.6 MHz, $CDCl_3$) δ = 0.91 (s, 6H -$OCH_2(CH_2)_6CH_3$), 1.32-1.85 (m, 24H, -$OCH_2(CH_2)_6CH_3$), 3.95 (t, 4H, -$OCH_2(CH_2)_6CH_3$), 6.87 (s, 4H, aromatics) ppm.

Figure 27: ^{1}H NMR (400 MHz, $CDCl_3$, room temperature) of 1,4-bis(octyloxy)benzene (**2**). Note peak at 1.56 and 3.43 ppm respectively due to water and methanol impurities.

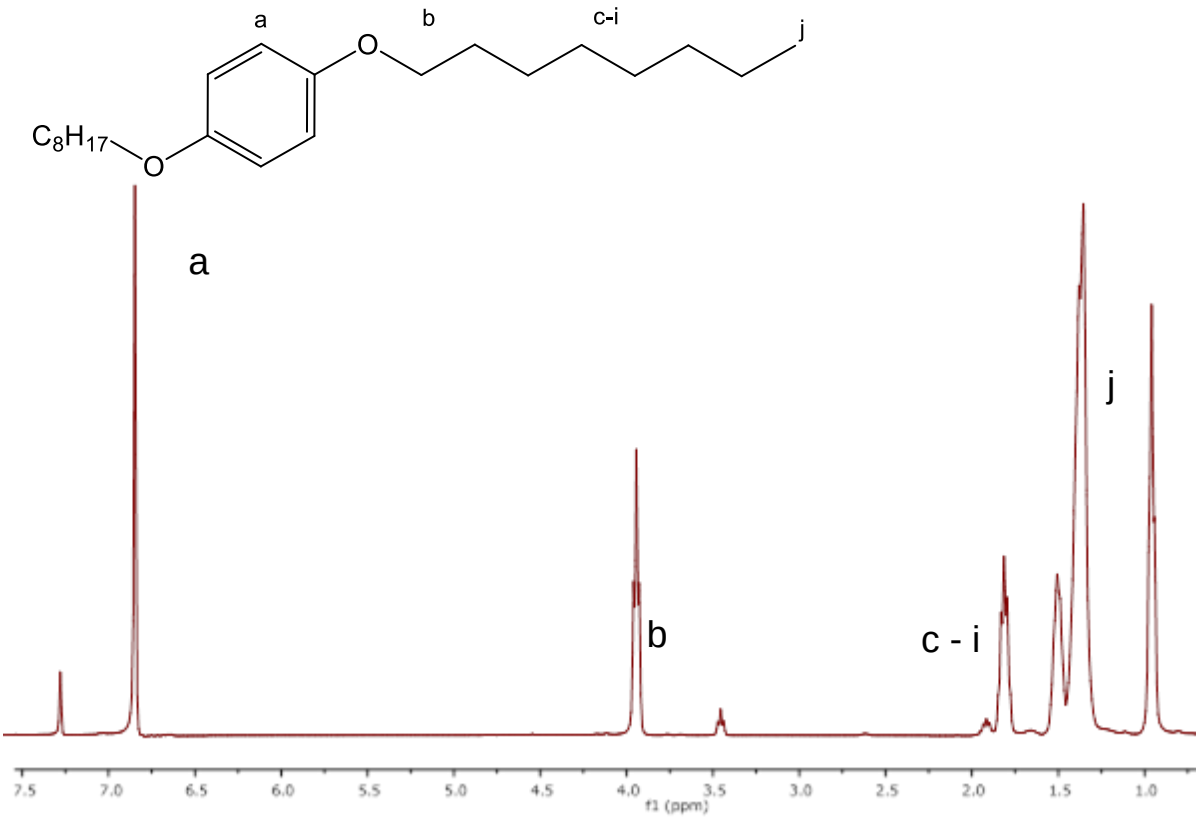

Synthesis of 1,4-bis(dodecyloxy)benzene (3)

Hydroquinone (5.0 g, 0.045 mol) and K_2CO_3 (18.82 g, 0.14 mol) were stirred with acetonitrile (100 mL) for 30 min at room temperature under nitrogen. 1-Bromododecane (32.7 mL, 0.014 mol) was added dropwise and the reaction heated at reflux for 48 h. Once cooled to room temperature, the solution was dropped into iced water (500 mL) and the product recovered by filtration. Purification was performed by twice dissolving the product into chloroform and precipitating it from methanol to yield a white crystalline material (18 g, 44 %).

^{1}H NMR (400 MHz, ambient temperature, $CDCl_3$) δ = 0.91 (t, *J* = 6 Hz, 6H, -C*H*$_3$), 1.51–1.22 (m, 36H, -C*H*$_2$-), 1.78 (t, *J* = 8 Hz, 4H, -C*H*$_2$-), 1.88 (t, *J* = 6 Hz, 4H, -C*H*$_2$-), 3.92 (t, *J* = 6 Hz, 4H, -O-C*H*$_2$), δ 6.84 (s, 4H, -*aromatic*) ppm.

Figure 28: ^{1}H NMR (400 MHz, $CDCl_3$, room temperature) of 1,4-bis(dodecyloxy)benzene (3). Note peak at 3.45 ppm due to methanol impurity

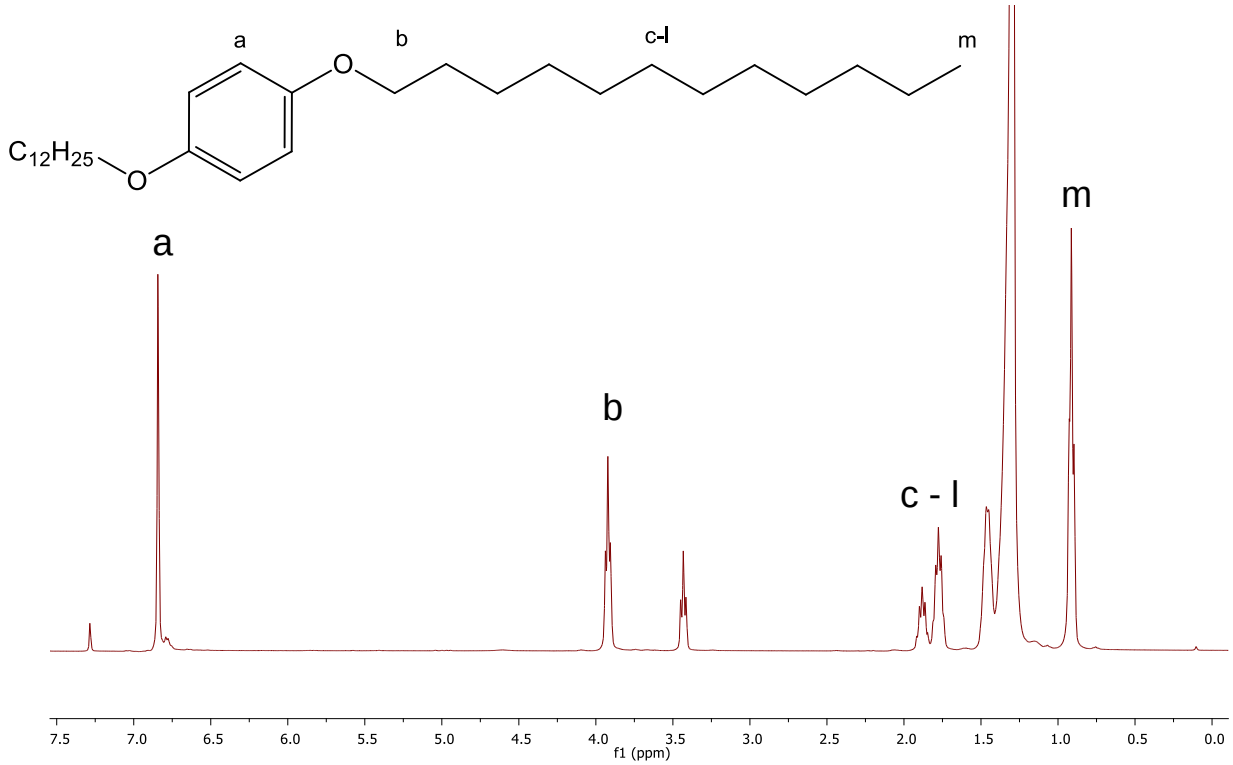

Synthesis of 1,4-bis(hexadecyloxy)benzene (4)

Hydroquinone (5.0 g, 0.045 mol) and K_2CO_3 (18.82 g, 0.14 mol) were stirred with acetonitrile (100 mL) for 30 min at room temperature under nitrogen. 1-Bromohexadecyldecane (41.6 mL, 0.14 mol) was added dropwise and the reaction warmed to reflux for 48 h. Once cooled to room temperature, the solution was dropped into iced water (500 mL), and the product recovered by filtration. Purification was performed by twice dissolving the product into chloroform and precipitating it from methanol to yield a white crystalline material (16 g, 31 %).

^{1}H NMR (400 MHz, ambient temperature, $CDCl_3$): δ 6.84 (s, 4H, -*aromatic*), 3.93 (t, *J* = 6 Hz, 4H, -O-C*H*$_2$), 1.87 (q, *J* = 6 Hz, 4H, -C*H*$_2$-), 1.78 (q, *J* = 6 Hz, 4H, -C*H*$_2$-), 1.51–1.22 (m, 56H, -C*H*$_2$-), 0.91 (t, *J* = 6 Hz, 6H, -C*H*$_3$).

Figure 29: ^{1}H NMR (400 MHz, $CDCl_3$, room temperature) of 1,4-bis(hexadecyloxy)benzene (**4**).

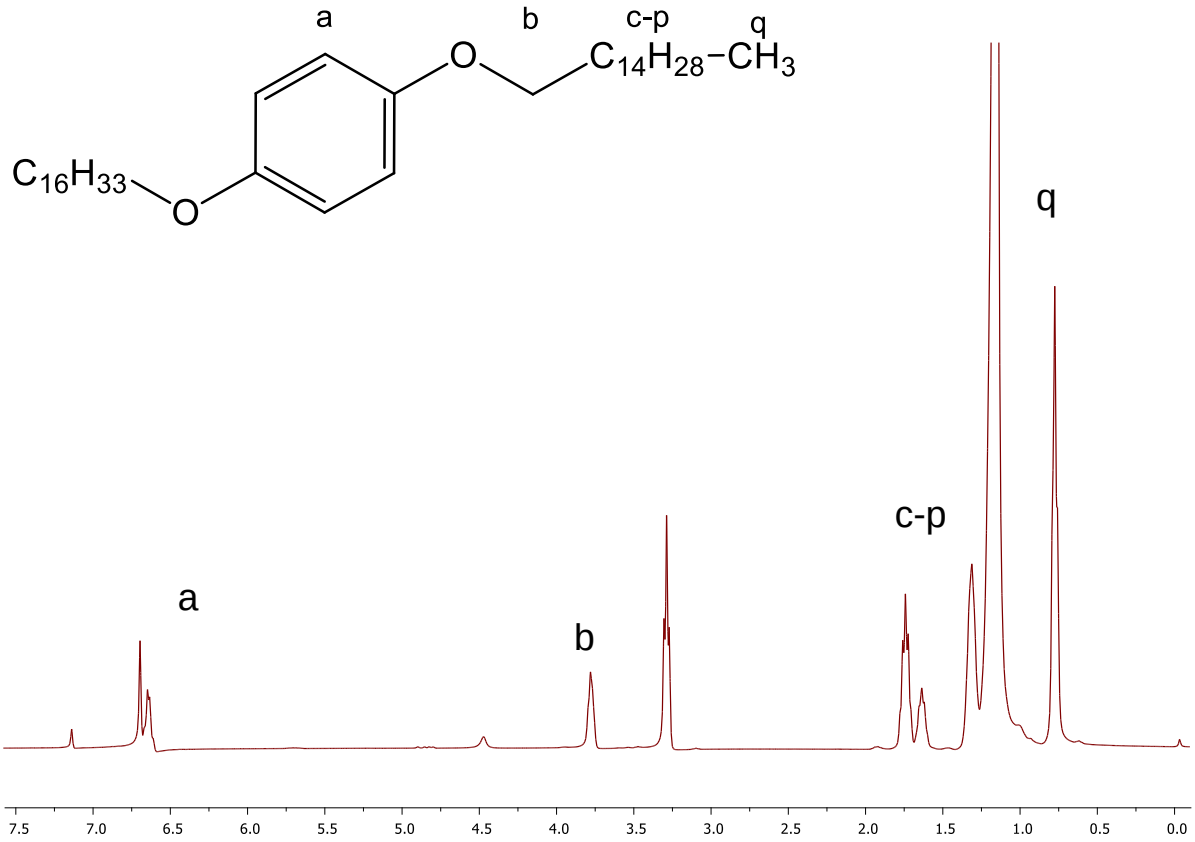

Synthesis of 1,4-bis(bromomethyl)-2,5-bis(octyloxy)benzene (5)

1,4-Bis(octyloxy)benzene (5.0 g, 0.015 mol) and the paraformaldehyde (1.12 g, 0.04 mol) were stirred with acetic acid (150 mL) under nitrogen. HBr 31 % in acetic acid (8.3 mL, 0.05 mol) was added dropwise and the reaction warmed to 70 °C for 2 h. Once cooled to room temperature, the solution was quenched with 300 mL of water and the product recovered by filtration. Purification was performed by twice dissolving the product into chloroform and precipitating it from methanol to yield a brownish material (3.78 g, 48 %).

^{1}H NMR (400.6 MHz, $CDCl_3$) δ = 0.91 (t, 6H -$OCH_2(CH_2)_6CH_3$), 1.32-1.85 (m, 24H, -$OCH_2(CH_2)_6CH_3$), 4.01 (t, 4H, -$OCH_2(CH_2)_6CH_3$), 4.55 (s, 4H, -CH_2Br), 6.87 (s, 4H, aromatics) ppm.

Figure 30: ^{1}H NMR (400 MHz, $CDCl_3$, room temperature) of 1,4-bis(bromomethyl)-2,5-bis(octyloxy)benzene (**5**). Note peaks at 1.8 and 3.5 ppm, respectively, due to water and methanol impurities.

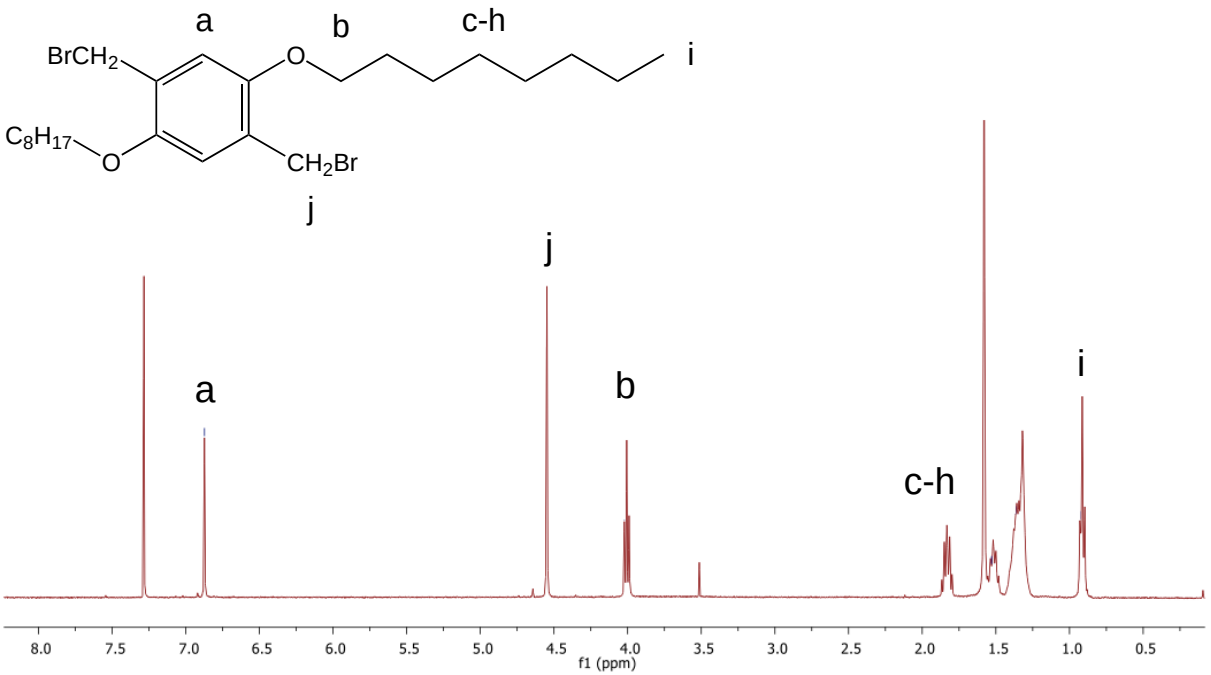

Synthesis of 1,4-bis(bromomethyl)-2,5-bis(dodecyloxy)benzene (6)

1,4-bis(dodecyloxy)benzene (5.0 g, 0.011 mol) and the paraformaldehyde (0.84 g, 0.028 mol) were stirred with acetic acid (150 mL) under nitrogen. HBr 31 % in acetic acid (6.8 mL, 0.036 mol) was added dropwise and the reaction warmed to 70 °C for 2 h. Once cooled to room temperature, the solution was quenched with 300 mL of water and the product recovered by filtration. Purification was performed by twice dissolving the product into chloroform and precipitating it from methanol of yield a brownish material (4.5 g, 64 %).

^{1}H NMR (400.6 MHz, $CDCl_3$) δ = 0.91 (t, 6H -$OCH_2(CH_2)_{10}CH_3$), 1.20-1.55 (m, 36H, -$OCH_2(CH_2)_{10}CH_3$), 1.83 (m, 4H, -CH_2-), 4.00 (t, *J* = 6 Hz, 4H, -$OCH_2(CH_2)_{10}CH_3$), 4.56 (s, 4H, -CH_2Br), 6.87 (s, 2H, aromatics) ppm.

Figure 31: ^{1}H NMR (400 MHz, $CDCl_3$, room temperature) of 1,4-bis(bromomethyl)-2,5-bis(dodecyloxy)benzene (**6**). Note peaks at 0.1, 1.6 and 3.4 ppm, respectively, due to grease, water and methanol impurities.

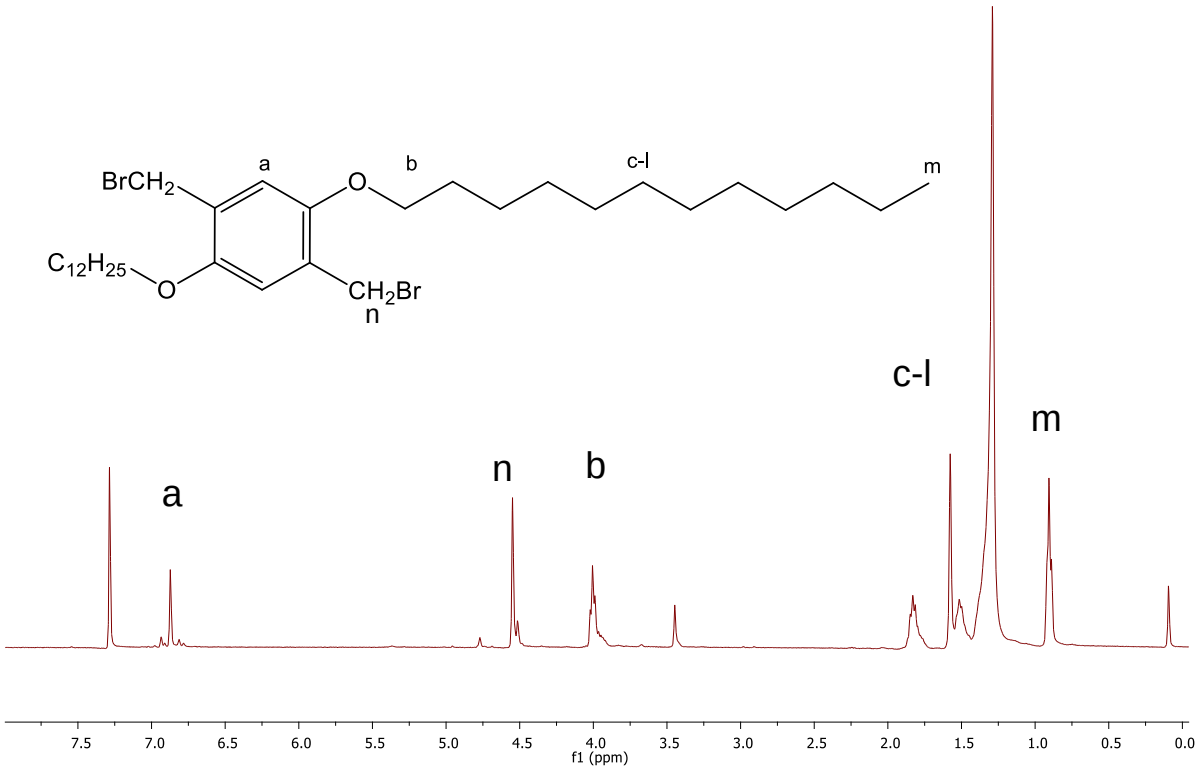

Synthesis of 1,4-bis(bromomethyl)-2,5-bis(hexadecyloxy)benzene (7)

1,4-bis(hexadecyloxy)benzene (5.0 g, 0.009 mol) and the paraformaldehyde (0.67 g, 0.02 mol) were stirred with acetic acid (150 mL) under nitrogen. HBr 31 % in acetic acid (5.7 mL, 0.03 mol) was added dropwise and the reaction warmed to 70 °C for 2 h. Once cooled to room temperature, the solution was quenched with 300 mL of water and the product recovered by filtration. Purification was performed by twice dissolving the product into chloroform and precipitating it from methanol to yield a brownish material (3.2 g, 48 %).

^{1}H NMR (400 MHz, ambient temperature, $CDCl_3$): δ 6.84 (s, 2H, -*aromatic*), 4.56 (s, 4H, -C*H*$_2$Br), 3.93 (t, *J* = 6 Hz, 4H, -O-C*H*$_2$), 1.87 (q, *J* = 6 Hz, 4H, -C*H*$_2$-), 1.78 (q, *J* = 6 Hz, 4H, -C*H*$_2$-), 1.51–1.22 (m, 56H, -C*H*$_2$-), 0.91 (t, *J* = 6 Hz, 6H, -C*H*$_3$).

Figure 32: ^{1}H NMR (400 MHz, $CDCl_3$, room temperature) of 1,4-bis(bromomethyl)-2,5-bis(hexadecyloxy)benzene (**7**). Note peaks at 0.1 and 1.6, respectively, due to grease and water impurities.

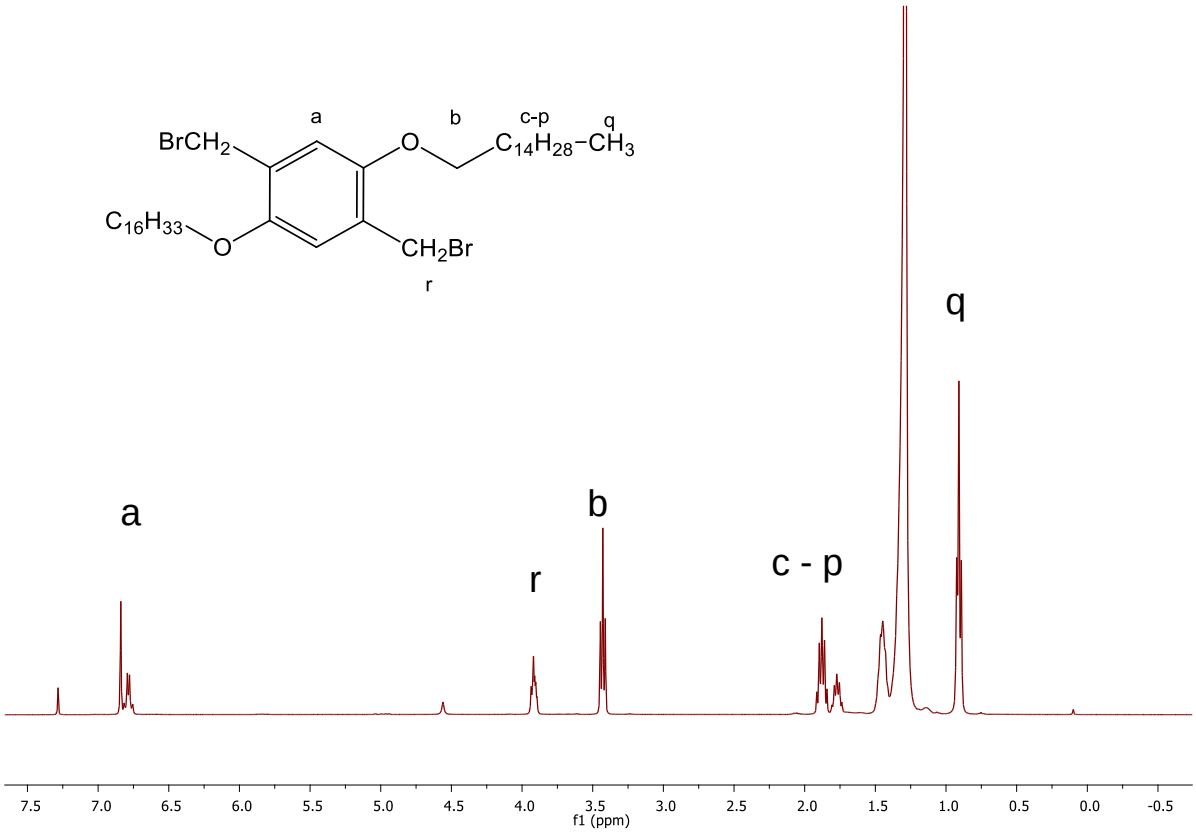

Synthesis of 1,4-bis(azidomethyl)-2,5-bis(octyloxy)benzene (8)

4-Bis(bromomethyl)-2,5-bis(octyloxy)benzene (**5**, 3 g, 5.76 x 10^{-3} mol) and sodium azide (1.11 g, 0.017 mol) were stirred with dimethyl sulfoxide (40 mL) under nitrogen for 12 h. The solution was dropped into iced water (150 mL), and the product recovered with diethyl ether (100 mL). Purification was performed by twice washing the solution with brine and recovering with diethyl ether. Drying over $MgSO_4$, roto-evaporation of the solvent, filtration and drying under air yielded white crystals (1.72 g, 67 %).

^{1}H NMR (400.6 MHz, $CDCl_3$) δ = 0.91 (t, 6H -$OCH_2(CH_2)_6CH_3$), 1.32-1.85 (m, 24H, -$OCH_2(CH_2)_6CH_3$), 4.01 (t, 4H, -$OCH_2(CH_2)_6CH_3$), 4.45 (s, 4H, -CH_2N_3), 6.87 (s, 4H, aromatics) ppm.

^{13}C NMR (100.16 MHz, $CDCl_3$) δ = 14.34 (s, O-$CH_2(CH_2)_6CH_3$), 22.70 (s, O-$CH_2(CH_2)_5CH_2CH_3$), 26.08 (s, O-$CH_2CH_2CH_2(CH_2)_4CH_3$), 29.23 - 29.33 (m, O-$CH_2(CH_2)_6CH_3$), 31.74 (s, O-$CH_2(CH_2)_4CH_2CH_2CH_3$), 49.81 (-CH_2-N_3), 68.93 (s, O-$CH_2(CH_2)_6CH_3$), 113.74 (s, aromatic), 124.88 (s, *aromatic*-CH_2N_3), 150.56 (s, *aromatic*-OC_8H_{17}) ppm.

Figure 33: ^{1}H NMR (400 MHz, $CDCl_3$, room temperature) of 1,4-bis(azidomethyl)-2,5-bis(octyloxy)benzene (**8**). Note peaks at 1.57 and 3.51 ppm, respectively, due to water and methanol impurities, and at 0.1 ppm due to grease.

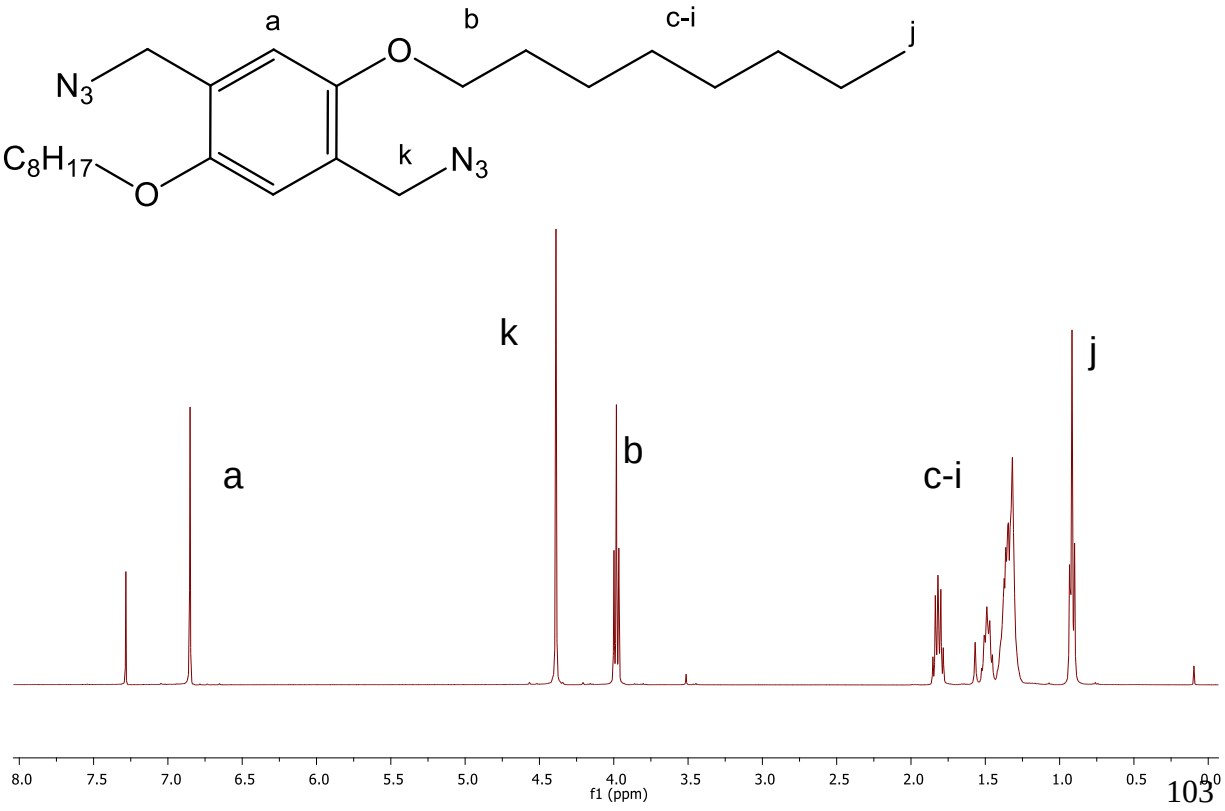

Figure 34: ^{13}C NMR (100.16 MHz, $CDCl_3$, room temperature) of 1,4-bis(azidomethyl)-2,5-bis(octyloxy)benzene (**8**).

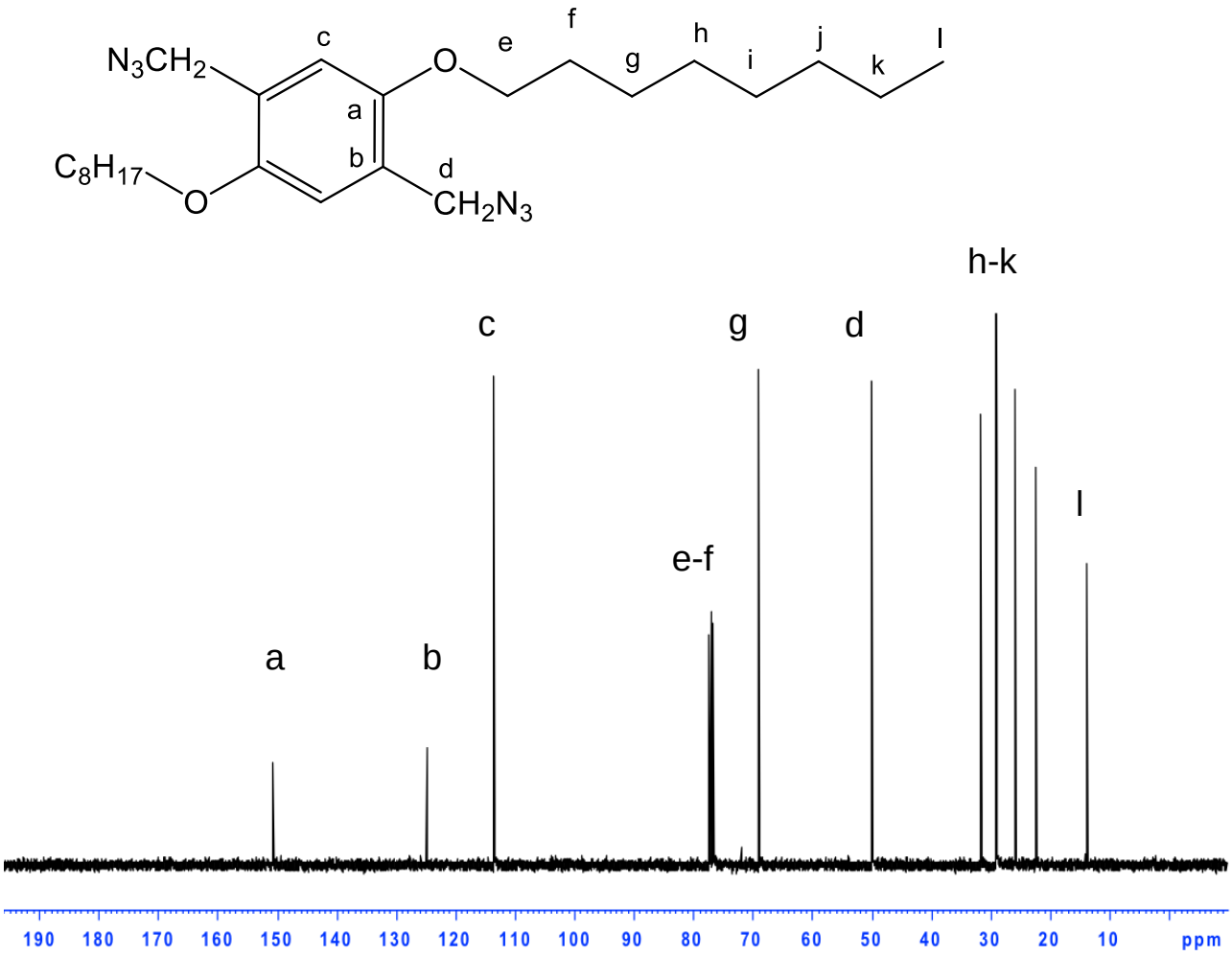

Synthesis of 1,4-bis(azidomethyl)-2,5-bis(dodecyloxy)benzene (9)

1,4-Bis(bromomethyl)-2,5-bis(dodecyloxy)benzene (3 g, 4.74 x 10^{-3} mol) and sodium azide (0.31 g, 0.014 mol) were stirred with dimethyl sulfoxide (40 mL) under nitrogen for 12 h. The solution was dropped into iced water (150 mL), and the product recovered with diethyl ether. Purification was performed by twice dissolving the product in brine and recovering with diethyl ether and dried over $MgSO_4$ to a yield a white material (2.3 g, 68 %).

^{1}H NMR (400 MHz, $CDCl_3$) δ 6.85 (s, 2H, -*aromatic*), 4.39 (s, 4H, -C*H*$_2$-N_3), 1.82 (t, *J* = 6 Hz, 4H, -C*H*$_2$-), 1.63 (m, 40H, -C*H*$_2$-), 0.91 (t, *J* = 6 Hz, 6H, -C*H*$_3$).

^{13}C NMR (100.16 MHz, $CDCl_3$) δ = 14.11 (s, O-$CH_2(CH_2)_{10}$*C*H_3, 22.69 (s, O-$CH_2(CH_2)_9$*C*H_2CH_3), 26.08 (s, O-CH_2CH_2*C*$H_2(CH_2)_8CH_3$), 29.38 (s, O-CH_2CH_2*C*H_2*C*$H_2(CH_2)_7CH_3$), 49.95 (s, -*C*H_2-N_3), 68.91 (s, , O-CH_2CH_2*C*H_2*C*H_2*C*$H_2(CH_2)_6CH_3$), 76.70 - 77.34 (m, O-*C*$H_2(CH_2)_{10}CH_3$), 113.46 (s, aromatic), 124.18 (s, *aromatic*-CH_2N_3), 150.64 (s, *aromatic*-$OC_{12}H_{25}$) ppm.

Figure 35: ^{1}H NMR (400 MHz, $CDCl_3$, room temperature) of 1,4-bis(azidomethyl)-2,5-bis(dodecyloxy)benzene (**9**). Note peak at 2.6 ppm due to dimethyl sulfoxide.

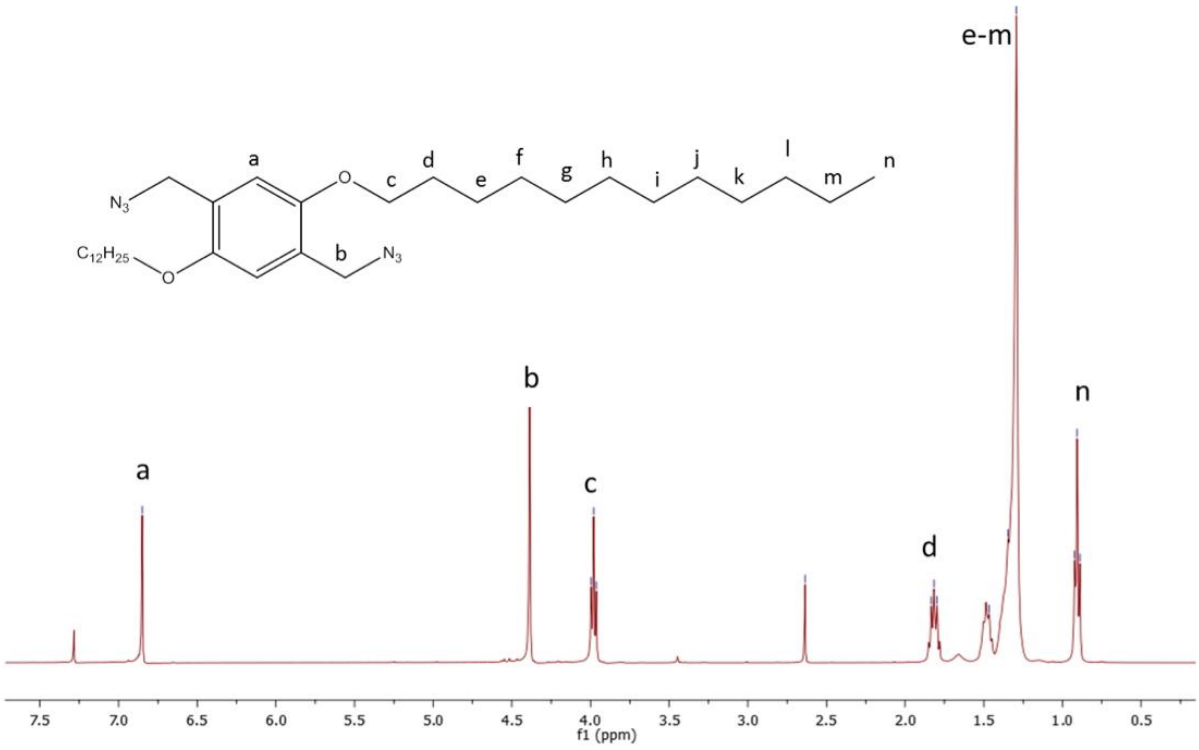

Figure 36: ^{13}C NMR (100.16 MHz, $CDCl_3$, room temperature) of 1,4-bis(azidomethyl)-2,5-bis(dodecyloxy)benzene (**9**).

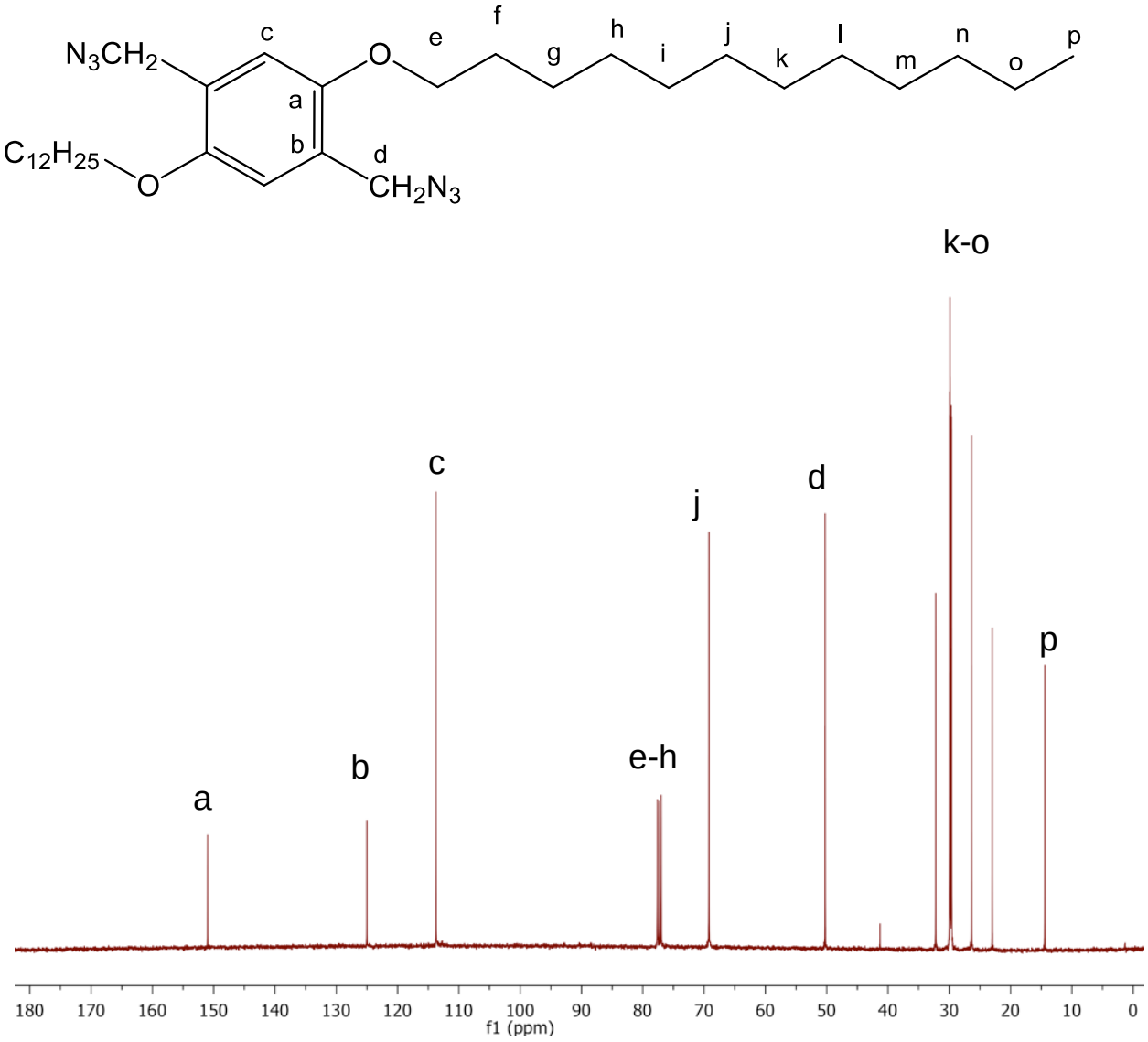

Synthesis of 1,4-bis(azidomethyl)-2,5-bis(hexadecyloxy)benzene (10)

1,4-Bis(bromomethyl)-2,5-bis(hexadecyloxy)benzene (3 g, 4.03 x 10^{-3} mol) and sodium azide (0.78 g, 0.012 mol) were stirred with dimethyl sulfoxide (120 mL) under nitrogen for 12 h. The solution was dropped into iced water (150 mL), and the product recovered with diethyl ether (100 mL). Purification was performed by twice washing the product with brine, recovering with diethyl ether, drying over $MgSO_4$ and then evaporation of the solvents under air. The yield of a creamy-white powder (1.4 g, 52 %).

^{1}H NMR (400 MHz, $CDCl_3$) δ 4.55 (s, 2H, -*aromatic*), 4.00 (s, 4H, -C*H*$_2$-N_3), 1.82 (t, *J* = 6 Hz, 4H, -C*H*$_2$-), 1.30 (m, 56H, -C*H*$_2$-), 0.91 (t, *J* = 6 Hz, 6H, -C*H*$_3$).

Figure 37: ^{1}H NMR (400 MHz, $CDCl_3$, room temperature) of 11,4-bis(azidomethyl)-2,5-bis(hexadecyloxy)benzene (**10**) Note plenty of impurities peaks.

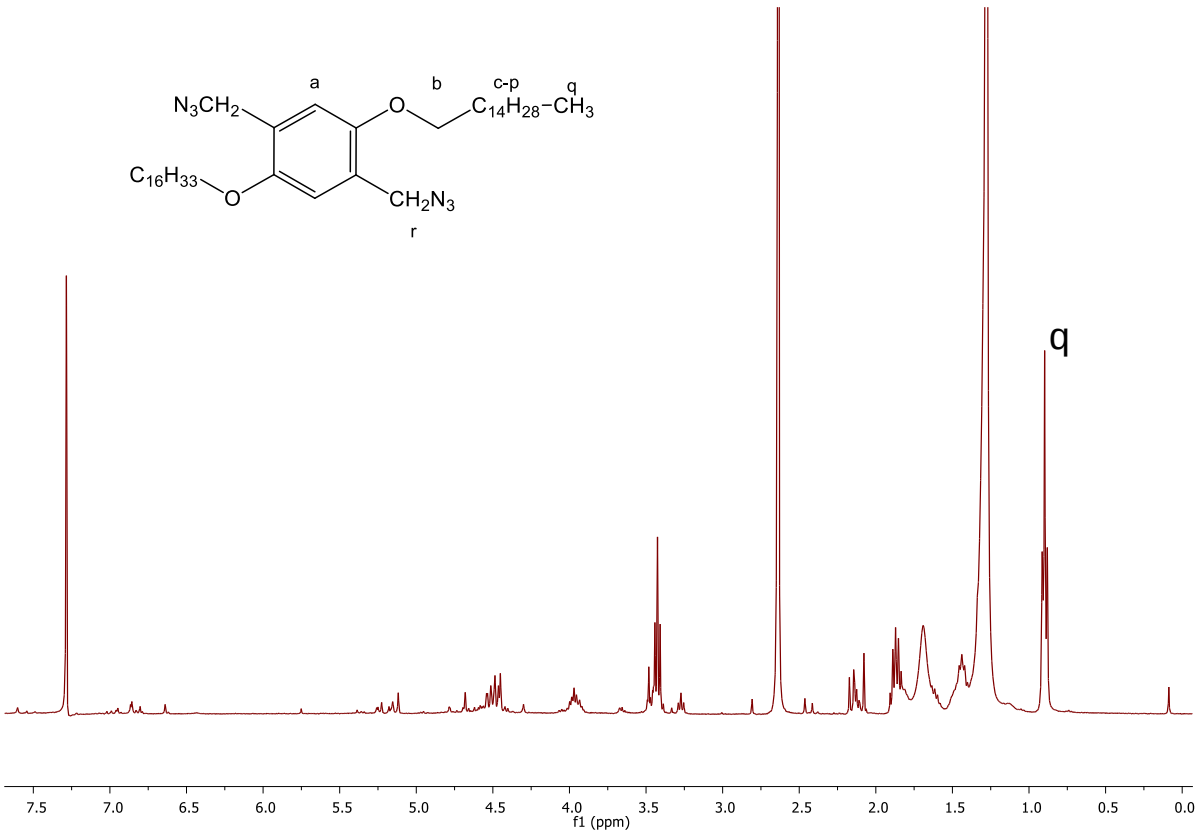

CHAPTER 4

INORGANIC OXIDE SYNTHESIS

In this chapter will be described the synthesis of TiO_2 and derivatives as titanates, in different conditions, acidic and alkaline, using the microwave assisted hydrothermal technique. It was investigated the influence of the temperature and synthetic time in both systems. Also, in the alkaline environement it was explored three concentrations of sodium ions.

Table 7: Morphology, surface area and yield of the synthesized samples. They are named as: a prefix (HM for acidic media or HMB for alkaline media), followed by the temperature, time of treatment and concentration of NaOH for the alkaline media.

Sample	Morphology	Surface area (m^2/g)	Yield (%)
HM110-15	Nanospheres	372	26
HM110-30	Nanospheres	-	52
HM110-60	Nanospheres	-	67
HM130-15	Nanospheres	382	54
HM130-30	Nanospheres	-	83
HM130-60	Nanospheres	427	89
HM150-2	Nanospheres	-	18
HM150-5	Nanospheres	-	26
HM150-15	Nanospheres	-	84
HM150-30	Nanospheres	207	93
HM150-60	Nanospheres	-	95
HMB150-30-0.1	Nanospheres	-	90
HMB110-5-1	Nanospheres+nanosheets	-	71
HMB110-15-1	Nanospheres+nanosheets	-	79
HMB110-30-1	Nanospheres+nanosheets	-	98
HMB110-60-1	Nanospheres+nanosheets	-	95
HMB130-5-1	Nanosheets+nanocables	-	65
HMB130-15-1	Nanosheets+nanocables	-	73
HMB130-30-1	Nanosheets+nanocables	-	96
HMB130-60-1	Nanosheets+nanocables	-	96
HMB150-5-1	needle-like + nanosheets	-	65
HMB150-15-1	needle-like + nanosheets	-	80

HMB150-30-1	needle-like + nanospheres	-	95
HMB150-60-1	needle-like + nanosheets	-	98
HMB110-5-10	needle-like + nanosheets	-	73
HMB110-15-10	needle-like + nanosheets	-	78
HMB110-30-10	needle-like + nanosheets	-	94
HMB110-60-10	needle-like + nanosheets	-	96
HMB130-5-10	needle-like + nanosheets	-	72
HMB130-15-10	needle-like + nanosheets	-	81
HMB130-30-10	needle-like + nanosheets	-	97
HMB130-60-10	needle-like + nanosheets	-	97
HMB150-5-10	needle-like + nanosheets	-	72
HMB150-15-10	needle-like + nanosheets	-	85
HMB150-30-10	needle-like	375	98
HMB150-60-10	needle-like	-	96

Acidic media

As already presented in Table 7, the synthesis in acidic media was performed at different temperatures; 110, 130 and 150 °C for 2, 15, 30 and 60 min. The temperatures were chosen above the boiling point of water to reach the solvent vapor pressure saturation. The solution volume used in the autoclave with maximum of 100 mL was fixed at 40 mL. The pressure of the system was not externally controlled and reached a maximum of 1 MPa.

Figure 38 shows the XRD patterns of samples synthesized. The diffractogram exhibits the same trends for all the samples in the acidic media: predominance of the anatase phase (JCPDS 21-1272), with a peak at $2\theta = 31.8°$ is attributed to the (211) plane of the brookite phase (JCPDS 29-1360).

Figure 38: XRD Patterns for all the samples synthesized in acidic media in a) HM150-XX, b) HM130-XX and c) HM110-XX-10.

a)

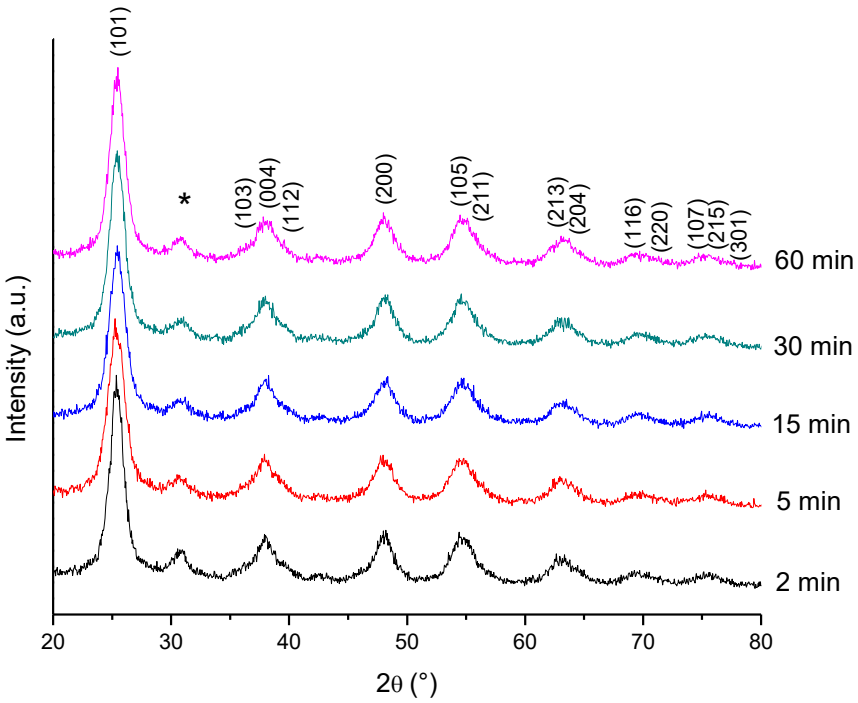

b)

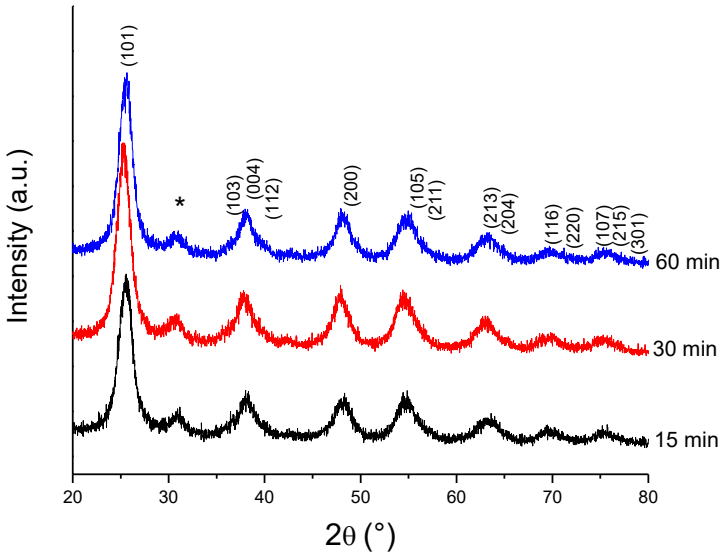

c)

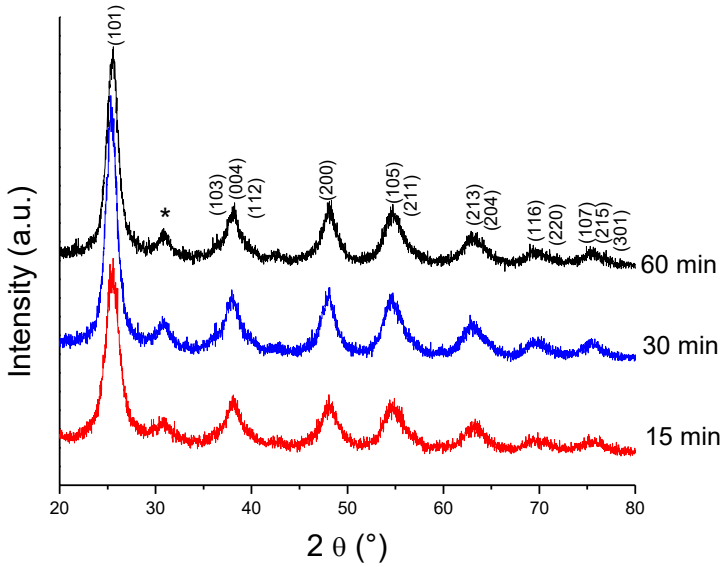

The intensity of the diffraction peak is correlated to the volume of the phase and crystallite size. In very small crystallites, the peaks are broad as observed in Figure 38. Crystallites sizes are close to 6.0 nm for all materials analyzed as presented in the Table 8.

Table 8: Calculated crystallite size.

Sample	FWHM (°)	Peak Position (°)	Crystallite size (nm)
HM110-15	1.70	25.7	5.75
HM110-30	1.24	25.4	6.86
HM110-60	1.50	25.6	5.68
HM130-15	1.63	25.7	5.22
HM130-30	1.60	25.4	5.32
HM130-60	1.60	25.4	5.32
HM150-2	1.29	25.4	6.60
HM150-5	1.90	25.3	4.48
HM150-15	1.56	25.4	5.45
HM150-30	1.45	25.4	5.87
HM150-60	1.45	25.4	5.87

No clear dependence on the particle size or its morphology was observed on the synthesis parameters used. As can be seen in Figure 39, it is possible to observe from SEM images that the particles are agglomerated. The particle aggregation is expected due to the existence of an amorphous phase related to $Ti(OH)_n$ species, once the nanoparticles has not been submitted to the sintering process after the synthesis.

Figure 39: SEM images of samples prepared at a) HM110-15 b) HM150-60 c) HM130-15, d) HM130-30, e) HM150-2 and f) HM150-60

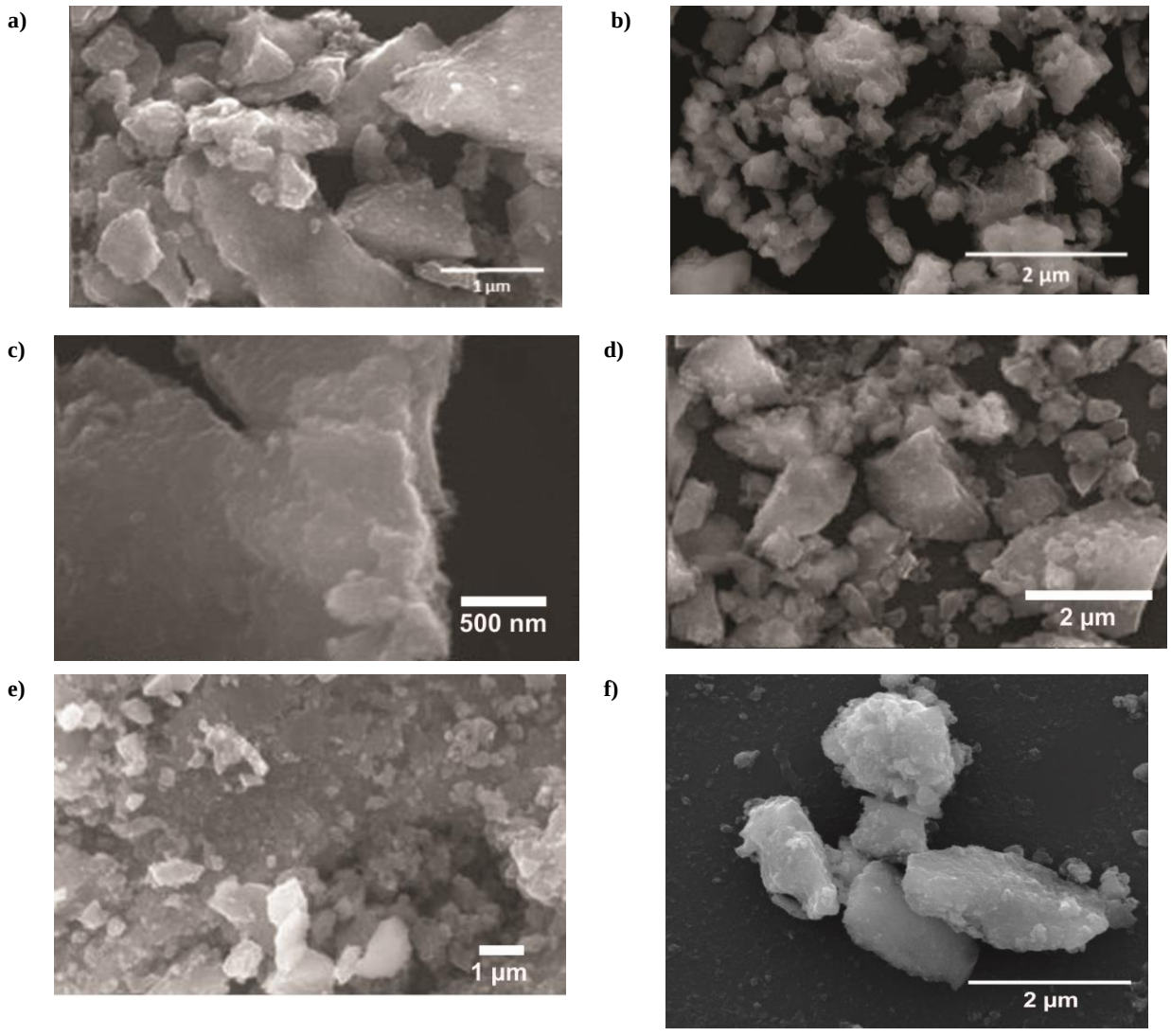

On the order hand, analyzing the TEM images, Figure 40a and 40b, it is possible to observe that the nanoparticles have sizes between 5 and 15 nm for HM150-30. Electron Diffraction

Pattern in Figure 40c shows, in accordance with X-ray diffraction, that the samples are crystalline. The surface area for the same sample was 207 $m^2 g^{-1}$, calculated by BET. Adsorption curve shown in Figure 40d is typical of micro-porous material with relatively small external surface (SING, 1985).

In summary, the synthesis parameter used did not affect the morphology, crystallite size and crystalline phase of the materials obtained. However, they did influence the synthesis yield. For short times, 2 and 5 minutes, the yield was lower than 30 % even at the highest temperature. Whereas the synthesis yields at 150 °C and 30 min was 93 %. For the yield determination, each reaction was repeated at least 3 times and the yields presented are an average value.

Figure 40: TEM images obtained with different magnifications (a) and (b), Electron Diffraction Pattern (c) and BET adsorption curve (d) for sample HM150-30

a)

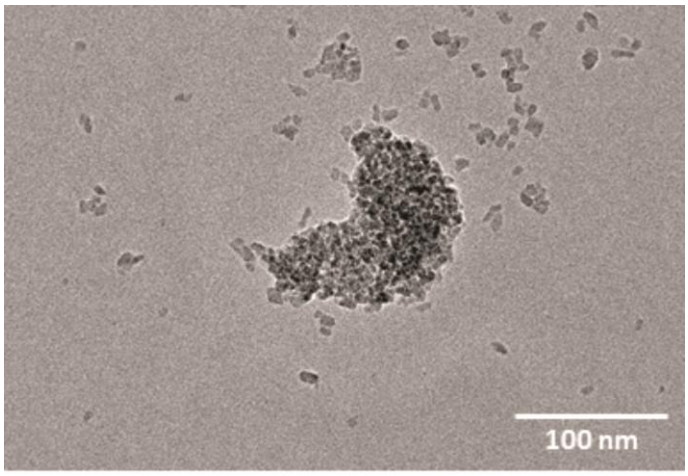

b)


b)
(112)
0.233nm
10 nm

c)

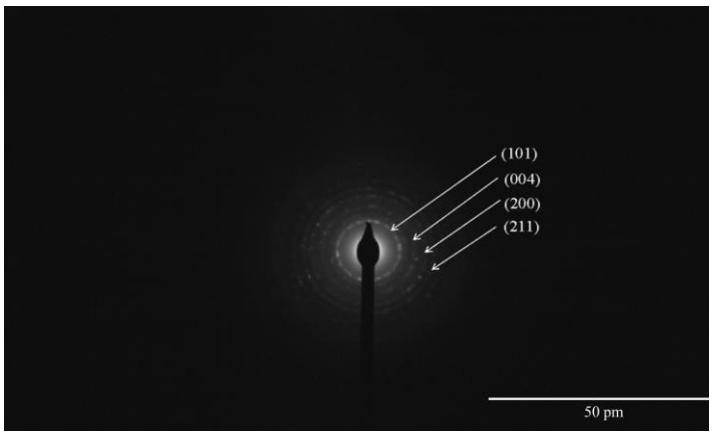
(101)
(004)
(200)
(211)
50 pm

d)

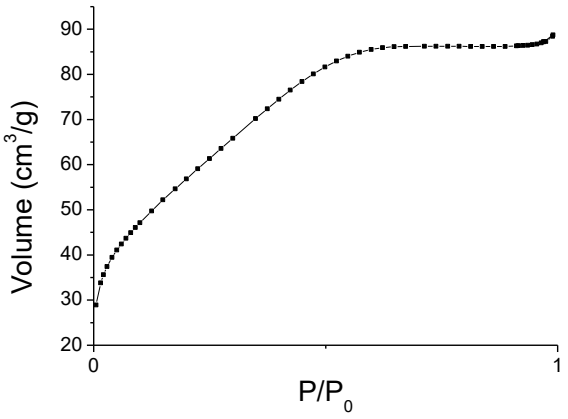
Volume (cm3/g)
90
80
70
60
50
40
30
20
0
1
P/P0

Alkaline media

Similarly, the syntheses under alkaline conditions were performed in different conditions. The temperature was 110, 130 and 150 °C, using 5, 15, 30 and 60 min of treatment for the concentration of 1 and 10 M

We shall start with the effect of the synthesis time in the 1M precursor solution. The XRD patterns for these samples are presented in Figure 41. The diffraction patterns are similar for all the synthetic conditions. They have shown a preferred orientation in the direction of the peak at 2θ = 48.1 ° which can be attributed to $Na_2Ti_6O_{13}$ (JCPDS 73-1398) (ANDERSSON, 1962). Analogous to the acidic system, the synthesis time did not influence the crystalline phase and morphology. However, the time did influence the yield of the synthesis and the optimum yield, > 90 %, was obtained after 30 min of synthesis, as presented in Table 7.

Figure 41: XRD patterns for the samples a) HMB110-XX-1, b) HMB130-XX-1 and c) HMB150-XX-1.

a)

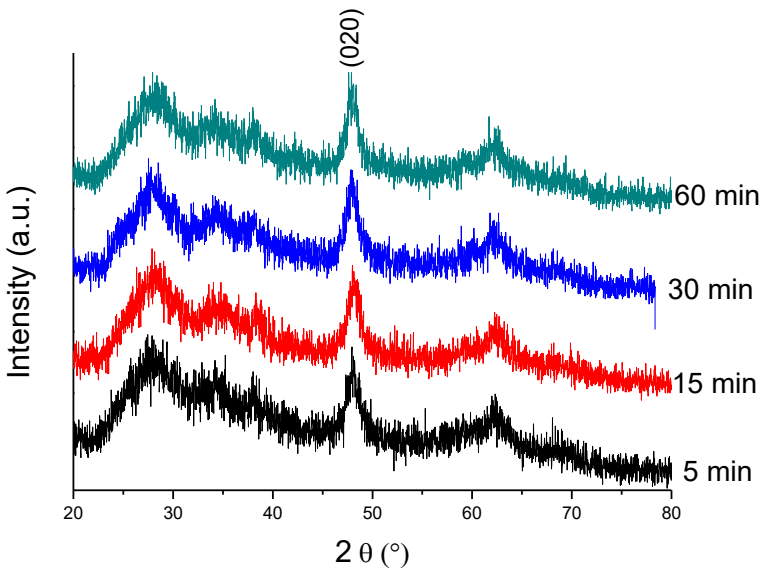

b)

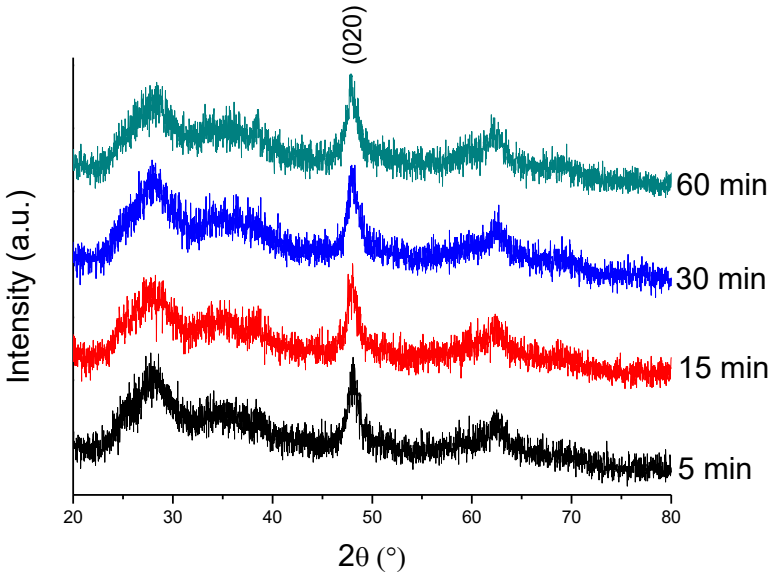

c)

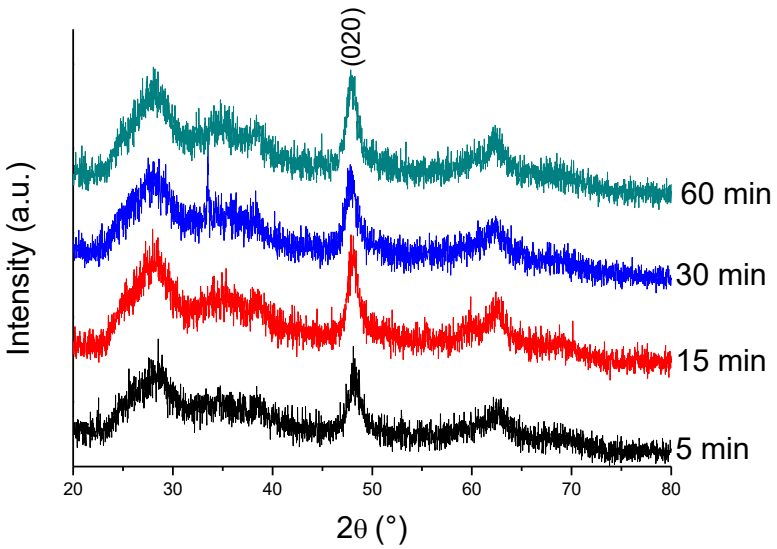

The SEM image of the samples synthesized at 110 °C present sphere-like aggregated that are composed by nanosheets, observed in higher magnifications, Figures 42a and 42b. The samples synthesized at 130 °C presented a mixture of nanocables and nanoparticles, and the same trend of nanosheets observed in lower temperature of treatment, Figures 42c, 42d and 42e. The sample synthesized at 150 °C present a mixture of needle like structures and irregular spheres as observed in lower concentrations of NaOH, Figure 42f. It is important to note that the same trend of morphologies was observed in the various temperatures, however, the samples

treated at 5 min, presented the most heterogeneous and bigger nanoparticles, Figure 42g and 42h.

Figure 42: SEM image for a) HMB110-30-1, b) HMB110-30-1 (higher magnification), c) HMB130-30-1 (lower magnification), d) HMB130-30-1 (higher magnification 1), e) HMB130-30-1 (higher magnification 2), f) HMB150-30-1, g) HMB110-5-1 and h) HMB150-15-1.

a) HMB110-30-1

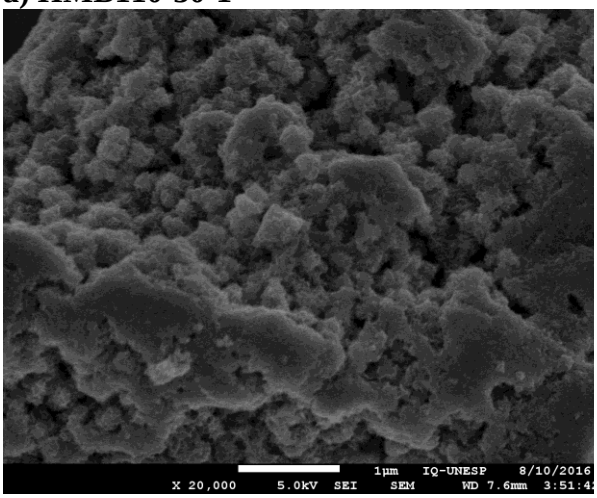

b) HMB110-30-1 (higher magnification)

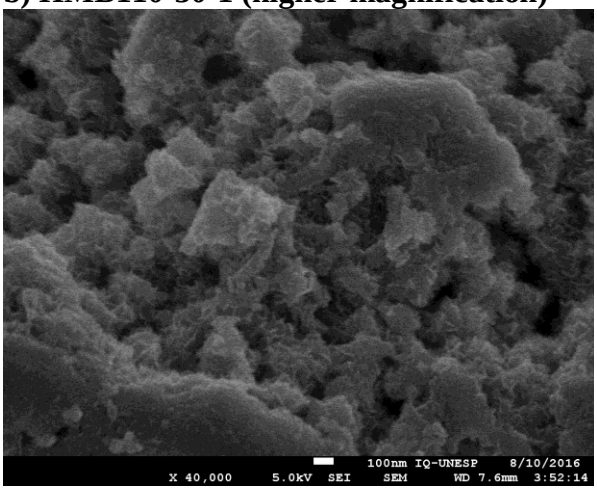

c) HMB130-30-1 (lower magnification)

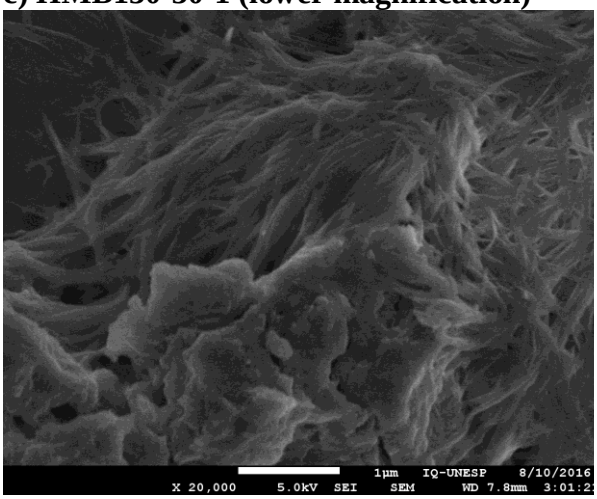

d) HMB130-30-1 (higher magnification 1)

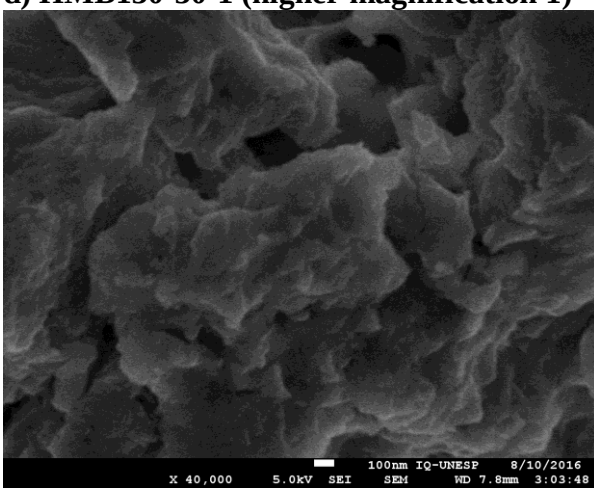

e) HMB130-30-1 (higher magnification 2)

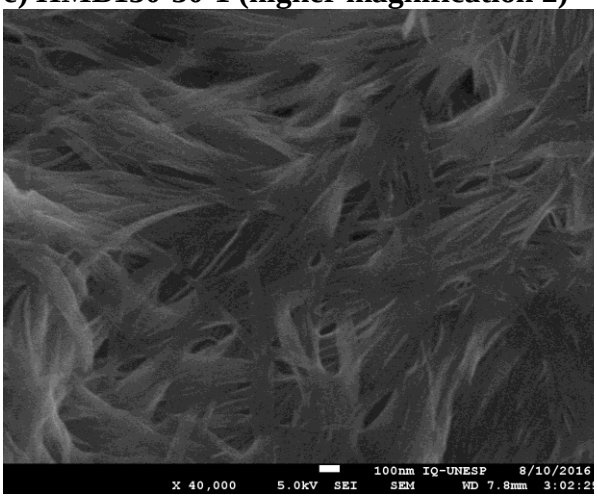

f) HMB150-30-1 higher magnification

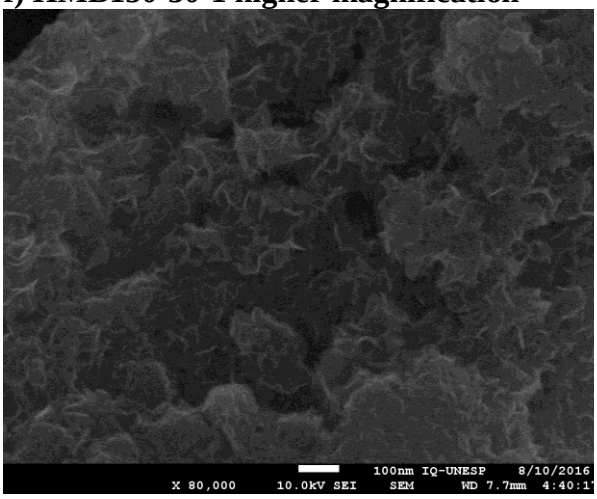

g) HMB110-5-1

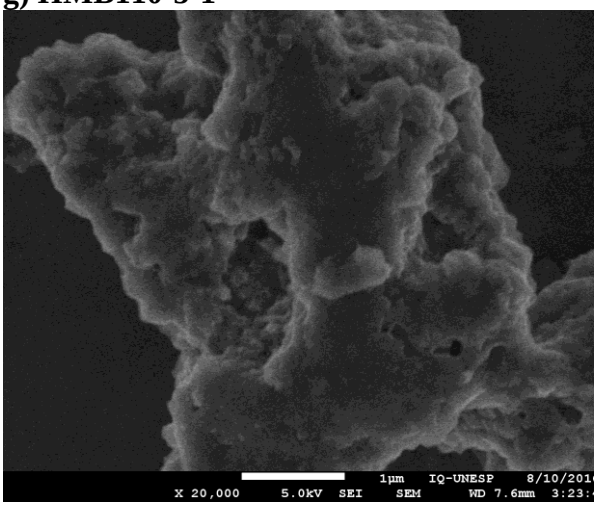

h) HMB150-15-1

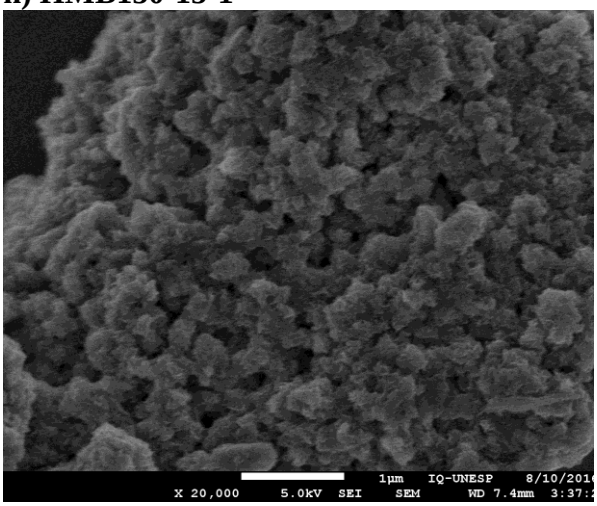

In the 10 M precursor solutions, the same trend for XRD patterns were obtained in all synthetic conditions used, as shown in Figure 43. It was also obtained titanates, in this case $Na_2Ti_3O_7$ (JCPDS 31-1329).

Figure 43: XRD patterns for the samples a) HMB110-XX-10, HMB130-XX-10 and HMB150-XX-10.

a)

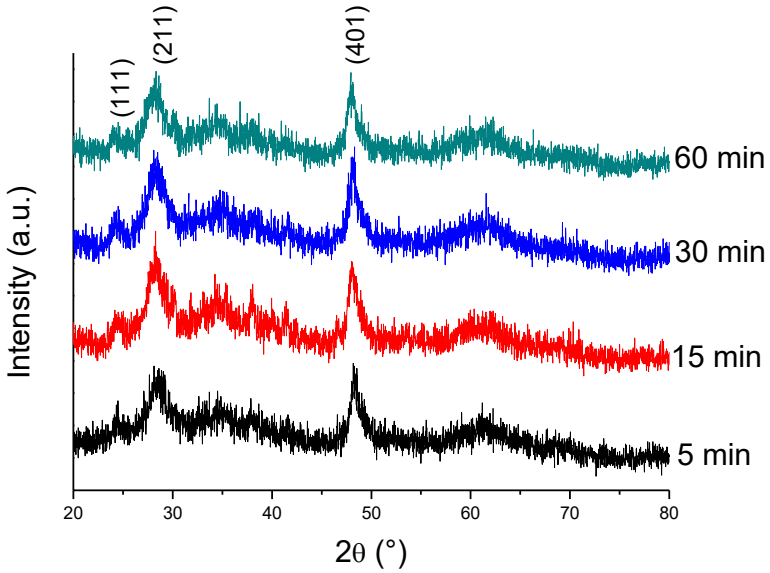

b)

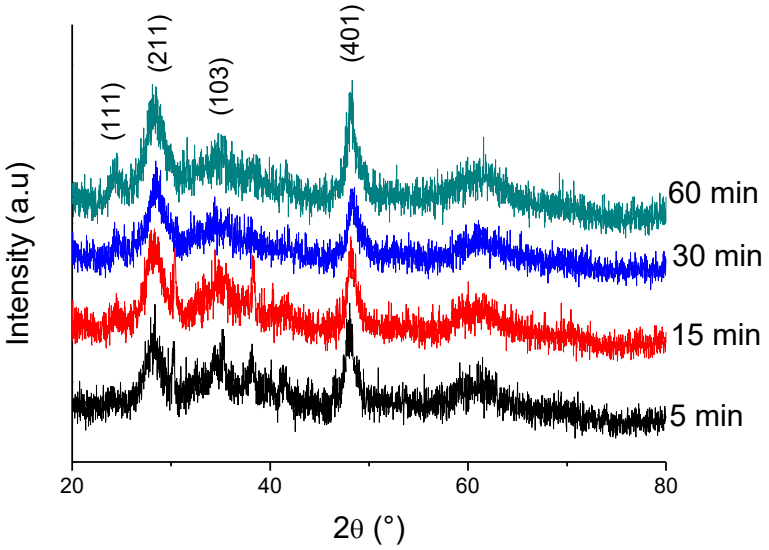

c)

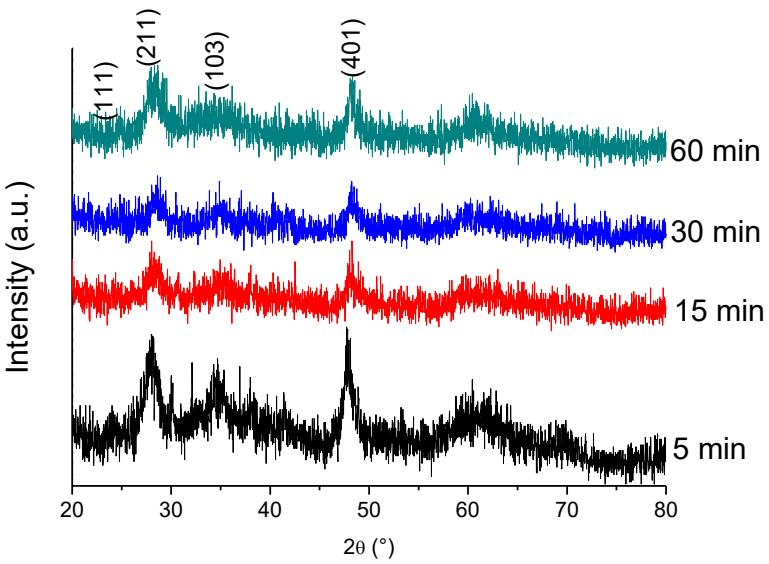

The influence of the Na^+ in the crystal growth was addressed using different NaOH concentrations during the synthesis. In Figure 44, XRD patterns for the solutions prepared using 10 M (HMB150-30-10) and 0.1 M (HMB150-30-0.1) are compared. It can be seen that the sample with the highest concentration of NaOH exhibits a pattern of Titanate, as presented above, while the lower concentration shows the anatase phase, similarly to Figure 38. Notice that even the peak of the brookite phase in $2\theta = 31°$ is observed for HMB150-30-0.1.

Figure 44: XRD patterns for the samples HMB150-30-10 and HMB150-30-0.1.

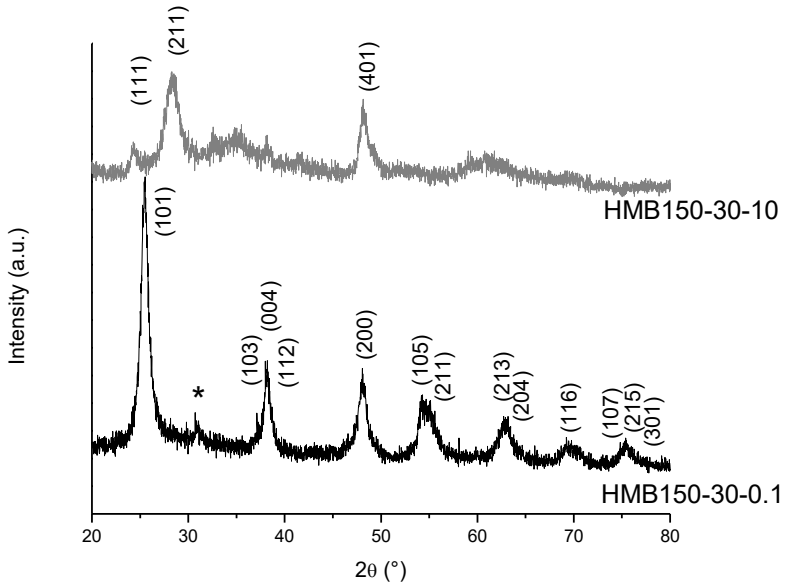

SEM images, Figure 45, show the same trends as observed in the XRD. In other words, the samples with low concentration of NaOH have similar morphology as observed for the synthesis in acidic media and have needle-like structures when using 1 M or 10 M NaOH. For other samples see Figure 46.

Figure 45: SEM images for the samples a) HMB150-30-0.1, b) HMB150-30-10 and c) HMB150-30-10 BET adsorption curve.

a)

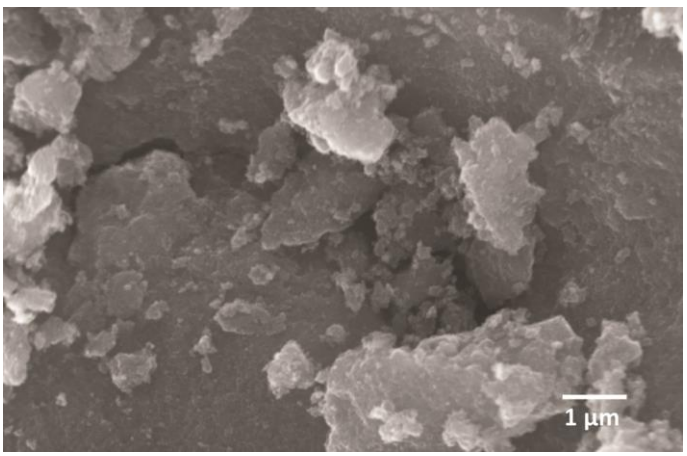

b)

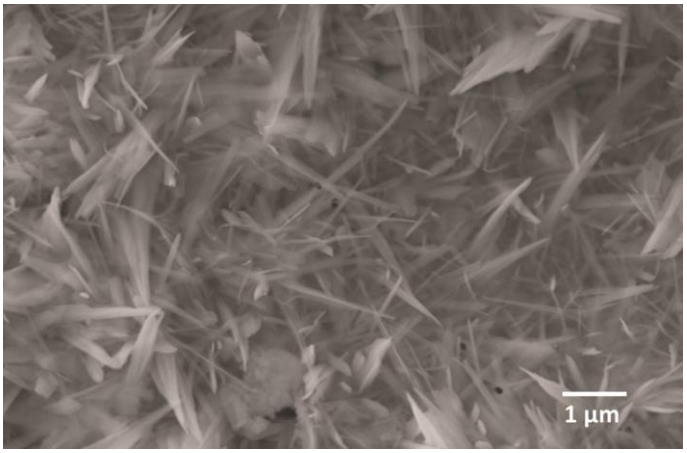

c)

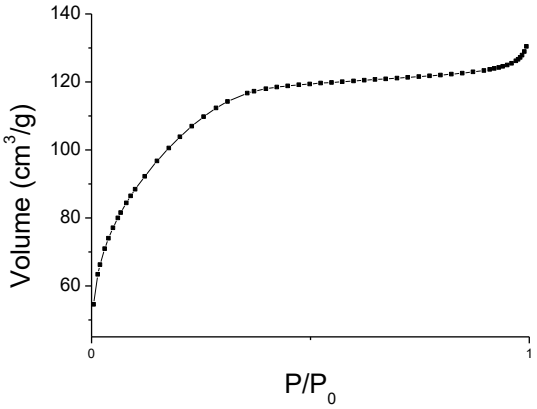

BET adsorption curve, Figure 45c, shows a steep increase in the isotherm, followed by a *plateau* which indicates a micro-porous material with *relatively* small external surface. The plateau is reached as soon as the surface is completely covered (SING, 1985). The surface area for HMB150-30-10 was 375 m^2g^{-1}.

Figure 46: SEM images of the samples obtained in alkaline media in a) HMB150-60-10, b) HMB150-15-1, c) HMB150-30-1, d) HMB150-60-1, e) HMB150-30-0.1 e f) HMB150-30-10.

a) HMB150-60-10

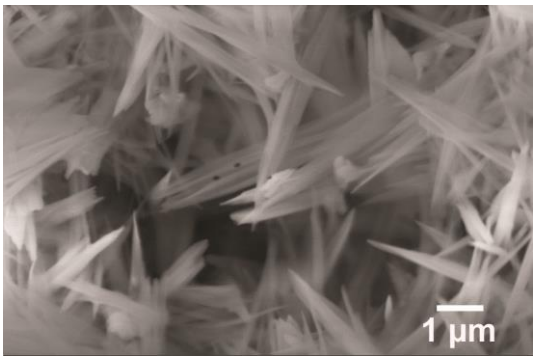

b) HMB150-15-1

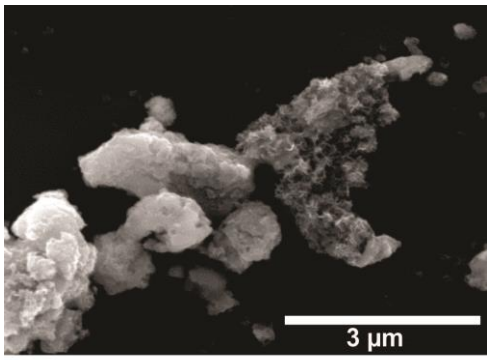

c) HMB150-30-1

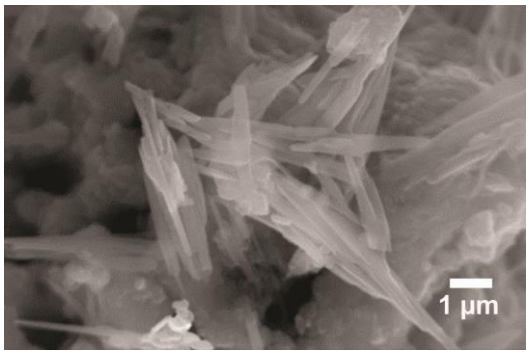

d) HMB150-60-1

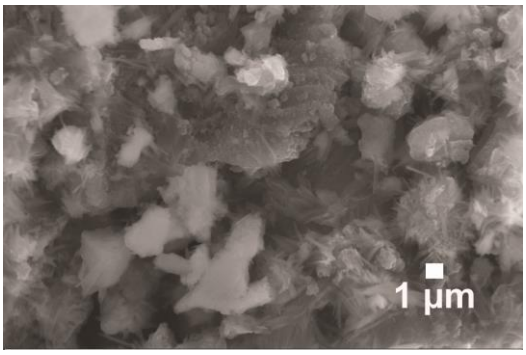

e) HMB150-30-0.1

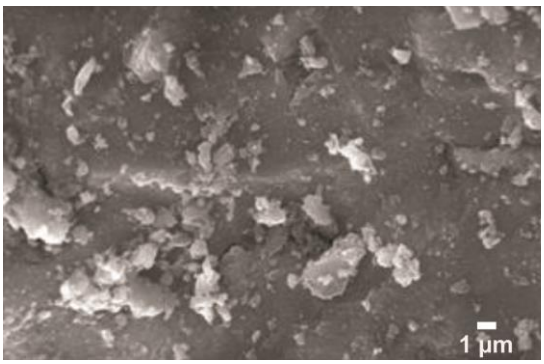

f) HMB150-30-10

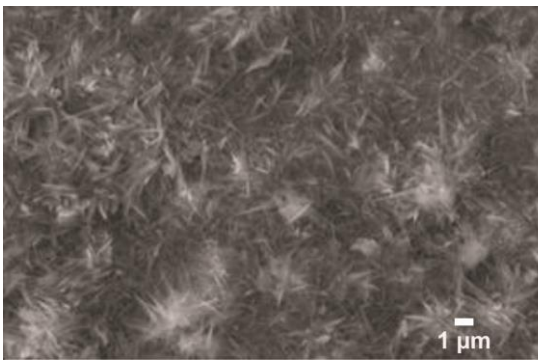

The HCl washing is known to be a fundamental step for the nanotubes formation (KASUGA, 1998). TEM imagens of the washed with HCl sample HMB150-30-10 are shown in Figure 47a. The EDX, shown in Figure 47b and 47c, has a small peak attributed to Na^+ ions, suggesting that most the ions could be removed by the HCl washes.

Figure 47: a) TEM image and b) EDX for the sample HMB150-30-10 as synthetised and c) EDX for the sample HMB150-30-10 after HCl washing.

a)

b)

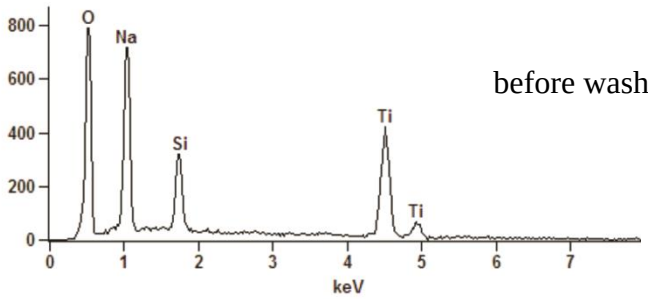

before washing

c)

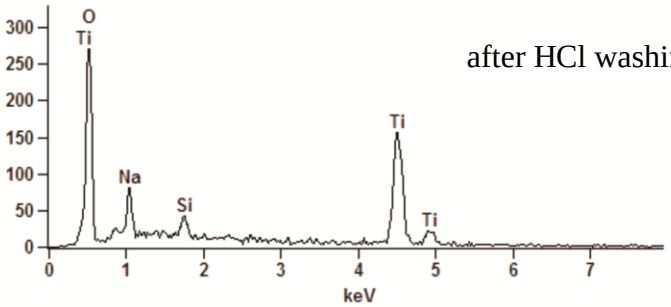

after HCl washing

Discussion

Our results indicate that in the acidic conditions, time and temperature of synthesis did not affect the morphology, crystallite size and crystalline phase. However, the synthetic conditions did influence the yield of nanoparticles. The best yields were obtained for synthesis from 30 to 60 min at 150 °C. In order to understand the different yields and the small dependence of synthesis parameters on the nanoparticles, we shall start discussing the mechanism of nanoparticles formation. The mechanism of TTIP precursor solution formation starts with the loss of the organic groups from TTIP and hydrolysis, which will have led to the formation of $Ti(OH)_x(OCHCH_3)_{4-x}$ species, in the first step of the reaction, as shown at Scheme 12.

Scheme 12: TiO_2 formation mechanism.

a) TTIP hydrolysis

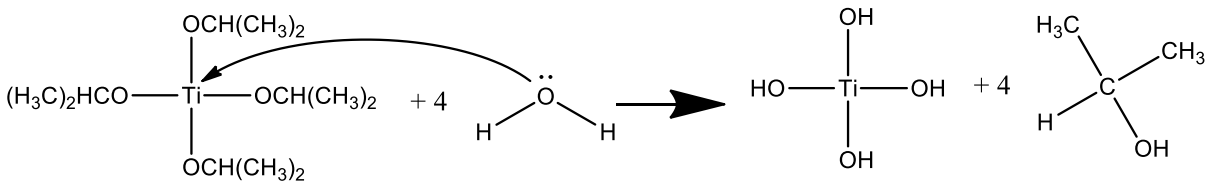

b) Polycondensation of hydrolyzed titanium hydroxide

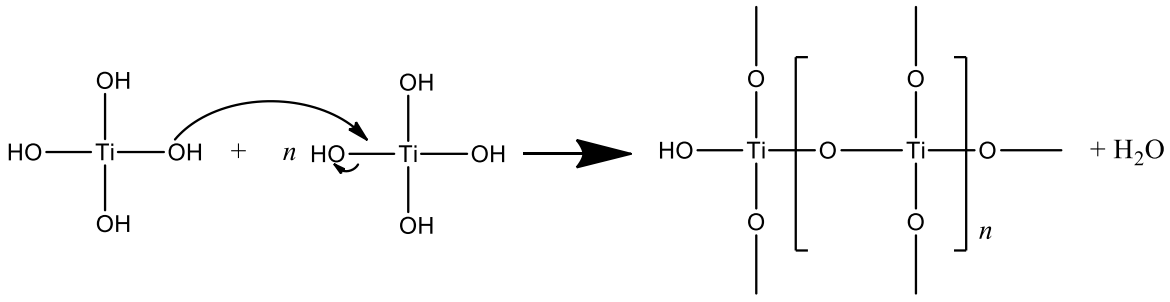

In the second step, in the acid system, the addition of HNO_3 will act as a peptizing agent forming crystallites by hydrolysis with low crystallinity (ISMAIL, 2011). In aqueous media,

protonated surfaces of TiO_6 octahedra easily combine with hydroxyl groups of other TiO_6 octahedra to form Ti–O–Ti oxygen bridged bonds by elimination of water (JIANG, 2006), resulting in an amorphous nanoparticles (BRINKER, 1988; YIN, 2001). The use of microwave hydrothermal processing of colloidal TiO_2 solutions allows rapid heating, fast kinetics of crystallization and formation of a large number of clusters that grows fast from the amorphous nanoparticles and assemble into TiO_2 nanocrystallite aggregates (WILSON, 2002). This mechanism is characterized by the formation of a high concentration of aggregated nanoparticles. Additionally, it is known that particle size influences the crystalline phase. Wherein, anatase is the most stable for particles smaller than 11 nm, brookite for particles between 11 and 35 nm and rutile for particles bigger than 35 nm (ZHANG, H., 2000). In this way, our results indicate that the fast cluster formation, due to the microwave heating, is responsible for the small crystallite and nanoparticles obtained and its aggregation. Finally, the crystalline materials exhibit the predominance of anatase phase with some brookite phase nanoparticles formed due the pressures inside the autoclave. Normally the simplest way to control the crystal size is by microwave synthesis time. However, in our results there is not clear difference in the nanoparticles size depending on time. The crystal growth mechanism observed is compatible to an oriented aggregation of small primary subunits (LUO, 2012). We observed the highest yields for the highest temperature and times higher than 30 min. Thus, it is assumed that in this system, 30 min is the minimum synthesis time for the nucleation and growth of the nanoparticles. For times higher than 30 min no difference in yield is observed which can be attributed to the Ostwald ripening process, in which the particles re-dissolve after a critical time, thus the yield is basically time independent after a critical synthesis time (WILSON, 2006). In these synthesis conditions it is expected high internal surface areas (CHEN, P., 2013).

For the samples synthesized in alkaline conditions, the temperature used was fixed at 150 °C, based on the best performance in the acidic system. The synthesis time did not also influence the morphology and crystalline phase, only the yield, following the same trend observed for the acidic condition. However, the synthesis in different concentrations of NaOH resulted in nanoparticles with very different morphologies and phases.

From our results the mechanism of TiO_2 formation follows the same route both in acidic and alkaline medium, hydrolysis and polycondensation. The mechanism of TiO_2 formation is weakly affected by the additive, HNO_3 or NaOH when it is close to the neutral condition, *i.e.* 0.01 M HNO_3 and 0.1 M NaOH (ZHAO, 2013). On the other hand, at high concentrations, 1 M and 10 M NaOH, remarkable differences were observed, needle-like structures were synthesized.

In the literature, few works are dedicated to investigate the influence of acidic and alkaline environments on the nanoparticles formation. Zhao *et al.* (ZHAO, 2013) have study the influence of the NaOH and HCl on the formation of nanostructures with different crystalline phase and morphologies using hydrothermal synthesis and tetrabutyl titanate as precursor. They obtained analogous materials as we did, i.e. anatase with brookite for the lowest concentrations of additives, or in conditions closest to neutral. For high NaOH concentrations, they obtained titanate nanoribbons. The difference between our material morphology and theirs can be attributed to the precursor used and synthesis technique. The ability of microwaves to influence the dissolution rate of various precursors (due to different dielectric properties) strongly affects the nucleation and crystallization rates. The organic species undergo chemical reactions that are responsible for supplying the ‘‘monomers’’ for nucleation and growth of the inorganic nanoparticles (BILECKA, 2010). In this way, the mechanism proposed here is based on the most accepted mechanism for nanotubes formation starting from TiO_2 spherical nanoparticles. Ti – O –Ti bonds are broken by NaOH to create an intermediate containing Ti – O – Na and Ti

– OH bonds (LIU, N., 2014), which grows in preferential directions. Instead, in our case TTIP hydrolyses directly on the solutions forming intermediates that have the format of sheets, as observed, due to the interaction of the TiO layers with Na^+ and H^+. The growth generates layered titanate structure with intercalated Na^+ ions (ZHAO, 2013). The Na^+ ions are mostly removed by HCl rinsing (KASUGA, 1998).

Most of the titanate nanotubes synthesis using microwave have TiO_2 nanopowders as precursor, as a consequence, higher temperatures and times are needed (CUI, 2012; LIU, N., 2014; MANFROI, 2014). Wu et al. (WU, X., 2005) synthesized multiwall structured titanate nanotubes from powders at high NaOH concentration (8–12 M) for 90 min. Also, Ou et al. (OU, 2007) obtained nanotubes with surface area of 256 m^2g^{-1} synthesized at 130 °C for 90 min. Here, we have obtained aggregated nanotube-like in 30 min of treatment using TTIP as precursor with greater surface areas, of 375 m^2g^{-1}.

From the point of view of applications, Dar et al. (DAR, 2014) obtained anatase nanostructures ~ 7 nm using microwave solvothermal technique using thiobenzoate complex of titanium as precursor at 200 °C and made from these materials DSSC with efficiencies of 6.5 %. Shen and coworkers, also used TTIP as precursor, and did their synthesis at 220 °C for 30 min. They obtained anatase nanoparticles with ~ 20 nm in diameter and surface area of 152 m^2g^{-1} which used in DSSC obtained efficiency of 7.8 % (SHEN, 2014). Thus, our results indicate that the synthesized nanoparticles present a great potential for application in DSSC.

Conclusion

Nanostructured titanium oxide was successfully synthesized by microwave assisted hydrothermal using different conditions. Nanoparticles were obtained at mild conditions using low temperatures and short synthesis times, as low as 2 minutes. The XRD patterns show that the TiO_2 nanocrystals are predominantly in the anatase phase though the brookite phase is also present. The crystallite sizes in acidic solutions have 5 to 6 nm in diameter that aggregate into particles of 5 to 15 nm. The reaction time and temperature do not change significantly the structure of the material. In the presence of high concentration of NaOH the morphology and phase are changed to titanates nanotubes, obtained after 30 min of synthesis. The structures obtained, that resemble needles, have the crystalline phase of $Na_2Ti_6O_{13}$ and $Na_2Ti_3O_7$. For lower NaOH concentrations aggregated nanoparticles were obtained similar to the ones obtained using HNO_3 as peptizing agent. In both systems, high surface areas were obtained which indicates that these materials are suited for photovoltaics.

CHAPTER 5

HYBRID PARTICLES

In this chapter it will be present the synthesis and characterization of hybrid nanoparticles, core@shell, P3HT@oxide. As oxide, it was used homemade TiO_2 and Nb_2O_5 synthesized by the microwave assisted hydrothermal. It was used as polymer a funcionalized P3HT witth the triethoxysilane group, which is responsible for the anchoring (grafting) onto the oxide.

The nanoparticles were previously characterized according to their crystalline phase by XRD, presented in the Figure 48. The patterns have shown anatase as predominantly phase for the TiO_2 and hexagonal phase for the Nb_2O_5. The TiO_2 nanoparticles are aggregated and have from 10 to 20 nm and surface area of 207 m^2/g and the Nb_2O_5 nanoparticles have aproximatelly 200 nm and surface area of 15 m^2/g determined by BET. As the graft reactions were performed in low temperature, 60 °C, a change in the crystalline phase is not expected. The grafted nanoparticles obtained, namely TiO_2@P3HT and Nb_2O_5@P3HT were characterized by TEM and the images are shown in the Figure 49. According with the TEM images, it is possible to observe a complete and homogeneous polymer shell around the nanoparticle leading to core@shell hybrid Nb_2O_5@P3HT. In the TiO_2@P3HT images, it is also possible to observe an amorphous region around the crystalline nanoparticle. The polymeric layer is formed due the triethoxysilane groups in the end of each polymeric chain are covalently attached to the oxide nanoparticles, as presented on the Scheme 13 resulting in stable particle with unique properties.

Figure 48: XRD pattern for a) TiO_2 and b)Nb_2O_5.

a)

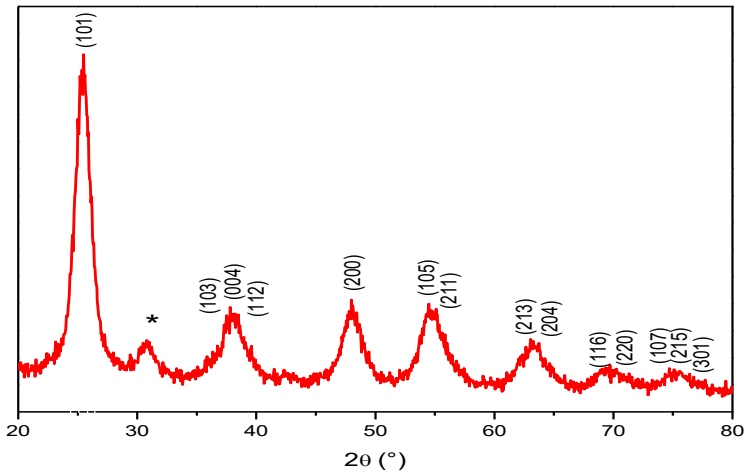

b)

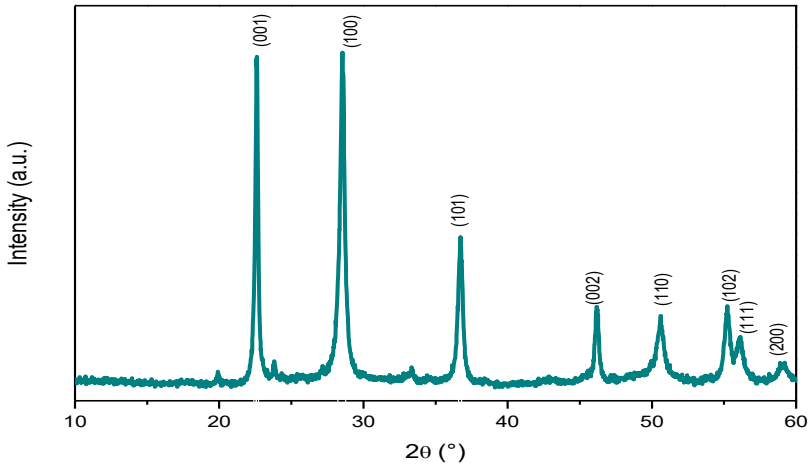

Figure 49: TEM images for the grafted particles a) and b) Nb_2O_5@P3HT and c) and d) TiO_2@P3HT.

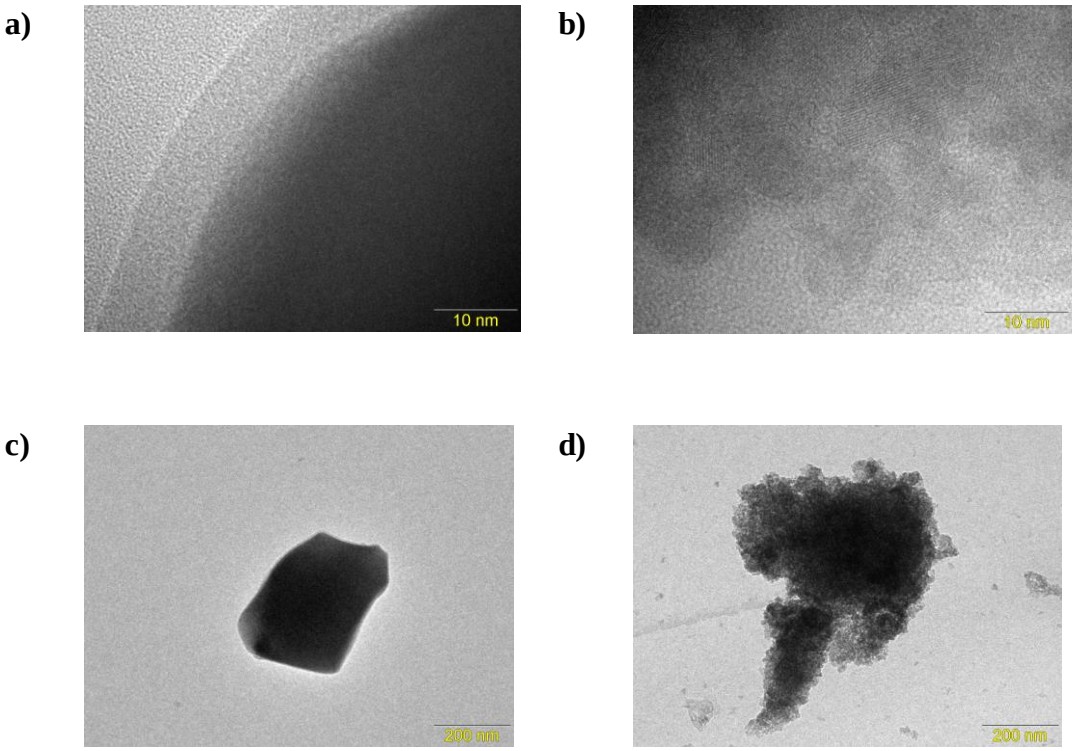

Scheme 13: Illustration of the grafting reaction

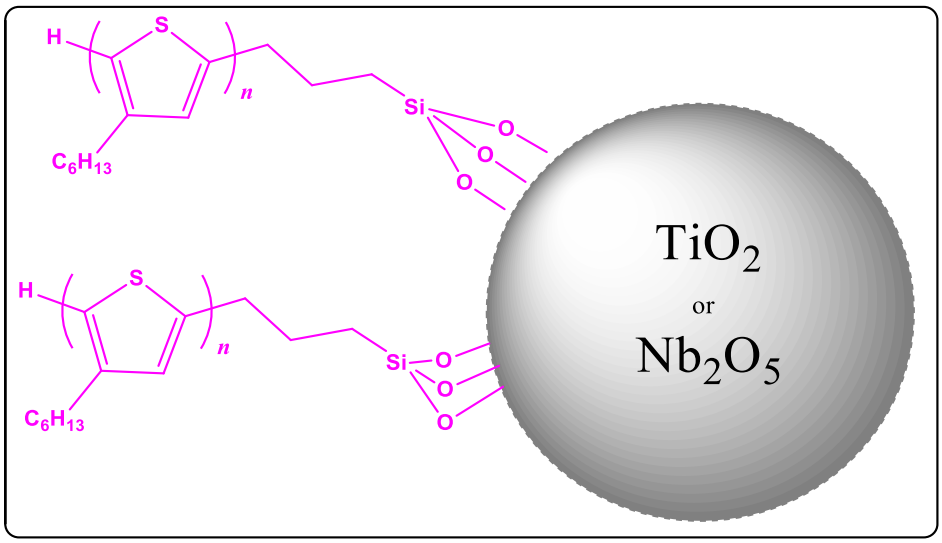

Photoluminescence (PL) spectra of the materials in in chloroform P3HT, red curve, of the oxides, blue curve, and grafted particles, black curve, is presented in Figure 50. The most intense peak of P3HT at 580 nm is an emission characteristic of the P3HT backbone that arises

from the relaxation of excited π-electron to the ground state while the shoulder around 640 nm is related to interchain states and the broad emission spectrum in the range of 300–600 nm can be attributed to the π–π* transition of the conjugated system. The addition of oxides nanoparticles to the polymer solution in a concentration calculated with respect to the mass composition of the one used to the graft reaction, per Beer's law, the absorbance is linear with the concentration or density of absorbers. The spectra exhibit a small quenching on the photoluminescence properties of P3HT when we have the mixture (P3HT+TiO_2 and P3HT+Nb_2O_5, green curve), as presented in Figure 50a and 50b. It was supposed, that under these conditions, the concentration of the oxide was too low to quench significantly the emission signal. On the contrary, it is possible to observe a quenching on the intensity grafted particles to one third of the intensity in the spectra of the polymer, suggesting an efficient charge transfer from the polymer to the oxide nanoparticles. As same as observed by Xu et al. (XU, 2012) the spectra of the grafted particles are strctureless compared with P3HT and the mixed sample. The same behavior was observed in both materials, TiO_2@P3HT and Nb_2O_5@P3HT. Since PL and charge transfer compete, the decrease of PL intensity in polymers is typically regarded as a good sign for Forster energy transfer and/or charge transfer from the polymers to acceptor materials (e.g. TiO_2, CdS, and CdSe). Forster energy transfer requires spectral overlap and electric dipole orientation between polymer emission and acceptor absorbance, while charge transfer typically requires a donor/acceptor interface with suitable energy level alignment between the two materials (BEEK, WALDO J. E., 2004; ZHANG, Y., 2006; XU, 2012). The PL of P3HT, as observed at Figure 51 is in a range of 550–800 nm, while TiO_2 has absorbance less than 350 nm (XU, 2012), resulting in a spectral overlap between them. However, the LUMO of P3HT is -3.2 eV, while the minimum of conduction band of TiO_2 is -4.2 eV, supporting a photoinduced charge transfer from P3HT to TiO_2 (XU, 2011).

Figure 50: PL spectra for a) P3HT, TiO_2@P3HT and TiO_2 and b) P3HT, Nb_2O_5@P3HT and Nb_2O_5 using λ_{Ex} = 455 nm and concentration of 1 x10^{-5} M.

a)

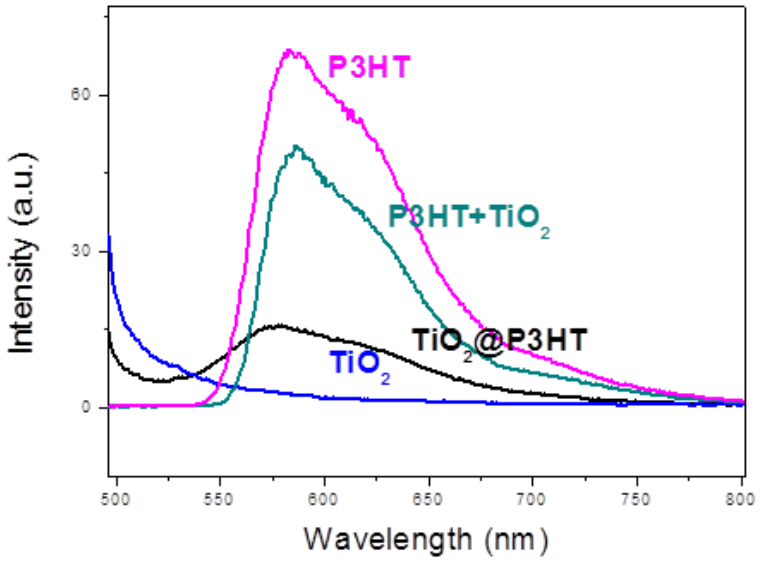

b)

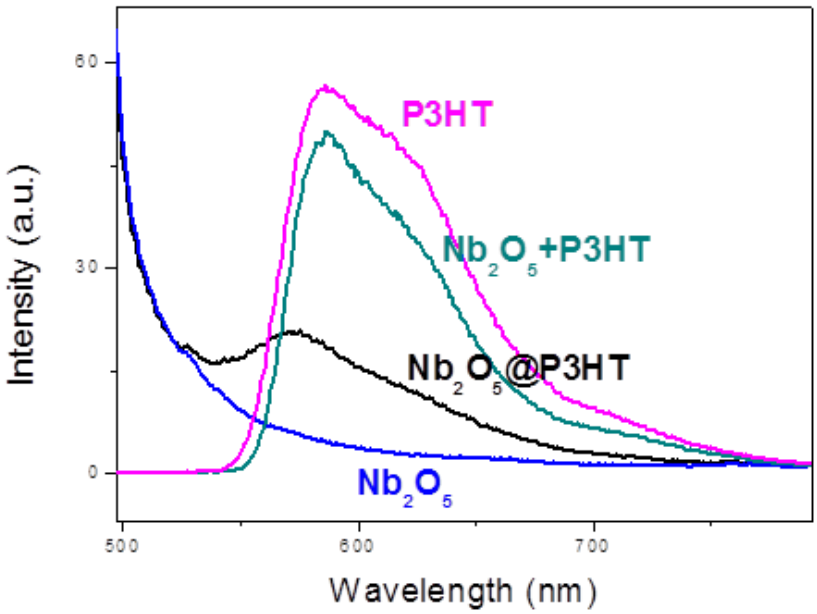

In order to study the charge transfer process and the photo induced properties, fluorescence lifetime imaging (FLIM) coupled with confocal microscopy has been performed for the grafted samples, the polymer and the oxides. In this technique, an image is generated and each pixel of this image generates a PL spectra, as presented at Figure 51. This experiment

is particularly useful for this system since the spectrum obtained in the conventional equipment is a mixture of all elements in solution, i.e., solvent and particles.

Figure 51: Confocal image for the samples in a) TiO_2, b) P3HT film, c) TiO_2@P3HT and d) Nb_2O_5@P3HT, using λ_{Ex} = 455 nm and concentration of 1 x10^{-5} M.

a) TiO_2 **b)** P3HT film

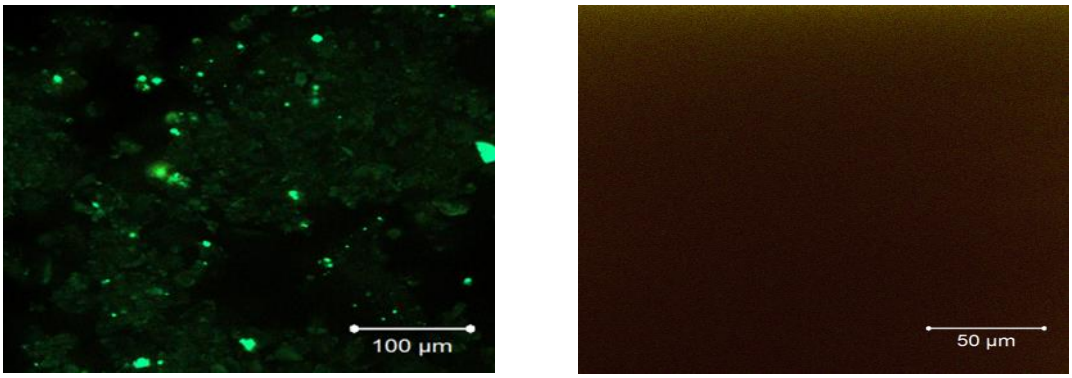

c) TiO_2@P3HT **d)** Nb_2O_5@P3HT

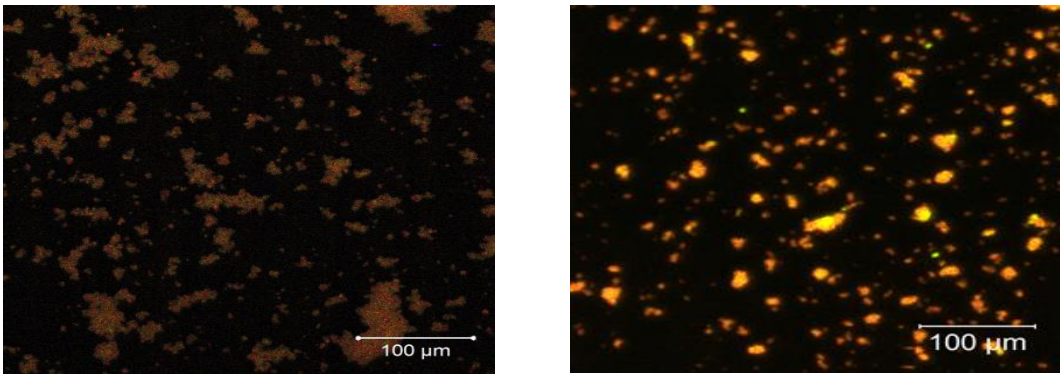

Figure 52 presents the PL in solid and liquid state for the materials. Measurements in solid state have shown a blue shift on the emission of the grafted particles, both for TiO_2@P3HT and Nb_2O_5@P3HT. Data show also a significant extinction of PL intensity compared to the polymer solution. It is also interesting to note that the polymer grown in-situ by Zhang *et al.*(ZHANG, Y., 2006) have shown a bluish spectrum compared to their P3HT. He attributed the shift to the shorter conjugation length, due to the spatial constraints imposed by the template

during growth. Also, Xu et al. (XU, 2012), observed the blue shift of the grafted samples and had attributed to the polymer conformation in the hybrid nanoparticle. In our study, the conformational parameters are not suitable, once the polymer is grafted into the particles and not growth from the oxide. Here, we attribute the blue shift to an efficient process of charge transfer from the polymer to the particle.

Figure 52: Confocal images of the prepared samples in a) P3HT film, b) P3HT in chloroform, c) dried TiO_2@P3HT, d) another region of the sample TiO_2@P3HT, e) dried Nb_2O_5@P3HT and f) comparison with intensities for non-illuminated (red) and after illumination for Nb_2O_5@P3HT.

a)

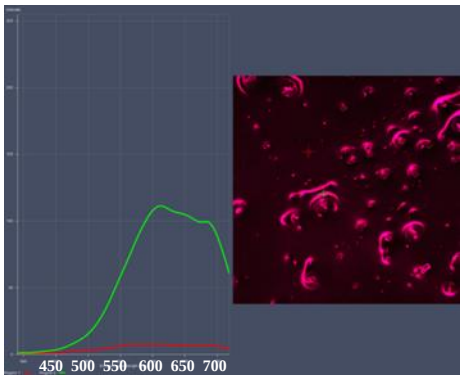

b)

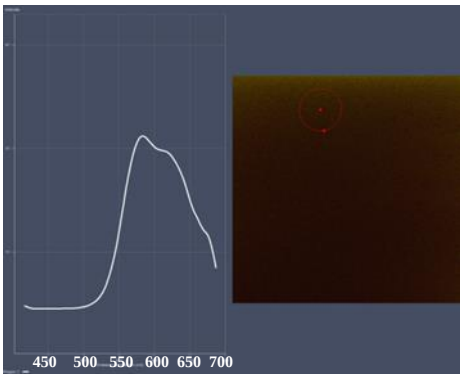

c)

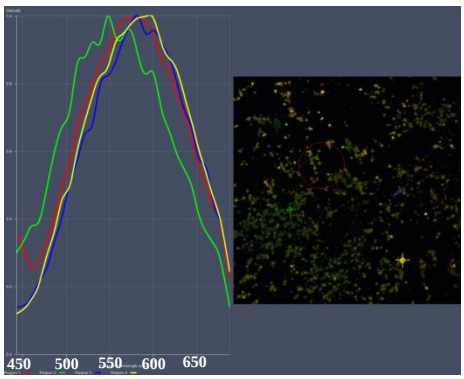

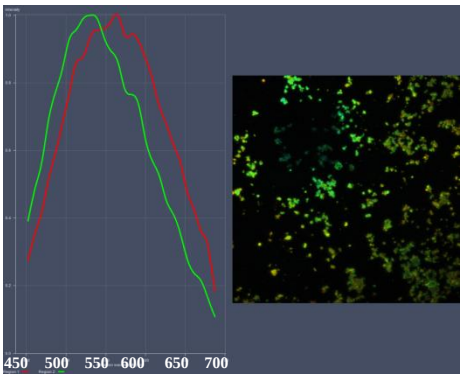

d)

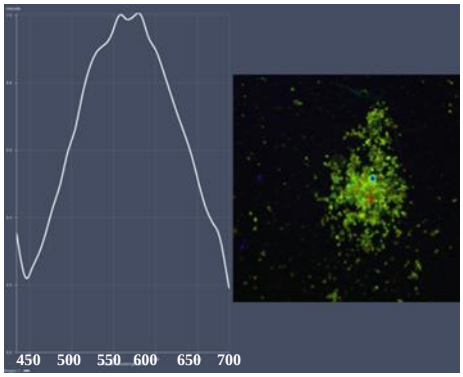

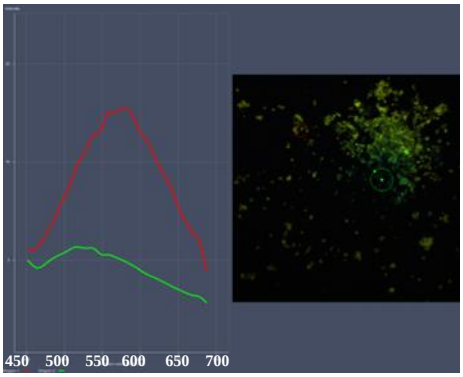

The measurements were carried out on samples with different concentrations and in different solvents, chloroform and o-dichlorobenzene. However, there were no significant difference in the issue regarding the significant quenching of the intensity comparing the intensity of the polymer solution and the grafted particles and also the emission have shown the same trending for blue shift under and after illumination. Also life-time experiments and lower concentrated samples are provided. The lifetime measurements are shown in Figure 53.

Figure 53: a) the P3HT polymer solid-state, b) TiO_2@P3HT and c) Nb_2O_5@P3HT. It is noteworthy that in these images the colors no longer correspond to their issue, but it is equivalent to their lifetime, where blue represents longer and red lower lifetimes using two photons excitation.

a) P3HT

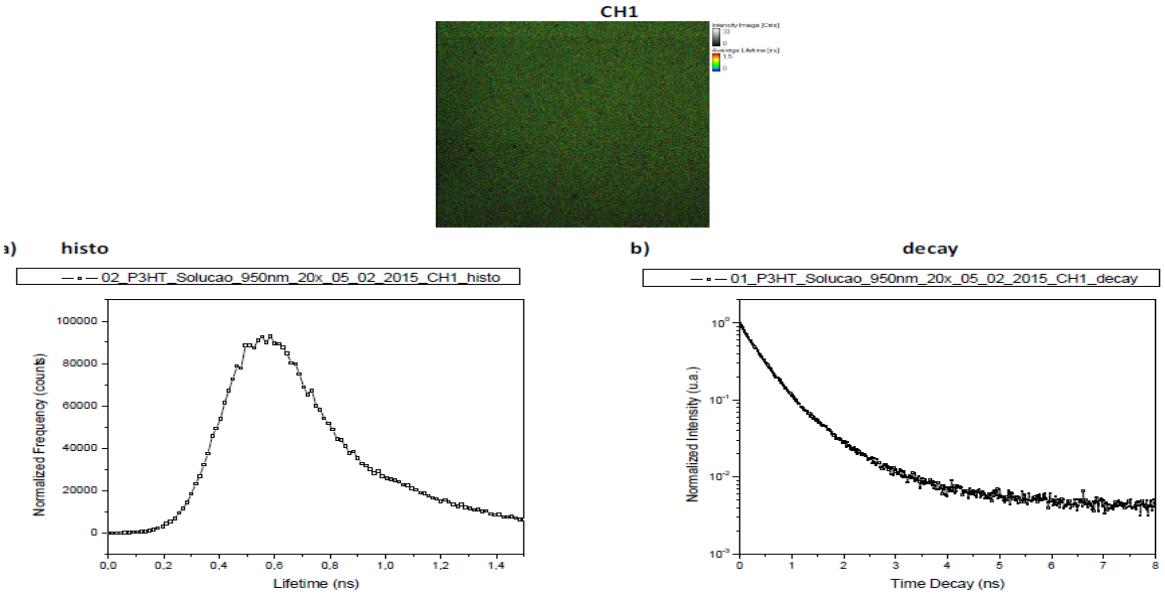

b) TiO_2@P3HT

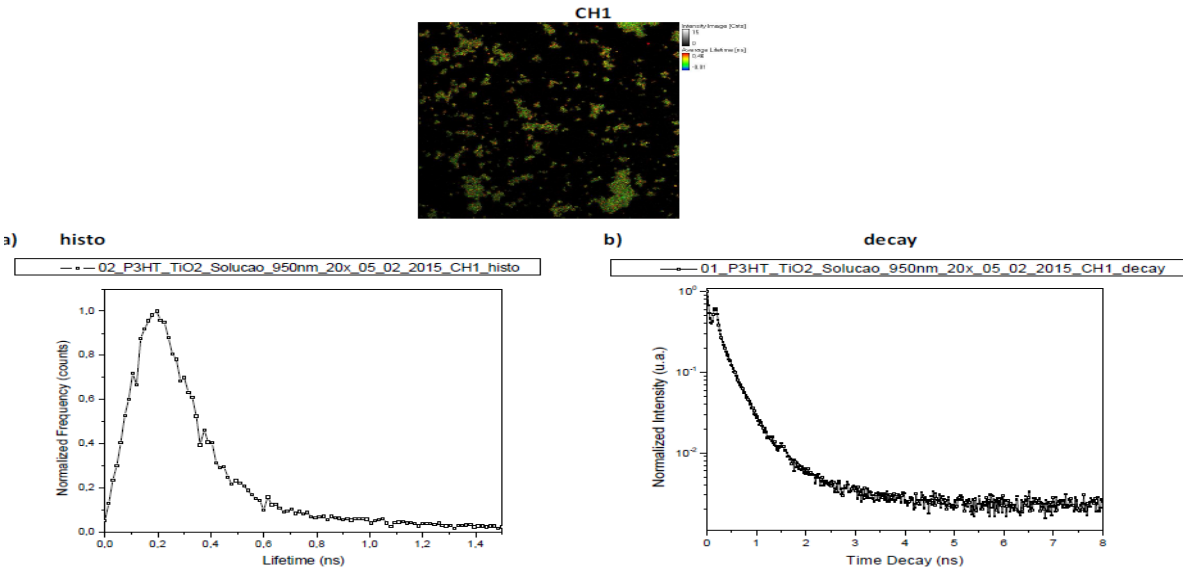

c) Nb_2O_5@P3HT

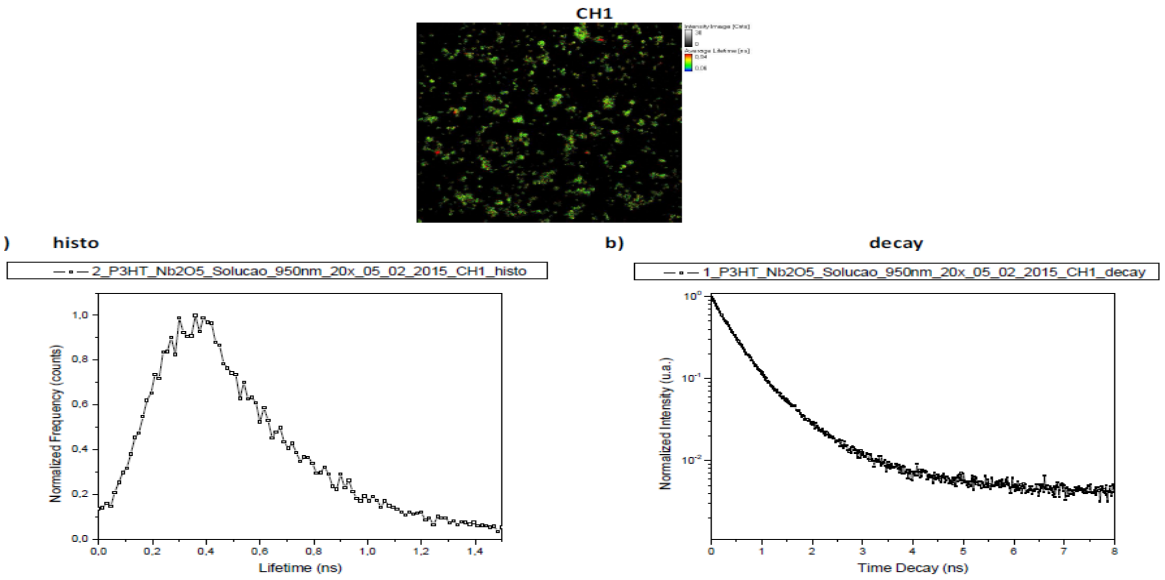

From the results, it is possible to observe that there is a significant decrease in the polymer lifetime, having its maximum at 0.6 ns for the polymer, P3HT non-grafted, compared to TiO_2@P3HT, 0.2 ns and Nb_2O_5@P3HT, 0.35 ns. Based on all the results presented here we propose a charge transfer study model of these nanoparticles.

In photoluminescence phenomenon in the film polymer P3HT, according to the incidence of photons, the excitons are generated, diffuse and emit the lowest energy region around 550 nm. However, in the hybrid particle, a short-term competition occurs where the generated excitons are annihilated by polarons formed in the interface material. So, the diffusion length is smaller, the emission will occur in higher energy regions, around 30 nm shifted to blue region, and its lifetime be much smaller than the polymer. This mechanism suggests the formation of an electric dipole, as illustrated in Figure 54.

Figure 54: Illustration of the formation of electric dipoles in the hybrid particles.

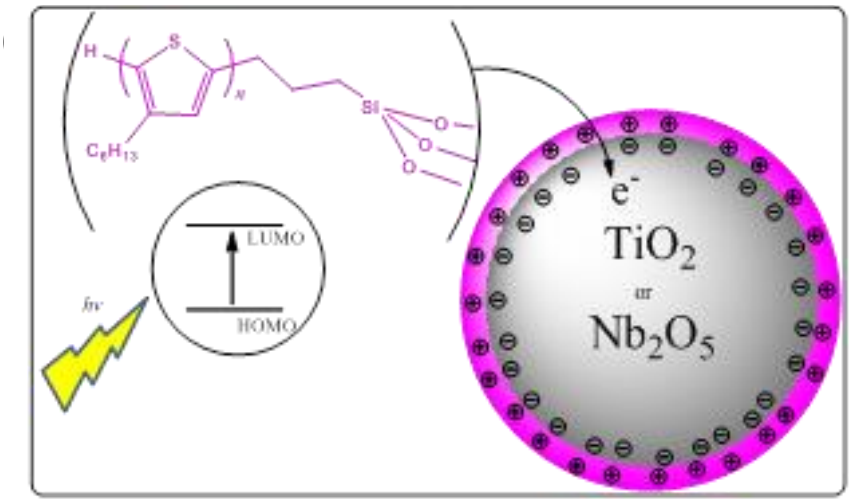

In order to detect these dipoles, relaxometry measurements are proposed. This technique works on the principle of relaxation for the return of the spins to equilibrium state when the radio frequency withdrawn after having absorbed a certain amount of energy from the energy electromagnetic radiation at its resonant frequency. In the process of relaxation NMR usually considered as the spin-lattice relaxation times and spin-spin T1 and T2, respectively (PRETO 2011). Thus, relaxometry is used to determine the relaxation times T1 and T2 corresponding to hydrogen nuclei of different chemical compounds present in the samples. The relaxometry measures performed for the hybrid particles, TiO_2@P3HT, Figure 55, has a long spin-spin relaxation, T2, for the samples under different illumination than the same sample in the dark. Since the relaxation time of the hybrid nanoparticles was decreasing as a function of illumination time inside the ellipse in Figure 55. This result indicates that the electronic environment where the nanoparticles are is different under illumination, suggesting that there is effectively the formation of electric dipole, due to influences the spin-spin relaxation. However, it is not possible to quantify using this technique.

Figure 55: T2 values plotted as a function of illumination time for the sample TiO_2@P3HT: the left side are measurements in the dark after lighting period and right side inside the ellipse measurements made during the illumination.

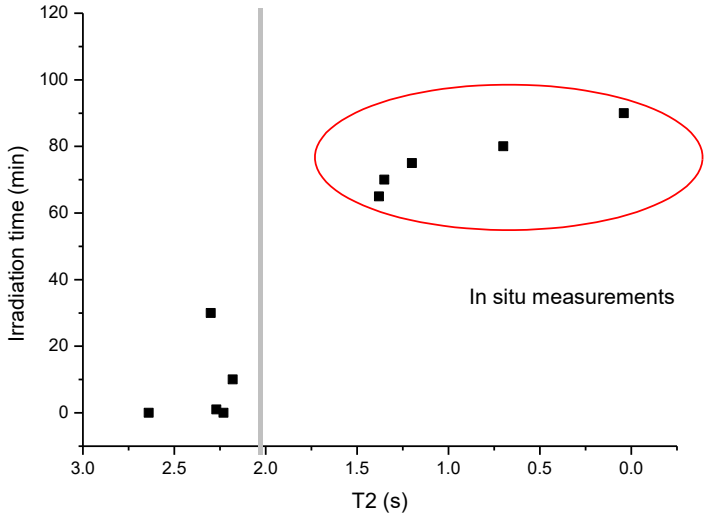

Conclusions

The photoluminescent properties and the lifetimes of the grafted nanoparticles were investigated. Results of PL measurements show a remarkable blue shift in the luminescence spectra for the grafted samples, accompanied by substantial quenching of the emission and reduction of the lifetime. The luminescence quenching is due to the transfer of photogenerated electrons from the polymer to the oxide nanoparticles while the blue shift is attributable to the electron charging of the nanoparticles.

CONCLUSION

In this work, we have explored many facets to synthetize n type materials for application in solar cells. A sort of comonomers and oligomers were studied and synthetized and some were applied in devices. It was developed a novel route, easy and clean, to polymerize C_{60}. Optimization of the devices are needed but the characterization of the materials and initial OPV results suggests that they could be promising. The synthesis of the nanostructured titanium oxide was successfully synthesized by microwave assisted hydrothermal in different and mild conditions and lower times, obtaining materials with high surface area and promising for pastes preparation for DSSCs. Despite many synthesis have been reported so far, our system delivers nanotubes-like materials using TTIP as precursor. In this way the influence of the sodium ions in this synthesis, crystal formation and mechanism were investigated. In addition, some of the particles synthetized were used to synthetized grafted systems, polymer@oxide. These hybrid nanoparticles were used to study photoluminescent properties. This system could be used as a model to study charge transport in organic-inorganic systems. Some complementary studies, such as electrical measurements and theoretical studies are in corse to complete this concept.

To obtain these results, a wide range of characterization techniques have been explored and studied. It was used the characterization of organic and inorganic materials, trainnig for assemble the devices and its electrical characterization. Despite the devices results are here presented only for the fullerene derivatives, DSSC were also made with poor efficiency and low reproductbility, whence not presented. The hybrid system allowed a deeply understand of the charge tranfer process and theories, already presented in the literature, and adaptation of these theories in our developed system. This interpretation corraborates with the devolopement of the other materials, since the sought properties are well undestood.

REFERENCES

ADAMOPOULOS, G.; HEISER, T.; GIOVANELLA, U.; OULD-SAAD, S.; VAN DE WETERING, K.I.; BROCHON, C.; ZORBA, T.; PARASKEVOPOULOS, K.M.; HADZIIOANNOU, G. Electronic transport properties aspects and structure of polymer-fullerene based organic semiconductors for photovoltaic devices. **Thin Solid Films**, v.511–512, p.371, 2006.

AMBIENTE, M.D.M. Energia Solar. Brasília. 2012, 2012.

ANDERSSON, S.; WADSLEY, A.D. The structures of Na2Ti6O13 and Rb2Ti6O13 and the alkali metal titanates. **Acta Crystallographica**, v.15, n.3, p.194, 1962.

ARICI, E.; SARICIFTCI, N.S.; MEISSNER, D. Hybrid Solar Cells Based on Nanoparticles of CuInS2 in Organic Matrices. **Advanced Functional Materials**, v.13, n.2, p.165, 2003.

ARIN, M.; WATTÉ, J.; POLLEFEYT, G.; DE BUYSSER, K.; VAN DRIESSCHE, I.; LOMMENS, P. Low temperature deposition of TiO2 layers from nanoparticle containing suspensions synthesized by microwave hydrothermal treatment. **Journal of Sol-Gel Science and Technology**, v.66, n.1, p.100, 2013.

AUDOUIN, F.; NUFFER, R.; MATHIS, C. Synthesis of di- and tetra-adducts by addition of polystyrene macroradicals onto fullerene C60. **Journal of Polymer Science Part A: Polymer Chemistry**, v.42, n.14, p.3456, 2004.

AWADA, H.; MEDLEJ, H.; BLANC, S.; DELVILLE, M.-H.; HIORNS, R.C.; BOUSQUET, A.; DAGRON-LARTIGAU, C.; BILLON, L. Versatile functional poly(3-hexylthiophene) for hybrid particles synthesis by the grafting onto technique: Core@shell ZnO nanorods. **Journal of Polymer Science Part A: Polymer Chemistry**, v.52, n.1, p.30, 2014.

O´REGAN, B., GRATZEL, M.. A low-cost, high-efficiency solar cell based on dye-sensitized colloidal TiO_2 films. **Nature**, v.353, p.737, 1991.

BABU, V.J.; VEMPATI, S.; SUNDARRAJAN, S.; SIREESHA, M.; RAMAKRISHNA, S. Effective nanostructred morphologies for efficient hybrid solar cells. **Solar Energy**, v.106, p.1, 2014.

BALDASSARI, S.; KOMARNENI, S.; MARIANI, E.; VILLA, C. Rapid Microwave–Hydrothermal Synthesis of Anatase Form of Titanium Dioxide. **Journal of the American Ceramic Society**, v.88, n.11, p.3238, 2005.

BALL, Z.T.; SIVULA, K.; FRÉCHET, J.M.J. Well-Defined Fullerene-Containing Homopolymers and Diblock Copolymers with High Fullerene Content and Their Use for Solution-Phase and Bulk Organization. **Macromolecules**, v.39, n.1, p.70, 2006.

BARRAU, S.; HEISER, T.; RICHARD, F.; BROCHON, C.; NGOV, C.; VAN DE WETERING, K.; HADZIIOANNOU, G.; ANOKHIN, D.V.; IVANOV, D.A. Self-Assembling

of Novel Fullerene-Grafted Donor–Acceptor Rod−Coil Block Copolymers. **Macromolecules**, v.41, n.7, p.2701, 2008.

BARRON, A.R. Physical Methods in Chemistry and Nano Science: Rice University**:** 917 p., 1992.

BASTIAENS, P.I.H.; SQUIRE, A. Fluorescence lifetime imaging microscopy: spatial resolution of biochemical processes in the cell. **Trends in Cell Biology**, v.9, n.2, p.48, 1999.

BAVYKIN, D.V.; FRIEDRICH, J.M.; WALSH, F.C. Protonated Titanates and TiO2 Nanostructured Materials: Synthesis, Properties, and Applications. **Advanced Materials**, v.18, n.21, p.2807, 2006.

BEEK, W.J.E.; JANSSEN, R.A.J. Photoinduced Electron Transfer in Heterosupramolecular Assemblies of TiO2 Nanoparticles and Terthiophene Carboxylic Acid in Apolar Solvents. **Advanced Functional Materials**, v.12, n.8, p.519, 2002.

BEEK, W.J.E.; JANSSEN, R.A.J. Spacer length dependence of photoinduced electron transfer in heterosupramolecular assemblies of TiO2 nanoparticles and terthiophene. **Journal of Materials Chemistry**, v.14, n.18, p.2795, 2004.

BILECKA, I.; NIEDERBERGER, M. Microwave chemistry for inorganic nanomaterials synthesis. **Nanoscale**, v.2, n.8, p.1358, 2010.

BINNIG, G.; QUATE, C.F.; GERBER, C. Atomic Force Microscope. **Physical Review Letters**, v.56, n.9, p.930, 1986.

BOON, F.; THOMAS, A.; CLAVEL, G.; MOERMAN, D.; DE WINTER, J.; LAURENCIN, D.; COULEMBIER, O.; DUBOIS, P.; GERBAUX, P.; LAZZARONI, R.; RICHETER, S.; MEHDI, A.; CLÉMENT, S. Synthesis and characterization of carboxystyryl end-functionalized poly(3-hexylthiophene)/TiO2 hybrids in view of photovoltaic applications. **Synthetic Metals**, v.162, n.17-18, p.1615, 2012.

BOON, F.; MOERMAN, D.; LAURENCIN, D.; RICHETER, S.; GUARI, Y.; MEHDI, A.; DUBOIS, P.; LAZZARONI, R.; CLÉMENT, S. Synthesis of TiO2–Poly(3-hexylthiophene) Hybrid Particles through Surface-Initiated Kumada Catalyst-Transfer Polycondensation. **Langmuir**, v.30, n.38, p.11340, 2014.

BOUCLE, J.; RAVIRAJAN, P.; NELSON, J. Hybrid polymer-metal oxide thin films for photovoltaic applications. **Journal of Materials Chemistry**, v.17, n.30, p.3141, 2007.

BOUDREAULT, P.-L.T.; NAJARI, A.; LECLERC, M. Processable Low-Bandgap Polymers for Photovoltaic Applications. **Chemistry of Materials**, v.23, n.3, p.456, 2011.

BOUSQUET, A.; AWADA, H.; HIORNS, R.C.; DAGRON-LARTIGAU, C.; BILLON, L. Conjugated-polymer grafting on inorganic and organic substrates: A new trend in organic electronic materials. **Progress in Polymer Science**, v.39, n.11, p.1847, 2014.

BRÄSE, S.; GIL, C.; KNEPPER, K.; ZIMMERMANN, V. Organic Azides: An Exploding Diversity of a Unique Class of Compounds. **Angewandte Chemie International Edition**, v.44, n.33, p.5188, 2005.

BRINKER, C.J. Hydrolysis and condensation of silicates: Effects on structure. **Journal of Non-Crystalline Solids**, v.100, n.1–3, p.31, 1988.

BRISENO, A.L.; HOLCOMBE, T.W.; BOUKAI, A.I.; GARNETT, E.C.; SHELTON, S.W.; FRÉCHET, J.J.M.; YANG, P. Oligo- and Polythiophene/ZnO Hybrid Nanowire Solar Cells. **Nano Letters**, v.10, n.1, p.334, 2010.

BYRAPPA, K.; YOSHIMURA, M. 1 - Hydrothermal Technology—Principles and Applications. In: (Ed.). **Handbook of Hydrothermal Technology**. Norwich, NY: William Andrew Publishing, 2001a.

BYRAPPA, K.; YOSHIMURA, M. 3 - Apparatus. In: (Ed.). **Handbook of Hydrothermal Technology**. Norwich, NY: William Andrew Publishing, 2001b.

CALLISTER, W.D., Ed. **Materials science and engineering: an introduction**, p.p. 811, 3rd ed ed, 1994.

CASES, M.; DURAN, M.; MESTRES, J.; MARTÍN, N.; SOLÀ, M. Mechanism of the Addition Reaction of Alkyl Azides to [60]Fullerene and the Subsequent N2 Extrusion to Form Monoimino-[60]fullerenes. **The Journal of Organic Chemistry**, v.66, n.2, p.433, 2000.

CHANDRASEKARAN, J., AJJAN, K.B., MARUTHAMUTHU, S., MANOHARAN D., KUMAR, S., Hybrid solar cell based on blending of organic and inorganic materials--An overview. **Renewable and Sustainable Energy Reviews**, v.15, n.2, p.1228, 2011.

CHEN, D.; HUANG, F.; CHENG, Y.-B.; CARUSO, R.A. Mesoporous Anatase TiO2 Beads with High Surface Areas and Controllable Pore Sizes: A Superior Candidate for High-Performance Dye-Sensitized Solar Cells. **Advanced Materials**, v.21, n.21, p.2206, 2009.

CHEN, P.; PENG, J.-D.; LIAO, C.-H.; SHEN, P.-S.; KUO, P.-L. Microwave-assisted hydrothermal synthesis of TiO spheres with efficient photovoltaic performance for dye-sensitized solar cells. **Journal of Nanoparticle Research**, v.15, n.3, p.1, 2013.

CHEN, X.; MAO, S.S. Titanium Dioxide Nanomaterials: Synthesis, Properties, Modifications, and Applications. **Chemical Reviews**, Disponível em http://dx.doi.org/10.1021/cr0500535, Acessado em 2007/07/01.

CHOI, M.G.; LEE, Y.-G.; SONG, S.-W.; KIM, K.M. Lithium-ion battery anode properties of TiO2 nanotubes prepared by the hydrothermal synthesis of mixed (anatase and rutile) particles. **Electrochimica Acta**, v.55, n.20, p.5975, 2010.

CONIBEER, G. Third-generation photovoltaics. **Materials Today**, v.10, n.11, p.42, 2007.

CORRADI, A.B.; BONDIOLI, F.; FOCHER, B.; FERRARI, A.M.; GRIPPO, C.; MARIANI, E.; VILLA, C. Conventional and Microwave-Hydrothermal Synthesis of TiO2 Nanopowders. **Journal of the American Ceramic Society**, v.88, n.9, p.2639, 2005.

CUI, L.; HUI, K.N.; HUI, K.S.; LEE, S.K.; ZHOU, W.; WAN, Z.P.; THUC, C.-N.H. Facile microwave-assisted hydrothermal synthesis of TiO2 nanotubes. **Materials Letters**, v.75, p.175, 2012.

DANG, M.T.; HIRSCH, L.; WANTZ, G. P3HT:PCBM, Best Seller in Polymer Photovoltaic Research. **Advanced Materials**, v.23, n.31, p.3597, 2011.

DAR, M.I.; CHANDIRAN, A.K.; GRATZEL, M.; NAZEERUDDIN, M.K.; SHIVASHANKAR, S.A. Controlled synthesis of TiO2 nanoparticles and nanospheres using a microwave assisted approach for their application in dye-sensitized solar cells. **Journal of Materials Chemistry A**, v.2, n.6, p.1662, 2014.

DENNLER, G., SCHARBER, M.C., BRABEC, C.J., Polymer-Fullerene Bulk-Heterojunction Solar Cells.**Advanced Energy** Materials, v. 21, n 13, p. 1323-1338, 2009.

DHAS, V.; MUDULI, S.; AGARKAR, S.; RANA, A.; HANNOYER, B.; BANERJEE, R.; OGALE, S. Enhanced DSSC performance with high surface area thin anatase TiO2 nanoleaves. **Solar Energy**, v.85, n.6, p.1213, 2011.

DREES, M.; HOPPE, H.; WINDER, C.; NEUGEBAUER, H.; SARICIFTCI, N.S.; SCHWINGER, W.; SCHAFFLER, F.; TOPF, C.; SCHARBER, M.C.; ZHU, Z.; GAUDIANA, R. Stabilization of the nanomorphology of polymer-fullerene "bulk heterojunction" blends using a novel polymerizable fullerene derivative. **Journal of Materials Chemistry**, v.15, n.48, p.5158, 2005.

ENERGIA, M.D.M.E. Análise da Inserção da Geração Solar na Matriz Energética Brasileira. 2012.

FERNANDES, F.L. **Carvão de endocarpo de coco da baía ativado quimicamente com $ZnCl_2$ e fisicamente com vapor d'água: Produção, caracterização, modificações químicas e aplicação na adsorção do íon cloreto.** Pós Graduação em Química, Universidade Federal da Paraíba, João Pessoa -PB, 2008.

FLORY, P.J. **Principles of Polymer Chemistry**. Ithaca, New York: Cornell University Press, 1953.

FLORY, P. J.. **Journal of the American Chemical Society**, v.58, p.1877, 1936.

FRANK K. KO, Y.W. **Introduction to Nanofiber Materials**: Cambridge University Press, 2014.

FRAUNHOFER INSTITUTE FOR SOLAR ENERGY SYSTEMS, I. PHOTOVOLTAICS REPORT. 2015.

GHOLAMKHASS, B.; PECKHAM, T.J.; HOLDCROFT, S. Poly(3-hexylthiophene) bearing pendant fullerenes: aggregation vs. self-organization. **Polymer Chemistry**, v.1, n.5, p.708, 2010.

GIACALONE, F.; MARTÍN, N. Fullerene Polymers: Synthesis and Properties. **Chemical Reviews**, v.106, n.12, p.5136, 2006.

GRATZEL, M. Photoelectrochemical cells. **Nature**, v.414, n.6861, p.338, 2001.

GRÄTZEL, M. Dye-sensitized solar cells. **Journal of Photochemistry and Photobiology C: Photochemistry Reviews**, v.4, p.145, 2003.

GREEN, M.A.; EMERY, K.; HISHIKAWA, Y.; WARTA, W.; DUNLOP, E.D. Solar cell efficiency tables (version 44). **Progress in Photovoltaics: Research and Applications**, v.22, n.7, p.701, 2014.

GRÖSSER, T.; PRATO, M.; LUCCHINI, V.; HIRSCH, A.; WUDL, F. Ring Expansion of the Fullerene Core by Highly Regioselective Formation of Diazafulleroids. **Angewandte Chemie International Edition in English**, v.34, n.12, p.1343, 1995.

GONZÁLEZ, D.M., KÖRSTGENS, V., YAO, Y., SONG, L., SANTORO, G., ROTH, S. V., MÜLLER-BUSCHBAUM P., Improved Power Conversion Efficiency of P3HT:PCBM Organic Solar Cells by Strong Spin–Orbit Coupling-Induced Delayed Fluorescence. v.5, n. 8 p. 1401770, 2015

GÜGEL, A.; BELIK, P.; WALTER, M.; KRAUS, A.; HARTH, E.; WAGNER, M.; SPICKERMANN, J.; MÜLLEN, K. The repetitive Diels-Alder reaction: A new approach to [60]fullerene maindashchain polymers. **Tetrahedron**, v.52, n.14, p.5007, 1996.

GÜNES, S.; FRITZ, K.P.; NEUGEBAUER, H.; SARICIFTCI, N.S.; KUMAR, S.; SCHOLES, G.D. Hybrid solar cells using PbS nanoparticles. **Solar Energy Materials and Solar Cells**, v.91, n.5, p.420, 2007a.

GÜNES, S.; NEUGEBAUER, H.; SARICIFTCI, N.S. Conjugated Polymer-Based Organic Solar Cells. **Chemical Reviews**, v.107, n.4, p.1324, 2007b.

HALME, J.; VAHERMAA, P.; MIETTUNEN, K.; LUND, P. Device Physics of Dye Solar Cells. **Advanced Materials**, v.22, n.35, p.E210, 2010.

HART, J.N.; CERVINI, R.; CHENG, Y.B.; SIMON, G.P.; SPICCIA, L. Formation of anatase TiO2 by microwave processing. **Solar Energy Materials and Solar Cells**, v.84, n.1–4, p.135, 2004.

HEISER, T.; ADAMOPOULOS, G.; BRINKMANN, M.; GIOVANELLA, U.; OULD-SAAD, S.; BROCHON, C.; VAN DE WETERING, K.; HADZIIOANNOU, G. Nanostructure of self-assembled rod-coil block copolymer films for photovoltaic applications. **Thin Solid Films**, v.511–512, p.219, 2006.

HIORNS, R.C.; DE BETTIGNIES, R.; LEROY, J.; BAILLY, S.; FIRON, M.; SENTEIN, C.; KHOUKH, A.; PREUD'HOMME, H.; DAGRON-LARTIGAU, C. High Molecular Weights, Polydispersities, and Annealing Temperatures in the Optimization of Bulk-Heterojunction Photovoltaic Cells Based on Poly(3-hexylthiophene) or Poly(3-butylthiophene). **Advanced Functional Materials**, v.16, n.17, p.2263, 2006.

HOLDER, J. S., SOMMERDIJK, A. J. M., WILLIAMS, N.; J., NOLTE, S., HIORNS R. C., JONES, R., The first example of a poly(ethylene oxide)-poly(methylphenylsilane) amphiphilic block copolymer: vesicle formation in water. **Chemical Communications**, n.14, p.1445, 1998.

HUANG, C.-H.; YANG, Y.-T.; DOONG, R.-A. Microwave-assisted hydrothermal synthesis of mesoporous anatase TiO2 via sol–gel process for dye-sensitized solar cells. **Microporous and Mesoporous Materials**, v.142, n.2–3, p.473, 2011.

HUANG, K.-C.; CHIEN, S.-H. Improved visible-light-driven photocatalytic activity of rutile/titania-nanotube composites prepared by microwave-assisted hydrothermal process. **Applied Catalysis B: Environmental**, v.140–141, p.283, 2013.

IIJIMA, S. **Nature**, v.354, n.56, p.8, 1991.

ISHII, A.; MIYASAKA, T. A high voltage organic-inorganic hybrid photovoltaic cell sensitized with metal-ligand interfacial complexes. **Chemical Communications**, v.48, n.79, p.9900, 2012.

ISMAIL, A.A.; BAHNEMANN, D.W. Mesoporous titania photocatalysts: preparation, characterization and reaction mechanisms. **Journal of Materials Chemistry**, v.21, n.32, p.11686, 2011.

ITO, H.; ISHIDA, Y.; SAIGO, K. Regio- and diastereo-controlled synthesis of bis(formylmethano)[60]fullerenes and their application to the formation of [60]fullerene pearl-necklace polyimines. **Tetrahedron Letters**, v.47, n.18, p.3095, 2006.

ITO, S.; CHEN, P.; COMTE, P.; NAZEERUDDIN, M.K.; LISKA, P.; PÉCHY, P.; GRÄTZEL, M. Fabrication of screen-printing pastes from TiO2 powders for dye-sensitised solar cells. **Progress in Photovoltaics: Research and Applications**, v.15, n.7, p.603, 2007.

IUPAC. COMPENDIUM OF CHEMICAL TERMINOLOGY, N.E.T.G.B.C.B.A.D.M.A.A.W.B.S.P., OXFORD (1997). XML ON-LINE CORRECTED VERSION: HTTP://GOLDBOOK.IUPAC.ORG (2006-) CREATED BY M. NIC, J. JIRAT, B. KOSATA; UPDATES COMPILED BY A. JENKINS. ISBN 0-9678550-9-8. DOI:10.1351/GOLDBOOK.

JAYARAMAN, S.; KUMAR, P.S.; MANGALARAJ, D.; RAJARATHNAM, D.; RAMAKRISHNA, S.; SRINIVASAN, M.P. Enhanced luminescence and charge separation in polythiophene-grafted, gold nanoparticle-decorated, 1-D ZnO nanorods. **RSC Advances**, v.4, n.22, p.11288, 2014.

JI, Y.; NIU, H.; ZHANG, H.; WU, W.; CAI, J.; WANG, C.; BAI, X.; WANG, W. Synthesis and electrochromic properties of polybismaleimides containing triphenylamine units. **Journal of Solid State Electrochemistry**, v.18, n.6, p.1537, 2014.

JIANG, B.; YIN, H.; JIANG, T.; JIANG, Y.; FENG, H.; CHEN, K.; ZHOU, W.; WADA, Y. Hydrothermal synthesis of rutile TiO2 nanoparticles using hydroxyl and carboxyl group-containing organics as modifiers. **Materials Chemistry and Physics**, v.98, n.2–3, p.231, 2006.

JOSE, R.; THAVASI, V.; RAMAKRISHNA, S. Metal Oxides for Dye-Sensitized Solar Cells. **Journal of the American Ceramic Society**, v.92, n.2, p.289, 2009.

KASUGA, T.; HIRAMATSU, M.; HOSON, A.; SEKINO, T.; NIIHARA, K. Formation of Titanium Oxide Nanotube. **Langmuir**, v.14, n.12, p.3160, 1998.

KAUR, N.; SINGH, M.; PATHAK, D.; WAGNER, T.; NUNZI, J.M. Organic materials for photovoltaic applications: Review and mechanism. **Synthetic Metals**, v.190, n.0, p.20, 2014.

KHARISOV, B.I.; KHARISSOVA, O.V.; GOMEZ, M.J.; MENDEZ, U.O. Recent Advances in the Synthesis, Characterization, and Applications of Fulleropyrrolidines. **Industrial & Engineering Chemistry Research**, v.48, n.2, p.545, 2009.

KIM, B.; LEE, J.; SEO, J.H.; WUDL, F.; PARK, S.H.; YANG, C. Regioselective 1,2,3-bisazfulleroid: doubly N-bridged bisimino-PCBMs for polymer solar cells. **Journal of Materials Chemistry**, v.22, n.43, p.22958, 2012.

KIM, D.S.; KWAK, S.-Y. The hydrothermal synthesis of mesoporous TiO2 with high crystallinity, thermal stability, large surface area, and enhanced photocatalytic activity. **Applied Catalysis A: General**, v.323, p.110, 2007.

KIM, G.; LEE, K.C.; KIM, J.; LEE, J.; LEE, S.M.; LEE, J.C.; SEO, J.H.; CHOI, W.-Y.; YANG, C. An unprecedented [5,6]-open adduct via a direct benzyne-C60 cycloaddition. **Tetrahedron**, v.69, n.35, p.7354, 2013.

KOMARNENI, S.; RAJHA, R.K.; KATSUKI, H. Microwave-hydrothermal processing of titanium dioxide1. **Materials Chemistry and Physics**, v.61, n.1, p.50, 1999.

KOOISTRA, F.B.; LEUNING, T.M.; MAROTO MARTINEZ, E.; HUMMELEN, J.C. Two new types of [small pi]-conjugation between a fullerene sphere and an addend. **Chemical Communications**, v.46, n.12, p.2097, 2010.

LANDMANN, M.; RAULS, E.; SCHMIDT, W.G. The electronic structure and optical response of rutile, anatase and brookite TiO 2. **Journal of Physics: Condensed Matter**, v.24, n.19, p.195503, 2012.

LEVELL, J.W.; GIARDINI, M.E.; SAMUEL, I.D.W. A hybrid organic semiconductor/silicon photodiode for efficient ultraviolet photodetection. **Optics Express**, v.18, n.4, p.3219, 2010.

LI, C.-Z.; CHUEH, C.-C.; YIP, H.-L.; DING, F.; LI, X.; JEN, A.K.Y. Solution-Processible Highly Conducting Fullerenes. **Advanced Materials**, p.n/a, 2013.

LI, L.; QIN, X.; WANG, G.; QI, L.; DU, G.; HU, Z. Synthesis of anatase TiO2 nanowires by modifying TiO2 nanoparticles using the microwave heating method. **Applied Surface Science**, v.257, n.18, p.8006, 2011.

LIAO, S.-H.; LI, Y.-L.; JEN, T.-H.; CHENG, Y.-S.; CHEN, S.-A. Multiple Functionalities of Polyfluorene Grafted with Metal Ion-Intercalated Crown Ether as an Electron Transport Layer for Bulk-Heterojunction Polymer Solar Cells: Optical Interference, Hole Blocking, Interfacial

Dipole, and Electron Conduction. **Journal of the American Chemical Society**, v.134, n.35, p.14271, 2012.

LIU, N.; CHEN, X.; ZHANG, J.; SCHWANK, J.W. A review on TiO2-based nanotubes synthesized via hydrothermal method: Formation mechanism, structure modification, and photocatalytic applications. **Catalysis Today**, v.225, n.0, p.34, 2014.

LIU, R. Hybrid Organic/Inorganic Nanocomposites for Photovoltaic Cells. **Materials**, v.7, p.2747, 2014.

LU, C.-W.; CAO, Y.; LI, H.; WEBB, C.; PAN, W.-P. Synthesis of TiO2 based on hydrothermal methods using elevated pressures and microwave conditions. **Journal of Thermal Analysis and Calorimetry**, v.116, n.3, p.1241, 2014.

LU, L.; ZHENG, T.; WU, Q.; SCHNEIDER, A.M.; ZHAO, D.; YU, L. Recent Advances in Bulk Heterojunction Polymer Solar Cells. **Chemical Reviews**, v.115, n.23, p.12666, 2015.

LUCAFÒ, M.; PACOR, S.; FABBRO, C.; DA ROS, T.; ZORZET, S.; PRATO, M.; SAVA, G. Study of a potential drug delivery system based on carbon nanoparticles: effects of fullerene derivatives in MCF7 mammary carcinoma cells. **Journal of Nanoparticle Research**, v.14, n.4, p.1, 2012.

LUCAFÒ, M.; GERDOL, M.; PALLAVICINI, A.; PACOR, S.; ZORZET, S.; DA ROS, T.; PRATO, M.; SAVA, G. Profiling the molecular mechanism of fullerene cytotoxicity on tumor cells by RNA-seq. **Toxicology**, v.314, n.1, p.183, 2013.

LUCAFÒ, M.; PELILLO, C.; CARINI, M.; DA ROS, T.; PRATO, M.; SAVA, G. A Cationic [60] Fullerene Derivative Reduces Invasion and Migration of HT-29 CRC Cells in Vitro at Dose Free of Significant Effects on Cell Survival. **Nano-Micro Letters**, v.6, n.2, p.163, 2014.

LUO, L.; HUI, J.; YU, Q.; ZHANG, Z.; JING, D.; WANG, P.; YANG, Y.; WANG, X. Crystal growth by leaps and bounds based on self-assembly: insight from titania. **CrystEngComm**, v.14, n.22, p.7648, 2012.

MABBOTT, G.A. An introduction to cyclic voltammetry. **Journal of Chemical Education**, v.60, n.9, p.697, 1983.

MANFROI, D.C.; DOS ANJOS, A.; CAVALHEIRO, A.A.; PERAZOLLI, L.A.; VARELA, J.A.; ZAGHETE, M.A. Titanate nanotubes produced from microwave-assisted hydrothermal synthesis: Photocatalytic and structural properties. **Ceramics International**, v.40, n.9, Part A, p.14483, 2014.

MAO, Y.; PARK, T.-J.; ZHANG, F.; ZHOU, H.; WONG, S.S. Environmentally Friendly Methodologies of Nanostructure Synthesis. **Small**, v.3, n.7, p.1122, 2007.

MATERIALS EVALUATION AND ENGINEERING, I. Fourier Transform-Infrared Spectroscopy (FTIR), 2016.

MAYER, A.C.; SCULLY, S.R.; HARDIN, B.E.; ROWELL, M.W.; MCGEHEE, M.D. Polymer-based solar cells. **Materials Today**, v.10, n.11, p.28, 2007.

MELCARNE, G.; DE MARCO, L.; CARLINO, E.; MARTINA, F.; MANCA, M.; CINGOLANI, R.; GIGLI, G.; CICCARELLA, G. Surfactant-free synthesis of pure anatase TiO2 nanorods suitable for dye-sensitized solar cells. **Journal of Materials Chemistry**, v.20, n.34, p.7248, 2010.

MICARONI, L.; NART, F.; HÜMMELGEN, I. Considerations about the electrochemical estimation of the ionization potential of conducting polymers. **Journal of Solid State Electrochemistry**, v.7, n.1, p.55, 2002.

MIHAILETCHI, V.D.; KOSTER, L.J.A.; HUMMELEN, J.C.; BLOM, P.W.M. Photocurrent Generation in Polymer-Fullerene Bulk Heterojunctions. **Physical Review Letters**, v.93, n.21, p.216601, 2004.

MILLER, G.P. Reactions between aliphatic amines and [60]fullerene: a review. **Comptes Rendus Chimie**, v.9, n.7–8, p.952, 2006.

MOORE, J.A.; ALI, S.; BERRY, B.C. Stabilization of PCBM domains in bulk heterojunctions using polystyrene-tethered fullerene. **Solar Energy Materials and Solar Cells**, v.118, n.0, p.96, 2013.

MOULE, A.J.; CHANG, L.; THAMBIDURAI, C.; VIDU, R.; STROEVE, P. Hybrid solar cells: basic principles and the role of ligands. **Journal of Materials Chemistry**, v.22, n.6, p.2351, 2012.

MUNIZ, E.C.; GÓES, M.S.; SILVA, J.J.; VARELA, J.A.; JOANNI, E.; PARRA, R.; BUENO, P.R. Synthesis and characterization of mesoporous TiO2 nanostructured films prepared by a modified sol–gel method for application in dye solar cells. **Ceramics International**, v.37, n.3, p.1017, 2011.

NAKAHIRA, A.; KUBO, T.; NUMAKO, C. Formation Mechanism of TiO2-Derived Titanate Nanotubes Prepared by the Hydrothermal Process. **Inorganic Chemistry**, v.49, n.13, p.5845, 2010.

NARAYAN, M.R. Review: Dye sensitized solar cells based on natural photosensitizers. **Renewable and Sustainable Energy Reviews**, v.16, n.1, p.208, 2012.

MARTIN, N., GIACALONE, F., Ed. **Fullerene Polymers: Synthesis, Properties and Applications**: Wiley-VCH, p.311ed, 2009.

NEMATI BIDEH, B.; ROLDAN-CARMONA, C.; SHAHROOSVAND, H.; NAZEERUDDIN, M.K. Low-voltage, high-brightness and deep-red light-emitting electrochemical cells (LECs) based on new ruthenium(ii) phenanthroimidazole complexes. **Dalton Transactions**, v.45, n.17, p.7195, 2016.

NIKIFOROV, M.P.; LAI, B.; CHEN, W.; CHEN, S.; SCHALLER, R.D.; STRZALKA, J.; MASER, J.; DARLING, S.B. Detection and role of trace impurities in high-performance organic solar cells. **Energy & Environmental Science**, v.6, n.5, p.1513, 2013.

NREL. Photoluminescence spectroscopy, 2016.

O'NEIL, E.J.; DIVITTORIO, K.M.; SMITH, B.D. Phosphatidylcholine-Derived Bolaamphiphiles via Click Chemistry. **Organic Letters**, v.9, n.2, p.199, 2007.

ODIAN, G. **Principles of Polymerization**. Hoboken, New Jersey, USA: John Wiley and Sons Inc., 2004.

ODOI, M.Y.; HAMMER, N.I.; SILL, K.; EMRICK, T.; BARNES, M.D. Observation of Enhanced Energy Transfer in Individual Quantum Dot−Oligophenylene Vinylene Nanostructures. **Journal of the American Chemical Society**, v.128, n.11, p.3506, 2006.

ORLOVA, T.P.T., ORLOV, A. P, SHATALOV, O.A.. Perspectives of Fullerene Derivatives in PDT and Radiotherapy of Cancers. **British Journal of Medicine and Medical Research**, v.3, n.4, p.1731, 2013.

OU, H.-H.; LO, S.-L. Review of titania nanotubes synthesized via the hydrothermal treatment: Fabrication, modification, and application. **Separation and Purification Technology**, v.58, n.1, p.179, 2007.

PADILHA, A.F. Microscopia Eletrônica de Transmissão. São Paulo. 2012**:** Página Prof. Poli USP p., 2012.

PANG, Y.L.; LIM, S.; ONG, H.C.; CHONG, W.T. A critical review on the recent progress of synthesizing techniques and fabrication of TiO2-based nanotubes photocatalysts. **Applied Catalysis A: General**, v.481, p.127, 2014.

PATTERSON, A.L. The Scherrer Formula for X-Ray Particle Size Determination. **Physical Review**, v.56, n.10, p.978, 1939.

PAUL-DAUPHIN, S.; KARACA, F.; MORGAN, T.J.; MILLAN-AGORIO, M.; HEROD, A.A.; KANDIYOTI, R. Probing Size Exclusion Mechanisms of Complex Hydrocarbon Mixtures: The Effect of Altering Eluent Compositions. **Energy & Fuels**, v.21, n.6, p.3484, 2007.

PENN, S.G.; COSTA, D.A.; BALCH, A.L.; LEBRILLA, C.B. Analysis of C60 oxides and C120On (n = 1,2,3) using matrix assisted laser desorption-ionization Fourier transform mass spectrometry. **International Journal of Mass Spectrometry and Ion Processes**, v.169–170, p.371, 1997.

PRETO, M.DM., Caracterização dos Constituintes Poliméricos da Maytenus ilicifolia por Relaxação Nuclear de 1 H por RMN no Estado Sólido. **Polímeros**, v.21, n.5 p.416, 2011.

QUINTANA, M.; EDVINSSON, T.; HAGFELDT, A.; BOSCHLOO, G. Comparison of Dye-Sensitized ZnO and TiO2 Solar Cells: Studies of Charge Transport and Carrier Lifetime. **The Journal of Physical Chemistry C**, v.111, n.2, p.1035, 2007.

R. C. HIORNS, R.J.B., R. DUHLEV, K. H. HELLWICH, P. HODGE, A. D. JENKINS, R. G. JONES, J. KAHOVEC, G. MOAD, C. K. OBER, D. W. SMITH, R. F. T. STEPTO, J.-P. VAIRON, J. VOHLÍDAL. A brief guide to polymer nomenclature (IUPAC Technical Report). **Pure and Applied Chemistry**, v.84, n.10, p.2167, 2012.

RABI, I.I.; ZACHARIAS, J.R.; MILLMAN, S.; KUSCH, P. A New Method of Measuring Nuclear Magnetic Moment. **Physical Review**, v.53, n.4, p.318, 1938.

RAMANITRA, H.H, SANTOS SILVA, H., BREGADIOLLI B. A., KHOUKH. A., COMBE C.M.S., DOWLAND, S.A., BÉGUÉ, D., CARLOS F. O. GRAEFF, C.F.O., DAGRON-LARTIGAU, C, DISTLER, A., MORSE, G., HIORNS, R.C. Synthesis of Main-Chain Poly(fullerene)s from a Sterically Controlled Azomethine Ylide Cycloaddition Polymerization **Macromolecules**, 2016, 49 (5), pp 1681–1691 DOI: 10.1021/acs.macromol.5b02793

RAMANITRA, H.H., DOWLAND, S.A., BREGADIOLLI, B.A., SALVADOR, M. SANTOS SILVA,H., BÉGUÉ, D., GRAEFF, C.F.O., PEISERT, H., CHASSÉ, T. RAJOELSON, S., OSVET, A., BRABEC, C.J., EGELHAAF, H.J. MORSE, G., DISTLER, A., HIORNS, R.C. Increased Thermal Stabilization of Polymer Photovoltaic Cells with Oligomeric PCBM. **Journal of Materials Chemistry C,** Accepted Manuscript DOI: 10.1039/C6TC03290G

RASHAD, M. M., LIRA-CANTÚ, M., ABDEL-MOTTALEB, S.A.,. Enhancement of TiO2 nanoparticle properties and efficiency of dye-sensitized solar cells using modifiers. **Applied Nanoscience**, v.3, n.2, p.167, 2012.

REYNOLDS, D.C.; LEIES, G.; ANTES, L.L.; MARBURGER, R.E. Photovoltaic Effect in Cadmium Sulfide. **Physical Review**, v.96, n.2, p.533, 1954.

RODRÍGUEZ-GONZÁLEZ, V.; OBREGÓN-ALFARO, S.; LOZANO-SÁNCHEZ, L.M.; LEE, S.-W. Rapid microwave-assisted synthesis of one-dimensional silver–H2Ti3O7 nanotubes. **Journal of Molecular Catalysis A: Chemical**, v.353–354, p.163, 2012.

SAPONJIC, Z.V.; DIMITRIJEVIC, N.M.; TIEDE, D.M.; GOSHE, A.J.; ZUO, X.; CHEN, L.X.; BARNARD, A.S.; ZAPOL, P.; CURTISS, L.; RAJH, T. Shaping nanometer-scale architecture through surface chemistry. **Advanced Materials**, v.17, n.8, p.965, 2005.

SCHARBER, M.C.; MÜHLBACHER, D.; KOPPE, M.; DENK, P.; WALDAUF, C.; HEEGER, A.J.; BRABEC, C.J. Design Rules for Donors in Bulk-Heterojunction Solar Cells—Towards 10 % Energy-Conversion Efficiency. **Advanced Materials**, v.18, n.6, p.789, 2006.

SCHICK, G.; HIRSCH, A.; MAUSER, H.; CLARK, T. Opening and Closure of the Fullerene Cage in cis-Bisimino Adducts of C60: The Influence of the Addition Pattern and the Addend. **Chemistry – A European Journal**, v.2, n.8, p.935, 1996.

SHAHEEN, S.E., GINLEY, D.S., JABBOUR, G.E. Organic-based photovoltaics: toward low-cost power generation. **MRS Bulletin**, v. 30, p.10, 2005.

SHEN, P.-S.; TAI, Y.-C.; CHEN, P.; WU, Y.-C. Clean and time-effective synthesis of anatase TiO2 nanocrystalline by microwave-assisted solvothermal method for dye-sensitized solar cells. **Journal of Power Sources**, v.247, p.444, 2014.

SHI, S.; KHEMANI, K.C.; LI, Q.; WUDL, F. A polyester and polyurethane of diphenyl C61: retention of fulleroid properties in a polymer. **Journal of the American Chemical Society**, v.114, n.26, p.10656, 1992.

SHOCKLEY, W.; QUEISSER, H.J. Detailed Balance Limit of Efficiency of p-n Junction Solar Cells. **Journal of Applied Physics**, v.32, n.3, p.510, 1961.

SILVA, H.S.; TOURNEBIZE, A.; BEGUE, D.; PEISERT, H.; CHASSE, T.; GARDETTE, J.L.; THERIAS, S.; RIVATON, A.; HIORNS, R.C. A universal route to improving conjugated macromolecule photostability. **RSC Advances**, v.4, n.97, p.54919, 2014.
SING, K.S.W. Reporting physisorption data for gas/solid systems with special reference to the determination of surface area and porosity. **Pure and Applied Chemistry**, v.57, p.603, 1985.

SIVULA, K.; BALL, Z.T.; WATANABE, N.; FRÉCHET, J.M.J. Amphiphilic Diblock Copolymer Compatibilizers and Their Effect on the Morphology and Performance of Polythiophene:Fullerene Solar Cells. **Advanced Materials**, v.18, n.2, p.206, 2006.

STEPTO, R. F. T, HESS, R.G.G., JENKINS, A. D., JONES, R. G., KRATOCHVÍL, P., . Dispersity in polymer science (IUPAC Recommendations 2009). **Pure and Applied Chemistry**, v.81, n.2, p.351, 2009.

SU, C.; TSENG, C.M.; CHEN, L.F.; YOU, B.H.; HSU, B.C.; CHEN, S.S. Sol–hydrothermal preparation and photocatalysis of titanium dioxide. **Thin Solid Films**, v.498, n.1–2, p.259, 2006.

TANG, H.; LÉVY, F.; BERGER, H.; SCHMID, P.E. Urbach tail of anatase TiO_{2}. **Physical Review B**, v.52, n.11, p.7771, 1995.

TAUC, J.; GRIGOROVICI, R.; VANCU, A. Optical Properties and Electronic Structure of Amorphous Germanium. **physica status solidi (b)**, v.15, n.2, p.627, 1966.

THOMPSON, B.C.; FRÉCHET, J.M.J. Polymer–Fullerene Composite Solar Cells. **Angewandte Chemie International Edition**, v.47, n.1, p.58, 2008.

TSAI, C.-C.; TENG, H. Regulation of the Physical Characteristics of Titania Nanotube Aggregates Synthesized from Hydrothermal Treatment. **Chemistry of Materials**, v.16, n.22, p.4352, 2004.

URIEN, M.; WANTZ, G.; CLOUTET, E.; HIRSCH, L.; TARDY, P.; VIGNAU, L.; CRAMAIL, H.; PARNEIX, J.-P. Field-effect transistors based on poly(3-hexylthiophene): Effect of impurities. **Organic Electronics**, v.8, n.6, p.727, 2007.

UTSUNOMIYA, S.; EWING, R.C. Application of High-Angle Annular Dark Field Scanning Transmission Electron Microscopy, Scanning Transmission Electron Microscopy-Energy Dispersive X-ray Spectrometry, and Energy-Filtered Transmission Electron Microscopy to the Characterization of Nanoparticles in the Environment. **Environmental Science & Technology**, v.37, n.4, p.786, 2003.

VAN DER MADE, A.W.; VAN DER MADE, R.H. A convenient procedure for bromomethylation of aromatic compounds. Selective mono-, bis-, or trisbromomethylation. **The Journal of Organic Chemistry**, v.58, n.5, p.1262, 1993.

VITTADINI, A.; CASARIN, M.; SELLONI, A. Chemistry <i>of</i> and <i>on</i> TiO₂-anatase surfaces by DFT calculations: a partial review. **Theoretical Chemistry Accounts: Theory, Computation, and Modeling (Theoretica Chimica Acta)**, v.117, n.5, p.663, 2007.

W. KRÄTSCHME, L.D.L., K. FOSTIROPOULOS & DONALD R. HUFFMAN. Solid C60: a new form of carbon. **Nature**, v.347, p.354, 1990.

WANG, B.; WASIELEWSKI, M.R. Design and Synthesis of Metal Ion-Recognition-Induced Conjugated Polymers: An Approach to Metal Ion Sensory Materials. **Journal of the American Chemical Society**, v.119, n.1, p.12, 1997.

WANG, Y.-A.; YANG, J.; ZHANG, J.; LIU, H.; ZHANG, Z. Microwave-assisted Preparation of Titanate Nanotubes. **Chemistry Letters**, v.34, n.8, p.1168, 2005.

WENDLANT, W.W., Ed. **Thermal methods of analysis**. New York, p.p. 505, 2nd ed. ed, 1974.

WILSON, G.J.; WILL, G.D.; FROST, R.L.; MONTGOMERY, S.A. Efficient microwave hydrothermal preparation of nanocrystalline anatase TiO2 colloids. **Journal of Materials Chemistry**, v.12, n.6, p.1787, 2002.

WILSON, G.J.; MATIJASEVICH, A.S.; MITCHELL, D.R.G.; SCHULZ, J.C.; WILL, G.D. Modification of TiO2 for Enhanced Surface Properties: Finite Ostwald Ripening by a Microwave Hydrothermal Process. **Langmuir**, v.22, n.5, p.2016, 2006.

WRIGHT, M.; UDDIN, A. Organic—inorganic hybrid solar cells: A comparative review. **Solar Energy Materials and Solar Cells**, v.107, p.87, 2012.

WU, J.; LAN, Z.; LIN, J.; HUANG, M.; HUANG, Y.; FAN, L.; LUO, G. Electrolytes in Dye-Sensitized Solar Cells. **Chemical Reviews**, v.115, n.5, p.2136, 2015.

WU, X.; JIANG, Q.-Z.; MA, Z.-F.; FU, M.; SHANGGUAN, W.-F. Synthesis of titania nanotubes by microwave irradiation. **Solid State Communications**, v.136, n.9–10, p.513, 2005.

WU, X.; JIANG, Q.-Z.; MA, Z.-F.; SHANGGUAN, W.-F. Tile overlapping model for synthesizing TiO2 nanotubes by microwave irradiation. **Solid State Communications**, v.143, n.6–7, p.343, 2007.

XIN, X.; SCHEINER, M.; YE, M.; LIN, Z. Surface-Treated TiO2 Nanoparticles for Dye-Sensitized Solar Cells with Remarkably Enhanced Performance. **Langmuir**, v.27, n.23, p.14594, 2011.

XU, T.; QIAO, Q. Conjugated polymer-inorganic semiconductor hybrid solar cells. **Energy & Environmental Science**, v.4, n.8, p.2700, 2011.

XU, T.; YAN, M.; HOEFELMEYER, J.D.; QIAO, Q. Exciton migration and charge transfer in chemically linked P3HT-TiO2 nanorod composite. **RSC Advances**, v.2, n.3, p.854, 2012.

YANG, C.; CHO, S.; HEEGER, A.J.; WUDL, F. Heteroanalogues of PCBM: N-Bridged Imino-PCBMs for Organic Field-Effect Transistors. **Angewandte Chemie International Edition**, v.48, n.9, p.1592, 2009a.

YANG, C.; LEE, J.K.; HEEGER, A.J.; WUDL, F. Well-defined donor-acceptor rod-coil diblock copolymers based on P3HT containing C60: the morphology and role as a surfactant in bulk-heterojunction solar cells. **Journal of Materials Chemistry**, v.19, n.30, p.5416, 2009b.

YANG, H.-T.; XING, M.-L.; ZHU, Y.-F.; SUN, X.-Q.; CHENG, J.; MIAO, C.-B.; LI, F.-B. BF3·Et2O-Catalyzed Formal [3 + 2] Reaction of Aziridinofullerenes with Carbonyl Compounds. **The Journal of Organic Chemistry**, v.79, n.3, p.1487, 2014.

YANG, J.; MEI, S.; FERREIRA, J.M.F. Hydrothermal synthesis of TiO2 nanopowders from tetraalkylammonium hydroxide peptized sols. **Materials Science and Engineering: C**, v.15, n.1–2, p.183, 2001.

YANG, Y.; TURNBULL, G.A.; SAMUEL, I.D.W. Hybrid optoelectronics: A polymer laser pumped by a nitride light-emitting diode. **Applied Physics Letters**, v.92, n.16, p.163306, 2008.

YE, M.; WEN, X.; WANG, M.; IOCOZZIA, J.; ZHANG, N.; LIN, C.; LIN, Z. Recent advances in dye-sensitized solar cells: from photoanodes, sensitizers and electrolytes to counter electrodes. **Materials Today**, v.18, n.3, p.155, 2015.

YIN, H.; WADA, Y.; KITAMURA, T.; KAMBE, S.; MURASAWA, S.; MORI, H.; SAKATA, T.; YANAGIDA, S. Hydrothermal synthesis of nanosized anatase and rutile TiO2 using amorphous phase TiO2. **Journal of Materials Chemistry**, v.11, n.6, p.1694, 2001.

YU, J.G., HUMMELE,N J. C., WUDL, F., HEEGER, A. J. Polymer Photovoltaic Cells: Enhanced Efficiencies via a Network of Internal Donor-Acceptor Heterojunctions. **Science**, v.270, p.1789, 1995.

ZACHARY A. SMITH, K.D.T., Ed. **Renewable and Alternative Energy Resources**. Santa Barbara: ABC-CLIO, Inc., p.138, 164ed, 2008.

ZHANG, H.; BANFIELD, J.F. Understanding Polymorphic Phase Transformation Behavior during Growth of Nanocrystalline Aggregates: Insights from TiO2. **The Journal of Physical Chemistry B**, v.104, n.15, p.3481, 2000.

ZHANG, Y.; WANG, C.; ROTHBERG, L.; NG, M.-K. Surface-initiated growth of conjugated polymers for functionalization of electronically active nanoporous networks: synthesis, structure and optical properties. **Journal of Materials Chemistry**, v.16, n.37, p.3721, 2006.

ZHAO, B.; LIN, L.; HE, D. Phase and morphological transitions of titania/titanate nanostructures from an acid to an alkali hydrothermal environment. **Journal of Materials Chemistry A**, v.1, n.5, p.1659, 2013.

ZHU, W.; MA, D. Synthesis of aryl azides and vinyl azides via proline-promoted CuI-catalyzed coupling reactions. **Chemical Communications**, n.7, p.888, 2004a.

ZHU, W.; MA, D. Synthesis of aryl azides and vinyl azides via proline-promoted CuI-catalyzed coupling reactions. **Chemical Communications**, v.0, n.7, p.888, 2004b.

ZHU, Y.-J.; CHEN, F. Microwave-Assisted Preparation of Inorganic Nanostructures in Liquid Phase. **Chemical Reviews**, v.114, n.12, p.6462, 2014.